TESIS DE LA UNIVERSIDAD DE ZARAGOZA
2026
30

Verónica Lockett Ruiz

Modeling the gradient index and curvature of the crystalline lens: impact on optical performance and changes with age and accommodation

Director/es
Navarro Belsué, Rafael

ISSN 2254-7606

Prensas de la Universidad
Universidad Zaragoza

Universidad de Zaragoza
Servicio de Publicaciones

ISSN 2254-7606

Universidad Zaragoza
1542

Tesis Doctoral

MODELING THE GRADIENT INDEX AND CURVATURE OF THE CRYSTALLINE LENS: IMPACT ON OPTICAL PERFORMANCE AND CHANGES WITH AGE AND ACCOMMODATION

Autor

Verónica Lockett Ruiz

Director/es

Navarro Belsué, Rafael

UNIVERSIDAD DE ZARAGOZA
Escuela de Doctorado

2025

Universidad Zaragoza
1542

Tesis Doctoral

Modeling the gradient index and curvature of the crystalline lens: impact on optical performance and changes with age and accommodation

Autora

Verónica Lockett Ruiz

Director

Rafael Navarro Belsué

Facultad de Ciencias / Física

2025

MODELING THE GRADIENT INDEX AND CURVATURE OF THE CRYSTALLINE LENS:

IMPACT ON OPTICAL PERFORMANCE AND CHANGES WITH AGE AND ACCOMMODATION

VERONICA LOCKETT RUIZ

SUPERVISOR:
Rafael Navarro Belsué

Departamento de Física Aplicada
Universidad de Zaragoza

Zaragoza, October 2025

MARIE CURIE ACTIONS

INMA
INSTITUTO DE NANOCIENCIA Y MATERIALES DE ARAGÓN

CSIC
CONSEJO SUPERIOR DE INVESTIGACIONES CIENTÍFICAS

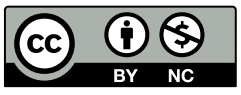

We can,
Each of us,
Do the impossible
As long as we can convince
ourselves
That it has been done before.

Parable of the Talents
Octavia Butler, 1998

For those who came before me.
For the ones who were denied but fought anyway
and the ones who walked so that we could run.

ACKNOWLEDGMENTS

To my partner in crime, Raúl, thank you for standing by my side through thick and thin. You have been my number-one supporter ever since we met, and your unwavering encouragement whenever new endeavors spark in my mind is truly unmatched. To the moon and back.

To my parents, Margarita, Miguel, and Jason, you nourished my young, curious mind and provided my brain and heart with the space to grow. You instilled in me the importance of education and taught me to always strive for my best. To my siblings, Azahara and David, I will forever be grateful that our parents gave me you. I can't imagine what it would have been like to grow up alone; you brought spice to my life.

To my thesis supervisor, Rafa Navarro, I appreciate your incredible generosity with your time and expertise. Thank you for always being available whenever I needed clarification, assistance, or corrections. This thesis would have been impossible without your continued help and support.

To my academic tutor, Ana Sánchez-Cano, thank you for graciously sharing your wisdom in visual optics, optometry, and any other area where I've needed assistance. Despite your busy schedule, you always offered a listening ear and invaluable advice. You have helped me navigate this experience in more ways than you know.

To my coauthors, Norberto López-Gil and José Luis López, I extend my sincere gratitude for their valuable scientific discussions, advice, and contributions.

To the team at the Visual Optics Lab Antwerp (VOLANTIS), you made me feel at home away from home. Jos Rozema, a huge thank you for trusting me, encouraging me to fly solo, and seeking collaboration opportunities that I could benefit from. Sharon, Hosna, and Arezoo, I always felt like part of the team when I was there. For that, I thank you.

To Barbara Pierscionek at Anglia Ruskin University, thank you for welcoming me into your team and sharing your knowledge. Fabian, I am forever grateful that you came to Chelmsford to greet me and show me around that first weekend. We had great food and great conversations, too. Lin, thanks for your help in getting me settled at the university.

I would also like to acknowledge my OBERON co-ESRs, who have journeyed alongside me these last three years. It's been fun times with you during meetings and secondments. Congratulations to everyone on earning your Ph.D.s; we made it! I really hope we get to meet again sometime.

María, Iñaki, Benedetta, Elena, and Matteo, you guys rock. Even though we haven't spent much time together, I appreciated the moments we did share, from our love of food to the lively discussions, vents, and laughter.

Alba and Justi, I have genuinely enjoyed our time together. Thank you for opening your office to me and for your patience with my comings and goings; I will miss our conversations. And Víctor, my next-door office neighbor,

I can't thank you enough for that phone call about the PhD grant opportunity—without it, I literally wouldn't be here now.

Last, I would like to acknowledge the financial support I received from the European Union's Horizon 2020 research and innovation program under the Marie Skłodowska-Curie grant agreement No 956720.

ABSTRACT

The crystalline lens is the most dynamic optical component of the human visual system, fulfilling the vital role of keeping light focused on the retina. This adaptive structure undergoes both short-term (accommodation) and long-term (aging, presbyopia, and cataracts) changes that affect the eye's optical properties. Understanding these changes and their impact on vision requires lens models that adapt to variations across the population, age, and accommodation while accurately reflecting the lens's optical performance.

We propose the GRINCU model [1], which combines a gradient refractive index (GRIN) with a gradient curvature of the iso-indicial surfaces (GRCU). The GRINCU model introduces a novel approach by incorporating a curvature radius gradient parameter, allowing for non-concentric surface configurations of the iso-indicial surfaces (IIS). The refractive index distribution follows an experimental power law, with distinct anterior and posterior distributions, while the interface is defined by the curved surface formed by the locus of the anterior and posterior hemispheres of the IIS.

A custom ray transfer matrix was derived for general onion-type GRIN lenses, providing a compact and accurate expression of the lens's refractive power. Both finite and paraxial ray tracing were conducted using two software platforms: Zemax OpticStudio and RTLib, a custom ray tracing library for Matlab, on two GRINCU configurations—singlet and doublet. Cross-validation confirmed consistency across platforms and configurations. An accommodative GRINCU lens model was developed based on the observed changes in lens curvature gradient with accommodation. This model was used to analyze Gullstrand's intracapsular accommodation mechanism. To evaluate the optical performance of the GRINCU lens within the eye, we analyzed 200 synthetic eyes (SyntEyes [2]) and compared the results with homogeneous and GRIN lens models. Lastly, age-related changes were examined using age-dependent geometrical lens data to quantify the evolution of curvature gradient with age. From this aging model, an accurate numerical explanation of the lens paradox was obtained in terms of the age-related changes in its inner curvature gradient (CRCU).

Results from ray tracing indicate that the curvature gradient enhances optical power while reducing spherical aberration and astigmatism compared to homogeneous models. It was also noted that steeper curvature gradients lead to improved optical quality. An analysis of the intracapsular accommodation mechanism (IAM) revealed a positive relationship between the equivalent refractive index and accommodation across all age groups, suggesting a gradual increase in IAM contributions with age.

The GRINCU model accurately reflects the optical performance of the human crystalline lens and provides a quantitative explanation for the lens paradox. These findings highlight the importance of considering both the refractive index gradient and curvature gradient in understanding lens aging and accommodation.

RESUMEN

El cristalino es el componente óptico más dinámico del sistema visual humano, adaptándose continuamente para mantener el enfoque de la luz en la retina. A lo largo de la vida, experimenta cambios a corto plazo (acomodación) y a largo plazo (envejecimiento, presbicia y cataratas) que modifican sus propiedades ópticas. Comprender estos cambios y su impacto en la visión requiere modelos que reflejen con precisión el rendimiento óptico del cristalino y se adapten a la variabilidad poblacional, la edad y la acomodación.

Esta tesis doctoral presenta el modelo GRINCU [3], que combina un gradiente de índice de refracción (GRIN) y un gradiente de curvatura de las superficies iso-índice (GRCU). El modelo GRINCU es novedoso al incorporar un gradiente del radio de curvatura, permitiendo configuraciones no concéntricas de las superficies iso-índice (IIS). La distribución del índice de refracción sigue una ley potencial experimental, con perfiles diferenciados en las regiones anterior y posterior de la lente. La interfaz es aquí una superficie curva, lugar geométrico de los hemisferios anterior y posterior de las IIS.

Para el análisis óptico, se ha derivado una matriz de transferencia de rayos específica para lentes GRIN tipo cebolla, obteniendo una expresión compacta y precisa de la potencia refractiva. Posteriormente, se ha realizado el trazado de rayos finito y paraxial utilizando Zemax OpticStudio y RTLib, una biblioteca personalizada en Matlab, para configuraciones de singlete y doblete. La validación cruzada confirmó la coherencia entre ambas plataformas y configuraciones. Se ha desarrolado además un modelo de lente GRINCU acomodativo, basado en los cambios observados en el gradiente de curvatura con la acomodación, para analizar el mecanismo de acomodación intracapsular de Gullstrand. Para evaluar el rendimiento óptico de la lente GRINCU dentro del ojo, se han analizado 200 ojos sintéticos (SyntEyes [2]) y se han comparado los resultados con modelos de lente homogénea y GRIN. Por último, se han analizado los cambios en el cristalino con la edad utilizando datos geométricos experimentales del cristalino para cuantificar la evolución del gradiente de curvatura con el envejecimiento. A partir de este modelo, se obtuvo una explicación cuantitativa de la paradoja del cristalino, en función de los cambios en el gradiente de curvatura interna con la edad.

Los resultados del trazado de rayos indican que el gradiente de curvatura aumenta la potencia óptica, al tiempo que reduce la aberración esférica y el astigmatismo en comparación con modelos homogéneos. Se observó también que gradientes de curvatura más pronunciados mejoran la calidad óptica. El análisis del mecanismo de acomodación intracapsular (IAM) revela una relación positiva entre el índice de refracción equivalente y la acomodación, lo que sugiere un incremento progresivo de la contribución del IAM a la potencia acomodativa con la edad.

El modelo GRINCU reproduce con precisión el rendimiento óptico del cristalino humano y proporciona una explicación cuantitativa de la paradoja del

cristalino. Estos hallazgos recalcan la importancia de considerar tanto el gradiente de índice de refracción como el gradiente de curvatura para comprender el envejecimiento del cristalino y su función acomodativa.

LIST OF PUBLICATIONS

Some of the concepts, analyses, and figures presented in this dissertation have been published in the following peer-reviewed articles:

1. Navarro, R., Lockett-Ruiz, V. & López, J. L. Analytical ray transfer matrix for the crystalline lens. *Biomedical Optics Express* **13,** 5836–5848 (2022)

2. Lockett-Ruiz, V., Navarro, R. & López-Gil, N. Intracapsular accommodation mechanism in terms of lens curvature gradient. *Ophthalmic and Physiological Optics* **44,** 334–346 (2024)

3. Lockett-Ruiz, V., Navarro, R. & Rozema, J. Effect of gradient-index lenses on the optical performance of SyntEyes. en. *J. Optom.* **18,** 100568 (July 2025)

4. Lockett-Ruiz, V. & Navarro, R. Modeling the aging crystalline lens: a quantitative explanation of the lens paradox. en. *J. Opt. Soc. Am. A Opt. Image Sci. Vis.* **42,** 1048 (Aug. 2025)

At the time of the thesis defense, the following article had also been published, but its contents are not included in this dissertation:

5. Lockett-Ruiz, V., Evans, T., Navarro, R., Mashige, K. P. & Rozema, J. J. Zulu ocular biometry differs fundamentally from that of Europeans–A modelling analysis. *Ophthalmic and Physiological Optics* (2025)

ACRONYMS

H&E	hematoxylin and eosin
GRIN	gradient index
GRCU	gradient curvature
MRI	magnetic resonance imaging
OCT	optical coherence tomography
IAM	intracapsular accommodation mechanism
GRINCU	gradient index and gradient curvature
UV	ultraviolet
IOL	intraocular lens
SA	spherical aberration
LCA	longitudinal chromatic aberration
TCA	transverse chromatic aberration
IIS	isoindicial surface
GRCU	gradient curvature
RMS	root mean square

CONTENTS

LIST OF FIGURES

LIST OF TABLES

INTRODUCTION

1 INTRODUCTION

1.1 ANATOMY AND PHYSIOLOGY OF THE VISUAL SYSTEM

The process of sight and visual perception is a complex interplay of specialized structures, each with its unique function. Within the eye, there are elements that refract, focus, and convert light rays into neural signals, which are then transmitted and interpreted by the brain. Externally, the eye is shielded by the orbital bone and connective tissue of the orbit. The eyelids protect the eye's front surface and house the glands that produce the lubricating tear film. The eye muscles, attached to the outer layer, control and direct the eye's movements, with the muscles of both eyes working in harmony for binocular vision. This intricate system is fundamental to how we perceive our environment and navigate the world.

1.1.1 Overview of the Eye

The eye consists of three coats or tunics: an outer fibrous layer that forms the sclera and cornea, a middle vascular layer that contains the iris, ciliary body, and choroid, and an inner neural layer that constitutes the retina. From outside to inside, the globe is composed of the following elements:

THE CORNEA, located at the front of the globe, is shaped like a positive meniscus lens and is one of the two lenses in the eye's optic system. It is approximately a prolate ellipsoid and has a radius of curvature of about 7.8 mm; it is separated from the sclera by about 5 mm. The cornea has roughly twice the refractive power of the crystalline lens (~44 D). The anterior corneal surface is covered by the tear film, which is crucial for maintaining the optimal environment for the corneal epithelial cells, smoothing and lubricating the corneal surface. The posterior corneal surface borders the anterior chamber. At its periphery, the cornea connects with the conjunctiva and the sclera.

THE SCLERA, also known as the white of the eye, is the eye's outermost layer and makes up most of the fibrous coat, making up the posterior five-sixths of the connective tissue covering the globe. It is a dense, opaque, and protective, approximately spherical tissue with a curvature radius of around 12 mm. It holds the eye's shape by countering internal and external forces and provides attachment for the extraocular muscle insertions.

- The sclera is continuous with the corneal stroma at the *limbus*, a band between 1.5 and 2 mm thick that encircles the cornea's periphery. The limbus is the transitional zone between the cornea and the adjacent conjunctiva and sclera.

- The *conjunctiva* is a translucent, mucous membrane that, starting from the limbus, runs over the anterior sclera, folds at the superior and inferior fornices, and then covers the inside of the eyelids. It ensures that the eyelids glide smoothly over the eye globe.

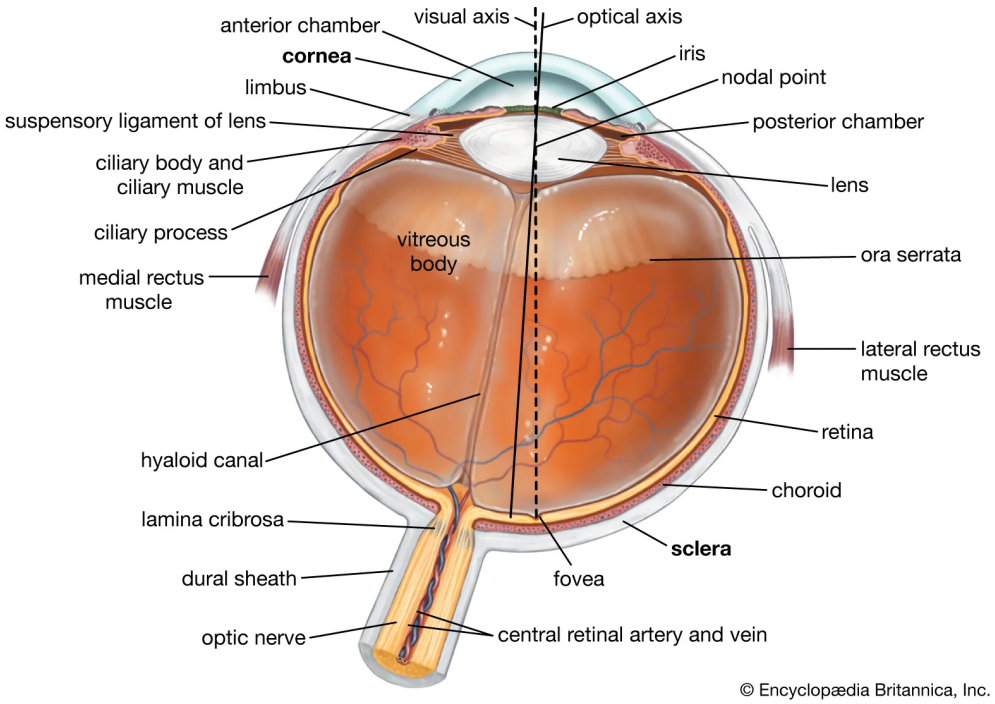

Figure 1.1: Horizontal section of the right eye, seen from above.

THE UVEA or uveal tract is the eye's middle layer and consists of a vascular coat comprised of four structures with different roles.

- The *iris* is a thin, circular structure located anterior to the lens. It acts like a diaphragm by regulating the amount of light that enters the eye, and it controls the shape and size of the pupil.

- The *pupil* regulates how much light enters the retina; its diameter can vary from 1 to 9 mm depending on lighting conditions. The iris is roughly 12 mm in diameter and divided into the pupillary zone, which encircles the pupil, and the ciliary zone, which extends to the iris root. The concentration of melanin granules in the iris's front layer determines our eyes' color. The pupil is usually decentered in real eyes, often being displaced nasally around 0.5 mm relative to the optical axis. Both natural and drug-induced pupil dilations cause a displacement of the pupil center away from the optical axis.

- Connected with the iris is the *ciliary body*, a ring-shaped structure that supplies aqueous humor to the anterior chamber, acting as a blood-aqueous barrier and regulating the protein content of the aqueous humor. The ciliary body houses the ciliary muscles, which regulate lens accommodation, a topic that will be explored in more detail below.

- The *choroid* is the posterior region of the uvea, extending from the ora serrata to the retina. It is a highly vascularized network that surrounds the retina, supplying nutrients to its outer layers. Besides providing oxygen and nutrients to the outer retina, the choroid participates in retinal thermoregulation and intraocular pressure drainage. The innermost layer of the choroid, Bruch membrane, is an acellular multi-laminated sheet that runs from the optic nerve to the ora serrata. It is tightly adhered to the outer layer of the retina.

THE RETINA is the innermost layer of the eye, located between the choroid and the vitreous body. It converts light into neural signals that travel to the brain along the optic nerve. The retinal pigment epithelium is the outermost retinal layer. It is a single layer of cells that extends from the ora serrata to the optic disc and is tightly attached to the choroid. The retinal pigment epithelium protects and maintains the health of the neural retina and enables photoreceptor cells to detect light. The neural retina comprises three layers of specialized cells that transform light into neural signals and transmit them to the brain. The peripheral retina detects gross form and motion, with rods being the dominating photoreceptor, whereas the central area is specialized for visual acuity and is rich in cones.

- In the center of the posterior portion of the retina is the *macula lutea*, responsible for high-resolution vision in good light. It is approximately 5.5 mm in diameter, and it contains the fovea.

- Centered in the macula is the *fovea*, a slight depression in the retina that, in emmetropic eyes, corresponds to the eye's focal point. The fovea is rod-free, having the highest density of cone photoreceptors, and is responsible for high-acuity vision.

The eye's interior contains three chambers, each filled with a fluid substance, and the crystalline lens.

- The *anterior chamber* is enclosed by the cornea anteriorly and the iris posteriorly. The *posterior chamber* is behind the iris and bound by the anterior surface of the lens. The anterior and posterior chambers are continuous through the opening of the iris, and they are filled with aqueous humor, which is responsible for providing oxygen and glucose to the avascular cornea and lens. The aqueous humor is produced in the ciliary body.

- Extending from the back of the lens to the retina is the *vitreous body*, taking up most of the volume of the eye. The vitreous body is filled with vitreous humor, a highly transparent gel-like substance made of salts, soluble proteins, and hyaluronic acid sustained by a collagen meshwork. The vitreous body provides physical support for the retina, stores metabolites for the retina and lens, and allows the transport of these substances within the eye. It also acts as a shock absorber and transmits and refracts light, aiding in focusing the rays in the retina.

- The *crystalline lens* is positioned between the anterior and the posterior chamber, behind the iris. It is a transparent elliptical structure composed of specialized cells called lens fibers, which give the lens a higher protein concentration (60%) than any other bodily tissue. The lens provides refractive power to the eye and focuses images on the retina. The crystalline lens is further discussed in Section 1.1.3.

The following sections overview the two main lenses of the eye's optical system.

1.1.2 The Cornea

The cornea is the principal refractive element of the eye; its transparency and avascularity provide optimal light transmission. From the side, the cornea appears elliptical rather than spherical, with a steeper curvature near the center and flatter in the periphery. Its anterior surface has an average radius of curvature of 7.8 mm, while the posterior is around 6.5 mm. Frontally, the cornea appears slightly elongated as it has a greater horizontal than vertical diameter (12 mm horizontally and 11 mm vertically). The cornea is composed of five layers, from front to (see fig. 1.2):

- The *epithelium* is the cornea's outermost layer, approximately 50 µm thick and continuous with the conjunctiva at the limbus. It acts as a barrier to microbes, chemicals, and water and provides a smooth surface with the tear film to contribute to the eye's refractive power.
- The *Bowman layer* is a transition layer between the epithelium and the stroma. It is between 8 and 19 µm thick and consists of an acellular, dense, fibrous sheet of intertwined collagen fibers. The Bowman layer is highly resistant to physical damage and infection and is crucial in maintaining the shape of the cornea.
- The *stroma* makes up most of the corneal thickness. It comprises a highly organized arrangement of collagen fibrils that lie parallel to the corneal surface, making it highly transparent. The stroma contains scattered cells called keratocytes whose cellular products support normal corneal development and homeostasis. It also includes substances that maintain corneal shape and tensile strength and confer mechanical strength and transparency to the cornea.
- The *Descemet membrane* acts as a resting layer for the endothelial cells. It is produced continually throughout life and can be regenerated if damaged. This membrane exhibits elastic properties that make it very resistant to trauma.
- The *endothelium* separates the cornea from the anterior chamber. It is partially permeable and allows the entrance of nutrients from the aqueous humor into the cornea. The endothelium maintains corneal clarity and adequate hydration by pumping water from the corneal stroma.

Age-related alterations to the cells that maintain tissue integrity cause the breakdown of the barrier function of the corneal epithelium, rendering the

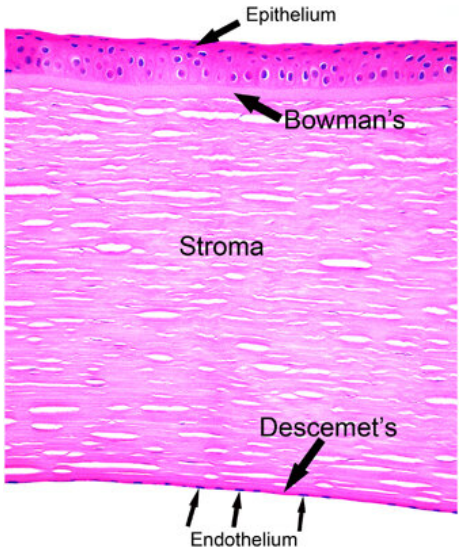

Figure 1.2: H&E of a normal cornea [8].

cornea more vulnerable to insults. Although the corneal thickness remains constant with age, the Bowman layer undergoes a thickness loss of around 32% between ages 20 and 80. This thinning can affect wound healing and disrupt the transparency of the cornea. On the contrary, the Descemet membrane thickens with age and forms small transparent growths in the periphery of its posterior surface that initially do not affect vision; over time, however, they cause a loss of transparency in the cornea, resulting in glare and scattering.

1.1.3 The Crystalline Lens

The crystalline lens is an avascular and anerval transparent, biconvex structure with an anterior radius of curvature between 8 and 14 mm and a posterior radius of curvature between 5 and 8 mm. The adult unaccommodated lens's thickness is 4 mm on average, ranging from 3.6 to 4.5 mm, and it has a growth rate of approximately 0.02 mm per year. The lens is around 9 mm wide in diameter, measured at the equator, where the anterior and posterior surfaces meet. The ciliary muscles' processes encircle the equator of the lens. And the lens itself is kept in place by the suspensory ligaments. The refractive power of the unaccommodated lens is approximately 23 D, with a maximum accommodative amplitude of 14 D reached between ages 8 and 12 years. The protein concentration within the lens fibers changes the optical density throughout the lens, resulting in a gradient refractive index (GRIN). The refractive index increases from the periphery to the center of the lens, with refractive indices of approximately 1.38 at the cortex and 1.41 at the lens core.

- The *lens capsule* is a transparent coat that encloses the lens. It is semipermeable, keeping large molecules outside and allowing the passage of nutrients and antioxidants to the lens. The anterior capsule thickens with age, growing from around 11 to 15 µm at the pole. The annular region surrounding the pole is the thickest, thickening with age from 13.5 to 16 µm. At the posterior pole, the lens capsule is the thinnest, with approxi-

mately 3.5 µm, and it does not change appreciably with age. Equatorially, the capsule is around 7 µm and thickens slightly with age. It is mainly made of collagen, and it is elastic due to the arrangement of its fibers. The lens capsule shapes the lens and is pulled at the equator by the zonular fibers of the ciliary muscles.

- The *lens epithelium* lies beneath the anterior lens capsule. It is found only at the anterior surface of the lens since the posterior epithelium is used during embryological development to form the posterior lens fibers. Close to the equator, the epithelial cells elongate toward the poles, where they merge at the lens sutures and become lens fibers. This process happens all around the equator, with fibers reaching toward the pole from the periphery of the lens. The lens epithelium regulates nutrients and ions and enhances water movement in and out of the lens.

- The *lens fibers*, which comprise the bulk of the lens, are formed by the multiplication and differentiation of the lens epithelial cells close to the equator. They are produced throughout our lives, with the new fibers stacking over the preceding generations of cells that lie closer to the lens nucleus. The lens structure is similar to that of an onion, where each layer is made of adjacent fibers within the layer. The lens fibers contain high concentrations of proteins known as crystallins, which account for almost half of the fiber weight and contribute to the gradient refractive index and the lens's transparency.

- The *epithelium-fiber interface* is the border between the anterior epithelium and the elongating fiber, and its primary function is nutrient and ion exchange.

The lens comprises the cortex and nucleus (fig. 1.3). The embryonic nucleus is the innermost part of the lens, forming between one and three months of gestation. The fetal nucleus includes the embryonic nucleus and the surrounding fibers formed before birth. The adult nucleus encompasses the embryonic and fetal nucleus and the fibers formed between birth and sexual maturation. The remaining layers make up the lens cortex. The refractive index of the lens is highest at the embryonic nucleus and lowest at the cortex. Due to the continual growth of lens fibers, the crystalline lens thickens at a rate of approximately 0.02 mm per year as age advances. It also undergoes an opacification process due to the deterioration of the fiber material. The natural changes that occur with aging contribute to the development of presbyopia and cataracts, which will be discussed further in Section 1.2.3.

1.2 OPTICS OF THE HUMAN EYE

The formation of images by the eye follows the same physical and optical principles as manufactured optical devices such as telescopes and cameras. Rays of light enter the eye through the cornea and are focused on the retina by the cornea and the lens. When light reaches the eye, the diameter of the incoming beam is regulated by the iris diaphragm (pupil), which acts as the

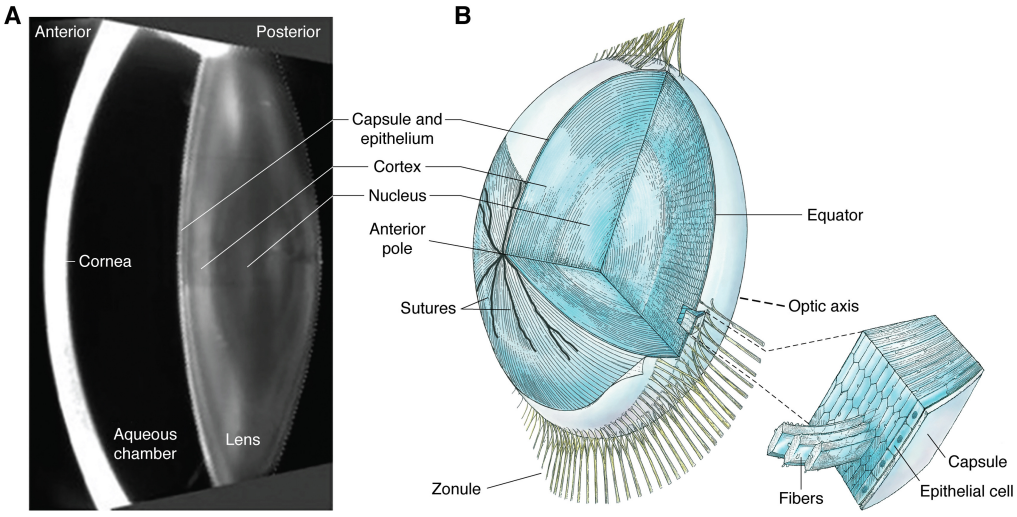

Figure 1.3: *Left:* OCT image of the anterior segment.
Right: Internal structure of the crystalline lens [9].

aperture stop of the eye. The pupil's diameter affects the depth of field, retinal light level, and retinal image quality.

The optical axis is defined as the line traversing the center of curvature of the refracting surfaces of a centered optical system. Because the eye is not a centered system, it does not have a true optical axis, but we can define one as the 'best fit' through the centers of curvature of the 'best fit' spheres of the corneal and lenticular surfaces. Line of sight, however, is The paraxial approximation states that light rays approaching the eye must have small angles of incidence relative to the optical axis. This means that in ray-tracing equations, replacing tangents and sines of the angles with the angles themselves (in radians) results in negligible errors. Paraxial ray tracing is optimal for calculating the refractive power and the cardinal points of the eye's optical system. The refractive power of the eye can be calculated with the following equation:

$$P_{eye} = P_{cornea} + P_{lens} - \frac{\overline{H'_c H_l}}{n_{aq}} \cdot P_{cornea} P_{lens} \tag{1.1}$$

P_{cornea} is the corneal power, P_{lens} is the lenticular power, n_{aq} is the refractive index of the aqueous humor, and $\overline{H'_c H_l}$ is the distance from the image principal plane of the cornea (H'_c) to the object principal plane of the lens (H_l).

1.2.1 Internal Structure of the Lens (GRIN)

The refractive index within the lens varies, being highest at the center and lowest at the edges. The refractive index remains nearly constant in the nucleus, with the most significant variations found in the cortex (periphery). This variation in the refractive index results in a gradual and continuous bending of light rays, potentially reducing spherical aberration [10] and enhancing the refractive power of the lens. The gradient refractive index follows an empirical power function:

$$n(r) = n_0 + (n_s - n_0) r^{2p} \tag{1.2}$$

Where $n(r)$ is the relative distance in any direction, from the point of highest refractive index n_0 on the optical axis to ns on the lens surface, and the coefficient p determines the steepness of the gradient. When the gradient (GRIN) index lens is replaced with a lens of uniform thickness and curvature but with a homogeneous refractive index, this index must be increased beyond the maximum index of the gradient lens to achieve the same lens power. The equivalent refractive index was typically considered to be 1.42, slightly higher than the gradient lens's maximum value of approximately 1.41 (at the center).

1.2.1.1 Measuring the Lens' Refractive Index Distribution

Over the years, various destructive and non-destructive methods for measuring the refractive index distribution within the lens have been developed. This discussion will focus solely on techniques used for human lenses. Destructive methods often involved freezing and slicing the crystalline lens before further analysis. For instance, some researchers employed Schlieren interferometry to reveal the gradient index of lens sections [11], while others used Pulfrich refractometry with a prism to observe iso-indicial surfaces [12]. Also requiring lens freezing and slicing, densitometry determined the refractive index by assessing the quantitative chemical composition and protein concentration in different lens regions [13]. A less destructive approach used an optic fiber reflectometer to probe the lens [14]. However, all the above methods require altering the intact lens, which inherently affects the GRIN structure being examined. Consequently, several non-destructive techniques have been proposed as alternatives. In vitro methods include laser ray tracing [15–17], magnetic resonance imaging (MRI) [18, 19], X-ray Talbot interferometry [20, 21], and optical coherence tomography (OCT) [22–25]. Among all these techniques, only MRI currently allows for in vivo analysis [26–30]. Despite the variety of measuring methods and the rapid advancements in non-destructive methods due to technological innovation, there is still no consensus on the exact refractive index values of the lens surface and core or the precise shape of the GRIN profile. Consequently, there is no agreement on which model best fits the natural lens either. All studies concur that the refractive index distribution changes with aging, reporting a smooth increase of the refractive index value from the surface to the nucleus in the young eye and a flattening of this profile, forming a central plateau with aging.

1.2.2 Accommodation

Accommodation occurs when the ciliary muscles contract, increasing the lens's refractive power to form a sharp image of close objects. It allows non-presbyopic individuals to focus near objects on the fovea but is also related to how distant objects are focused on the retina.

René Descartes was the first to mention the role of the crystalline lens in accommodation in 1677. It was Thomas Young, though, who in 1801 quantified the lens's alterations during accommodation by examining changes in Purkinje images. Later, in 1855, Helmholtz proposed the most widely accepted theory of the accommodation mechanism, also grounded in the variations observed

in Purkinje images. It is commonly agreed that accommodation arises from alterations in the curvature of the crystalline lens surface; however, the lens itself cannot alter its size. This curvature change is facilitated by the ciliary muscles encircling the lens's equator and the zonules of Zinn, which connect the lens to the ciliary muscles and convey the movement of the ciliary muscles to the lens capsule. All these changes increase the lens's and the eye's equivalent refractive power.

When it contracts, the ciliary muscle moves inward and forward, causing several eye components to shift forward: the pupillary edge and the anterior surface of the lens move approximately 0.3 mm into the anterior chamber, and the choroid shifts around 0.5 mm (see fig. 1.4). Due to the specific innervation pattern of the ciliary muscles, this movement is associated with pupil constriction (miosis). When the eye disaccommodates, the reverse process takes place.

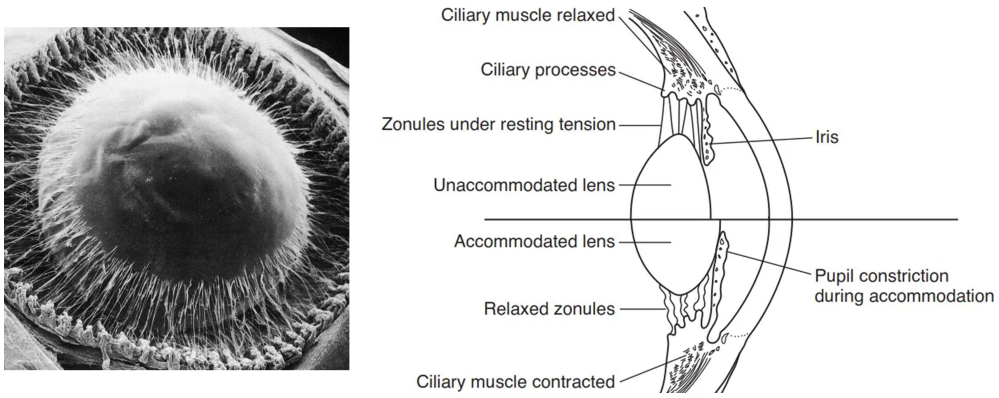

Figure 1.4: *Left:* Scanning electron micrograph of the anterior zonular insertions [31]. *Right:* Relaxed vs. accommodated lens [32].

The physical constraints on the range of lens shapes limit changes in lens power and the range of clear vision. The far point is the spatial point conjugate to the retina when the eye is not accommodating. Conversely, the near point is the spatial point conjugate to the retina when the eye is fully accommodated. Simply put, the far and near points represent the furthest and closest distances at which objects can be seen clearly (see fig. 1.5). The difference between these vergences is the amplitude of accommodation or accommodative range. At birth, the amplitude of accommodation is at its peak, around +20D, because the crystalline lens is most elastic. This amplitude decreases with age due to changes in the lens and ciliary muscles, leading to the onset of presbyopia in the fourth decade of life.

1.2.2.1 Gullstrand's Theory of the Intracapsular Accommodation Mechanism

Gullstrand attributed part of the increase in lens power with accommodation to the change in refractive index distribution, which he referred to as the intracapsular accommodation mechanism (IAM). It was based on a four-surface crystalline lens model (a cemented triplet), with one refractive index for the cortex and a different, higher index for the nucleus. To understand the effects of the internal structure of the lens on accommodation, Gullstrand compared this

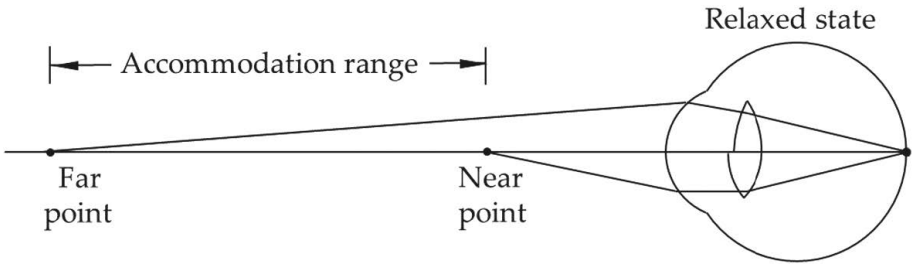

Figure 1.5: Near and far points of the eye. [33]

model to an equivalent two-surface homogeneous lens with a constant refractive index, neq, that yields the same refractive power. During accommodation, the curvature change in the four-surface lens model resulted in a more significant increase in lens power compared to the equivalent two-surface homogeneous lens (fig. 1.6). Put differently, the homogeneous lens's refractive index would have to increase to match the increase in power of the four-surface lens [34]. It is important to note that the equivalent index is not a physical refractive index but an imaginary concept. Gullstrand's four-surface crystalline lens model challenges the traditional understanding of accommodation. It suggests that the relationship between lens power and refractive index is not linear and that the simplified two-surface lens may not accurately match the accommodation changes produced by the four-surface lens.

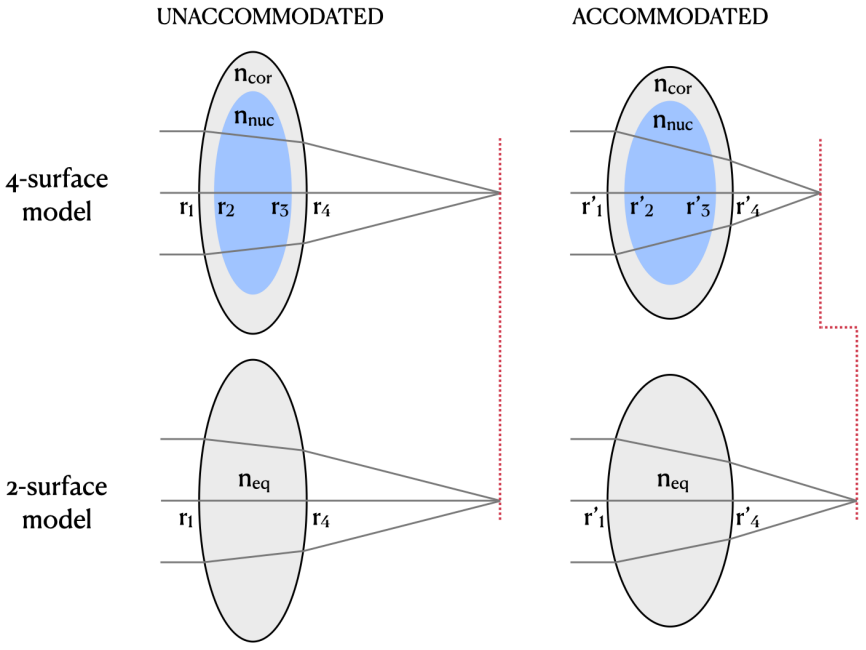

Figure 1.6: Intracapsular accommodation mechanism [4]

Gullstrand's six-surface eye model, which includes two surfaces for the cornea and four for the crystalline lens (separating the lens cortex and nucleus), has influenced subsequent two-surface accommodating lens models that feature an equivalent refractive index that increases during accommodation [35–37]. More advanced models with gradient index (GRIN) lenses have demonstrated

that GRIN media enhances refractive power during accommodation [38, 39], and other studies point to a positive increment in the equivalent refractive index (IAM) in non-human primate lenses [40]. However, some studies have challenged the existence of an IAM. For instance, Hermans et al. [41] argued that Gullstrand's model might overestimate lens power due to not accounting for accommodative lag. Other models, like Garner and Smith's GRIN lens [42], do not indicate an IAM. Relatively recent in-vivo Scheimpflug imaging [43] has shown less change in the radii of curvature of the lens nucleus surfaces during accommodation than Gullstrand proposed, suggesting a potential "intracapsular mechanism of disaccommodation" instead [34]. Table 1 presents IAM values for various eye models. The increase in the equivalent refractive index per dioptre of accommodation (IAM > 0) ranges from 0.00078 to 0.00141 [35, 36, 44], contrasting with recent and not-so-recent studies that report a more negligible increase [41, 42].

AUTHOR	MODEL	RELAXED		ACCOMMODATED		VARIATION	IAM
		P(D)	n_{eq}	P(D)	n_{eq}	$\frac{\Delta n_{eq}}{\Delta P}$ (10^{-3})	
Gullstrand [35]	4 surf.	19.11	1.4085	33.06	1.4260	1.25	+
Le Grand [35]	2 surf.	21.78	1.4200	30.70	1.4270	0.78	+
Navarro [36]	2 surf.	21.55	1.42	34.30	1.438	1.41	+
Hermans [41]	4 surf.	–	1.4345	–	1.4345	0	No
Garner [42]	GRIN	21.75	1.4277	30.65	1.4277	0	No

Table 1.1: Intracapsular accommodation mechanism findings across different accommodating studies and lens models.

1.2.3 The Aging Lens

The most significant age-related optical changes in the eye happen in the lens. Its shape, size, and mass undergo substantial alterations, its capacity to change shape (accommodation) decreases, and its ability to transmit light diminishes significantly, especially at shorter wavelengths.

Most of the increase in lens thickness happens before the age of 50, primarily due to the thickening of the nucleus. This thickening is associated with increased curvature of the anterior surface, a forward shift of the lens center, and a reduction in anterior chamber depth. Changes in the curvature of the posterior surface are less pronounced than the anterior surface. The growth of the lens is driven by the continuous proliferation of epithelial cells near the equatorial region. These cells elongate towards the anterior and posterior poles of the lens from all around the lens periphery and eventually become lens fibers that stack over the older fibers. Moving from the surface to the center of the lens is akin to traveling through time from the present to the past, transitioning from the newest to the oldest lens layers. Over time, all these stacked layers compress and harden the lens nucleus and increase its weight.

As the lens shape changes with age, one might expect an increase in refractive power due to the steepening of the lens surfaces. However, the general trend

is the opposite, with the eye exhibiting a hypermetropic shift, i.e., a power loss of about two diopters between the ages of 30 and 60, a phenomenon known as the lens paradox. In younger eyes, the refractive index of the lens decreases from the center outward, which significantly contributes to the lens's overall power. As we age, the gradient index profile of the lens flattens near its center. It becomes steeper towards the edges, reducing the contribution of the gradient index to the overall lens power. These internal changes within the lens counterbalance the increased curvature of the lens surfaces, thereby explaining the decrease in lens power associated with aging. Although there is general agreement that the GRIN structure may explain the lens paradox, to our knowledge, there is no quantitatively precise model (in terms of both anatomy and optical performance) of the aging lens. This gap was a primary motivation for developing the GRINCU lens model.

With aging, there is also a loss in UV and visible wavelength transmittance, leading to lens yellowing. Additionally, beginning around age 40, there is an increase in both forward and backward light scattering, along with heightened fluorescence.

1.2.3.1 Presbyopia

Presbyopia is the physiological decline in the eye's ability to accommodate. Optically, it is characterized by the progressive movement of the near point away from the eye until it aligns with the far point. Symptoms typically begin to appear around the age of 40. However, the exact onset can vary based on an individual's refractive error, the nature of their close work, stature, and potentially genetic and environmental factors. The aging of the visual system is the primary cause of presbyopia, with the main culprit being the loss of elasticity, mainly in the nucleus of the crystalline lens, due to the changes in its size, shape, and structure. The ciliary muscle seems to keep most of its function, so it does not seem to be a relevant factor in the loss of accommodative ability. By the fifties, accommodation is entirely lost, well before most other physiological functions show any significant decline.

Presbyopia translates into difficulty focusing on close objects, eye strain, and fatigue, especially during tasks requiring close focus, increased lighting, and blurred near vision. Common treatments include reading glasses that move the near point closer to the eye, bifocal or progressive lenses, or surgical procedures such as LASIK or intraocular lens implantation.

1.2.3.2 Cataracts

Cataracts are a common age-related condition characterized by the cloudification of the crystalline lens, resulting from the breakdown and aggregation of lens proteins (see fig. 1.7 for a microscope image of a cataract). This process usually begins after age 40, with more noticeable vision changes typically occurring after age 60. The aggregation of proteins within the lens leads to increased inhomogeneity (variations in the refractive index) and anisotropy (directional dependence of optical properties), affecting the lens's overall transparency and functionality. The impact of cataracts on vision can be understood in terms of

light scatter: Forward scatter causes a veiling glare, where light is dispersed forward through the lens. This glare can obscure vision by reducing contrast and making it difficult to see clearly, especially in bright lighting. Backscatter reduces the amount of light that reaches the retina. It effectively diminishes the clarity of the image formed on the retina, as when one looks through a dense fog, strongly impairing vision.

Cataract treatment often involves surgical procedures such as phacoemulsification, where the cataractous lens is replaced with an artificial intraocular lens (IOL) that helps restore transparency and improve vision. For individuals with high myopia and hyperopia, IOLs can be implanted alongside the existing natural lens. However, during cataract surgery, the natural lens is typically removed before the IOL is inserted. The optical characteristics of IOLs differ significantly from those of spectacle and contact lenses because they are situated within the eye. Therefore, any optical treatment involving IOLs must consider the entire eye's optics, including internal distances, refractive indices, and corneal surface powers. Unlike spectacle lenses, but similar to contact lenses, IOLs move with the eye. IOLs, like contact lenses, address many issues associated with high positive-powered spectacle lenses used after cataract extraction, such as weight, high spectacle magnification, high off-axis power errors, and restricted visual field through the lenses. Another motivation for this thesis was creating a realistic and precise lens model that could enhance the design of intraocular lenses (IOLs).

1.2.4 Optical Quality

The main factor affecting the optical quality of the eye is optical aberrations. Aberration refers to the deviation of a ray from its ideal trajectory. When considering a bundle of rays or their associated wavefront, these deviations can be categorized into modes based on their order. First and second-order aberrations relate to clinical refractive errors, which can be corrected using prisms

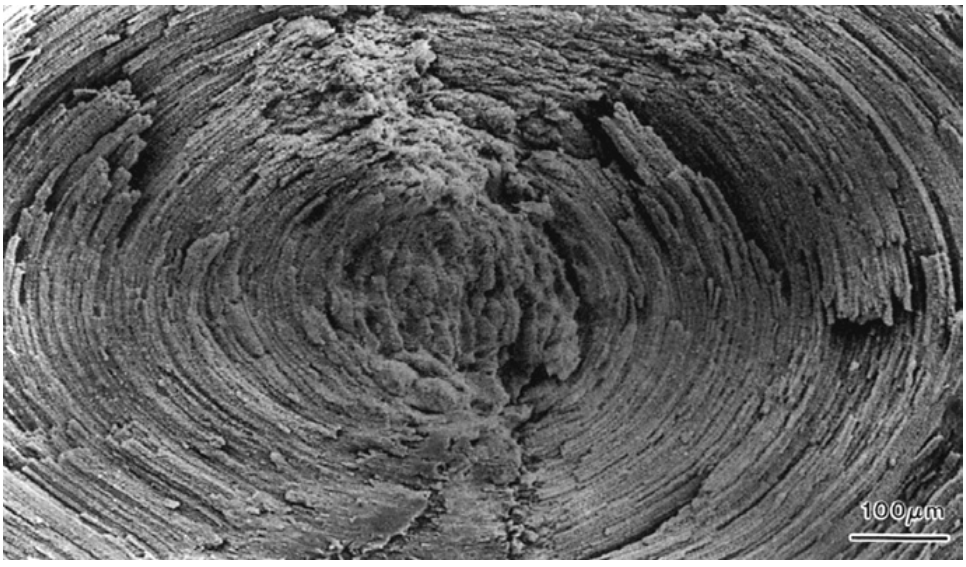

Figure 1.7: Electron microscope imaging of a cataract. [45]

or lenses, respectively. However, conventional optical elements can not correct higher-order aberrations. In a typical population, the primary aberrations are the common second-order spherocylindrical focus errors, known as refractive errors. Higher-order aberrations constitute a relatively minor portion, accounting for approximately 10% of the eye's total aberrations. These higher-order aberrations tend to increase with age and exhibit mirror symmetry between the right and left eyes.

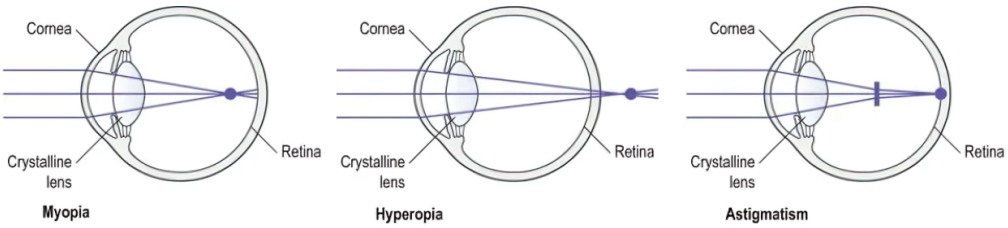

Figure 1.8: Ametropias of the eye.

- *Emmetropia* refers to the normal refractive state of the eye and is the condition by which incoming light rays come into focus in the retina and form a clear image. The far point of an emmetropic eye is at infinity, although in practice, a person may be considered emmetropic if they have a refractive error of 0.25 D or less.

- *Ametropia* or refractive error is defined as any alteration where the eye's far point is not at infinity, therefore reducing visual acuity. Ametropias can be classified into spherical refractive anomalies, where the refractive error is the same in all meridians, and astigmatic refractive error, where it depends upon the meridian.

- *Spherical refractive errors* are those that can be compensated with spherical lenses. They are due to a mismatch between the eye's refractive power and axial length. In myopia or nearsightedness, the far point of the eye is at a finite distance, causing the focal point to be in front of the retina (fig. 1.8, left). Myopia can be corrected by placing a diverging spherical lens in front of the eye to move the focal point of the system to its correct position on the retina. In hyperopia or farsightedness, the far point is behind the eye, with the focal point positioned behind the retina (fig. 1.8, center). Hyperopia is corrected by a converging lens. According to its etiology, ametropia can be classified into axial ametropia, where the eye is abnormally long (myopia) or short (hyperopia), or refractive ametropia, caused by an abnormal refractive power of the lens or cornea— excessive refracting power leading to myopia and deficient refractive power leading to hyperopia. Axial ametropia is more prevalent than the refractive type.

- *Astigmatism* is a curvature defect in the eye's refractive surfaces that prevents the convergence of light rays to a single focus point. Different radii of curvature of the different meridians (lack of rotational symmetry) of the refractive elements result in unequal refraction of the light rays and the creation of two focal lines perpendicular to each other and at

different distances from the retina (fig. 1.8, right). Astigmatism may also arise when one or more surfaces are transversely displaced or tilted. In any case, astigmatism may be corrected with cylindrical lenses. For this reason, clinicians often use the term cylinder instead of astigmatism. Toric lenses allow the combination of sphere and cylinder corrections.

- *Presbyopia,* as detailed in Section 1.2.3.1, is not strictly classified as ametropia but rather as a refractive anomaly where the near point recedes away from the eye due to the age-related reduction in amplitude of accommodation.

1.2.4.1 Higher-Order Aberrations

Here, we will address only the most relevant higher-order aberrations of the eye.

MONOCHROMATIC ABERRATIONS

- *Spherical aberration (SA)* is the dominant monochromatic optical aberration of the human eye. It refers to the lack of coincidence of focus between peripheral and paraxial rays that results from the lens's surface being spherical. Typically, the peripheral rays focus in front of the central rays, leading to positive or undercorrected SA, which tends to shift toward negative spherical aberration during accommodation. Sometimes, negative or overcorrected SA is also found in the unaccommodated eye. SA tends to produce rotationally-symmetric blurring of an on-axis image point.
- *Coma* occurs when light rays from an off-axis point source enter the eye through different parts of the pupil and fail to converge at a single focal point. Instead, one side of the beam focuses slightly before or after the other, creating an asymmetric blur that resembles the shape of a comet—sharp on one side and gradually trailing off on the other. In an ideal, rotationally symmetric optical system, this effect, called off-axis coma, increases with field angle. However, coma can also arise from physical decentration or tilting of optical components, such as the cornea or lens. In these cases, the aberration is known as misalignment coma, and it remains relatively constant across the field. It is commonly observed in patients with keratoconus, decentered corneal grafts, or off-center laser ablations.
- *Astigmatism* refers to the formation of two separate focal lines at different distances, rather than a single focal point, when off-axis light rays enter obliquely relative to the central axis of the eye. This occurs when the optical surface exhibits two different radii of curvature in orthogonal meridians, resulting in two distinct powers: one in the tangential plane and another in the sagittal plane. Radial astigmatism increases either with the toricity of the optical surfaces or with increased obliquity of the incident light, and it is also susceptible to accommodative stimulus levels for the most oblique rays. Pupil size affects the length of the focal lines.
- *Astigmatism* refers to the formation of two distinct focal lines—one tangential and one sagittal—rather than a single focal point. This can arise

through different mechanisms. The most common form in the human eye is due to toric optical surfaces, such as the cornea or lens, which exhibit different radii of curvature in orthogonal meridians. This surface-based astigmatism is present even for on-axis rays and remains relatively constant across the visual field.

In contrast, even in a perfectly centered and rotationally symmetric optical system, astigmatism can occur for off-axis rays due to differences in optical path length between the tangential and sagittal planes. This field-dependent form—known as oblique or radial astigmatism—increases approximately with the square of the field angle. It is also influenced by pupil size and accommodation, particularly for highly oblique incident rays.

CHROMATIC ABERRATIONS

- *Longitudinal chromatic aberration (LCA)* arises from different wavelengths focusing to varying distances due to variations in refractive index with wavelength. The refractive indices of the ocular media decrease as the wavelength increases, resulting in the eye being myopic for shorter wavelengths and hyperopic for long wavelengths. The total LCA of the human eye over the visible spectrum is approximately 2D. Longitudinal chromatic aberration may cause some on-axis retinal image defocus in white light, which is slightly reduced with smaller pupil diameters.
- *Transverse chromatic aberration (TCA)* causes different magnifications for different wavelengths. In the eye, it is usually associated with decentration between optical surfaces, especially of the pupil relative to the optical axis.

1.3 OPTICAL MODELS OF THE EYE

Understanding the link between structure and function is essential for comprehending the optical and dynamic properties of the eye and lens. To achieve this, an optical eye model must balance simplicity and fidelity to a natural eye's intricate structure and performance. This consideration applies to the entire optical system of the eye and, more specifically, to the crystalline lens.

The model should:

- Mimic the lens's optical properties, including its refractive power and ability to alter shape during accommodation.
- Include age-related changes, such as reduced accommodative power and presbyopia.
- Be adaptable to individual biometric parameters, allowing customization based on specific measurements from a person's eye.

Considering the above requirements, the model needs to adapt to the significant intersubject variability found in the population, as well as the short-

and long-term changes associated with accommodation and aging. While maintaining physiological accuracy is essential, models should be straightforward enough for practical use in clinical and research settings. Meeting these criteria, an eye model can offer valuable insights into the lens's structure-function relationship, aiding in the development of improved diagnostic tools, treatments, and personalized refractive corrections.

The first accurate paraxial schematic eye model is credited to Listing [46], who in 1851 proposed a simplified eye comprised of a single-surface cornea and a homogeneous lens. Since then, various paraxial schematic eye models with different levels of complexity have been developed. The most straightforward schematic eyes are *reduced* models [47–49] with a single refractive surface and a homogeneous index throughout the eye volume. *Simplified* models [47, 48, 50] include a single-surface cornea and a two-surface lens and are more anatomically correct, allowing for accommodated states and a more accurate prediction of cardinal points. Finally, *exact* eye models [35, 50, 51] include a two-surface cornea and a two-surface homogeneous lens or a four-surface lens with a homogeneous nucleus and a homogeneous cortex, albeit with different refractive indices. While paraxial models can accurately predict the Gaussian optical properties and the longitudinal chromatic aberration of the human eye [52, 53], they are poor predictors of spherical aberration, astigmatism, and distortion [33]. Improving the agreement between schematic eye models and experimental real-eye performance requires aspherizing the surfaces [54–56], heterogenizing the crystalline lens [57–59], and accounting for chromatic dispersion [60]. Rapid advances in non-invasive technologies for measuring ocular aberrations [61] and optical biometry [62] in vivo have promoted the development of more accurate and realistic eye models adaptive to age [3, 63–66], accommodation [36, 57, 67–69], or both [37, 38, 70].

Gullstrand was the first to propose a model with an inhomogeneous distribution of the refractive index of the lens. Based on contemporary studies, he understood that the lens comprised a "medium of variable index of refraction" [50]. This index exhibited a continuous distribution throughout childhood and puberty but developed discontinuities, observable as light reflexes, by the end of the second decade of life. Gullstrand introduced a six-surface eye model, allocating four surfaces to the lens, thereby dividing it into the nucleus and cortex. Since then, many gradient index (GRIN) crystalline lens models have been proposed. The gradient refractive index (GRIN) distribution of the crystalline lens enhances lens power and contributes to ocular aberrations [59, 71–73] and peripheral power [74]. Most GRIN lens models typically assume a concentric shell configuration of the iso-indicial surfaces (IIS) within the lens [75]. However, the presence of a gradient in the curvatures of the IIS strongly impacts lens power [39]. Developing more realistic and customizable eye models requires lens models adaptable to individual variations. Incorporating both a gradient index and a gradient curvature of the iso-indicial surfaces is crucial to analyzing the effect of the lens's internal structure on the optical performance of the entire eye. Only two recent GRIN models [3, 70] allow for modifying the inner curvature gradient; the GRINCU lens model [3] provides an explicit method for altering the curvature gradient inside the lens.

Refractive calculations for individualized eye treatments require a detailed understanding of the eye's biometric dimensions and optical properties, which generic models fail to provide due to the considerable variability in eye anatomy among individuals. The optical performance of an individual eye is influenced by the shape of its surfaces and the gradient index (GRIN) distribution within the crystalline lens. Ideal assessments would require comprehensive ocular biometric data, which are currently incomplete, with the available data sets lacking crucial lens parameters. Given the bigaussian nature of human ocular biometric parameters [76], a statistical eye model accurately reflecting eye properties is a promising candidate for population modeling. SyntEyes [2] is a platform that generates synthetic biometric data sets with physiologically realistic variations similar to those found in the general population. These virtual eyes eliminate the need for biometric measurements from the end user and provide a valuable resource for vision scientists and clinicians to analyze and simulate the optical properties of the human eye both pre and post-intervention. Another method for modeling individual eyes involves using custom eye models [77]. These models are developed by optimizing an optical model to find the lens topography that best replicates the experimentally measured wave aberration (including both low and high-order aberrations), assuming the lens geometry is unknown.

Eye models have a wide range of applications in academia, clinical settings, and industry. They are vital teaching tools in medical and optometry programs, enhancing students' comprehension of the eye's optical properties. In vision science research, eye models help study the impact of various conditions and diseases, offering deeper insights into ocular issues. In the clinical setting, they contribute to developing advanced diagnostic tools and personalized treatment plans, such as custom contact lenses and intraocular lenses. Industrially, eye models are essential for designing and testing optical devices and driving innovation in vision correction technologies. Integrating optical principles with anatomical and physiological characteristics, effective eye models help professionals across these fields improve understanding, diagnosis, and treatment of various visual conditions, leading to advancements in eye care and optical technology.

1.4 MOTIVATION

The crystalline lens is the most dynamic element in the human visual system. It fulfills the vital role of focusing light on the retina, an essential process for vision. While the relaxed lens contributes to about one-third of the eye's refractive power, it can alter its shape, guided by the ciliary muscles, to focus targets at a wide range of distances. Unlike the cornea, the lens is an adaptive system that experiences short (accommodation) and long-term (aging, presbyopia, and cataracts) changes in its external geometry and internal structure.

Accommodation, a fundamental process through which the lens changes its shape to focus on nearby objects, is a key function that diminishes with age due to continuous lens growth. This gradual loss of accommodative power typically begins early but reaches a functional impact between the ages of 40

and 45, marking the onset of presbyopia and affecting nearly everyone over 45. Cataracts, another common age-related condition, are characterized by the lens's opacification, resulting from changes in the chemistry and physiology of mature lens fibers. They usually appear later in life, with most individuals developing a cataract by age 65 and half the population reporting vision loss due to cataracts between ages 75 and 85. The impact on quality of life is substantial, considering that nearly all individuals over 45 have presbyopia and that more than half of the elderly population may experience significant vision impairment due to cataracts. This understanding of the lens's accommodation process and the effects of aging on vision is not just informative but crucial for comprehensive eye health management, especially as we age. As explained in Section 1.2.3, although there is a general consensus that the GRIN structure may account for the lens paradox, no quantitatively accurate model currently exists that effectively represents the aging lens's anatomy and optical performance. This gap is a primary motivation for developing the GRINCU lens model.

Considering the intricate internal structure of the lens and the changes it undergoes with age and accommodation, studying it presents significant challenges. Nevertheless, extensive research on the lens and its functions has led to various models that aim to clarify its opto-biomechanical properties. As the population ages and life expectancy rises, a thorough understanding of the lens's structure and function becomes increasingly crucial. This endeavor is not solely an academic pursuit but has direct implications for improving personalized refractive correction, such as refractive calculations and IOL design.

1.5 HYPOTHESIS

An effective GRIN lens model must be adaptable enough to account for the statistical variations in the overall population and the long- and short-term changes in the lens optobiometric properties while remaining as simple as possible. Ideally, the model should have a clear physical and optical interpretation, be as intuitive as possible, and accurately represent both the paraxial properties and the optical performance of the human crystalline lens.

The starting hypothesis of this thesis is that the GRINCU (GRIN and GRCU) model of the crystalline lens, which incorporates a gradient curvature of the isoindicial surfaces alongside a gradient refractive index, can accurately describe the optical performance of the human lens and its variations with age and accommodation.

1.6 GOALS

This thesis aims to establish a theoretical framework and specific methods for calculating the optical properties of a model that integrates optical principles with the anatomical and physiological characteristics of the human lens. The specific objectives are summarized below.

- Develop a precise mathematical formulation for the GRINCU refractive index distribution within the lens, ensuring it adapts to its external geometry.
- Implement numerical methods to trace light rays through the GRIN lens and analyze the model's optical performance.
- Model the alterations in lens shape and refractive index distribution during accommodation and quantitatively examine the intracapsular accommodation mechanism within our model.
- Incorporate age-related changes such as lens growth and variations in the refractive index distribution using empirical data from aging lenses, adjusting the GRIN profile to reflect these changes. Address the lens paradox by ensuring the model accurately accounts for the paradoxical changes in lens power with age.
- Customize the GRIN model based on individual biometric data from clinical measurements, such as lens curvature, thickness, and refractive power.
- Validate the model against clinical and experimental data, possibly by comparing predicted optical properties with those measured in human subjects.
- Implement the model in proprietary or public software, creating an interface for clinicians and researchers to input biometric parameters and visualize the optical properties of the GRIN lens.

1.7 ORGANIZATION OF THIS THESIS

This thesis is organized into four main sections: Methods (Chapters 2 to 4), Results (Chapters 5 to 7), Conclusions (Chapter 8), and Spanish translations of each chapter and conclusions (Chapters 9 and 10).

Chapter 1 provides a comprehensive overview of the human eye, focusing on its anatomy, physiology, and key optical characteristics, particularly the crystalline lens's gradient index (GRIN). It discusses the optical quality of the lens, various aberrations, and the changes that occur with accommodation and aging. This chapter also outlines the thesis's motivation, hypothesis, and objectives.

Chapter 2 presents the mathematical formulation of the GRINCU model. Building on Navarro's 2007 concentric iso-indicial surface parametrization, a non-concentric model is developed by introducing a curvature gradient parameter, G. This chapter covers the refractive index distribution, the dispersive properties of the model, and implementation results for a 32-year-old GRINCU lens.

Chapter 3 introduces a ray transfer matrix for onion or shell-type GRIN lenses. The matrix is derived in the continuous limit, allowing the lens power

to be expressed as an integral. An analytical solution for the power of the GRINCU model is also provided.

Chapter 4 describes the implementation of GRINCU lens surfaces using Matlab and C++, enabling finite ray tracing in both RT Lib, a custom ray tracing library for Matlab, and ZEMAX.

Chapter 5 compares the optical performance of different lens models (homogeneous, GRIN, and GRINCU) in synthetically generated eyes (SyntEyes) with identical biometrics. It assesses paraxial properties and aberrations for each lens model individually and also within the context of the entire eye.

Chapter 6 explores lens accommodation by quantitatively explaining Gullstrand's intracapsular accommodation mechanism within the GRINCU model. This includes an analysis of accommodative power and changes in the equivalent refractive index.

Chapter 7 addresses the lens paradox through the GRINCU model. By utilizing experimental data on age-related changes in lens geometry and refractive power, an aging model is implemented to examine the internal changes within the lens and their effects on lens power and the equivalent refractive index.

Chapter 8 presents the thesis's achievements, conclusions, and future lines of work.

Chapter 9 includes summaries of each chapter in Spanish, and Chapter 10 contains the Spanish translation of Chapter 8.

METHODS

2 MODEL FORMULATION

2.1 ISO-INDICIAL SURFACE PARAMETRIZATION

2.1.1 Concentric Model

The GRINCU is a gradient index model of the crystalline lens characterized by a shell-type internal structure of the iso-indicial surfaces (IIS), which fills the entire volume of the lens's anterior and posterior regions. As a parametric model, the GRINCU lens is designed to adapt to any age or accommodative state by modification of its parameters. It is built upon an earlier GRIN model, initially formulated as a cemented lens doublet with concentric conicoid shells [66]. This prior model was also adaptive in the sense that the geometry of the anterior and posterior lens surfaces automatically determined the anterior and posterior shapes of the entire family of IIS. This type of lens model was later termed geometry-invariant [78] or external-surface-following [65]. The GRINCU model incorporates both a gradient in the refractive index (GRIN) and a gradient in the curvatures of the IIS (GRCU) [3]. The conic constant of the external surface of the lens, $Q = -e^2$, determines the shape of the internal shells:

$Q < -1$ for hyperboloids

$Q = -1$ for paraboloids

$-1 < Q < 0$ for oblate ellipsoids

$Q = 0$ for spheroids

$Q > 0$ for prolate ellipsoids

Figure 2.1 illustrates the concentric case for the three central conics: spheres, ellipses, and hyperbolas. For spheres to be concentric, the radius must decrease as the vertex varies along z. For the other conics, however, the semiaxis a changes with z, decreasing for ellipses and increasing for hyperbolas. Note that for spheres, $R = a$; therefore, the condition for concentric conics will be $a(z) = a_0 - \varepsilon z$, where $\varepsilon = +1$ for spheres and ellipses and $\varepsilon = -1$ for hyperbolas. Using the expression of the apical radius of curvature and the conic constant in terms of the semiaxes a and b, $R = +b^2/a$ and $Q = \varepsilon b^2/a^2 - 1$ respectively, it is straightforward to arrive at the general condition for concentric conics.

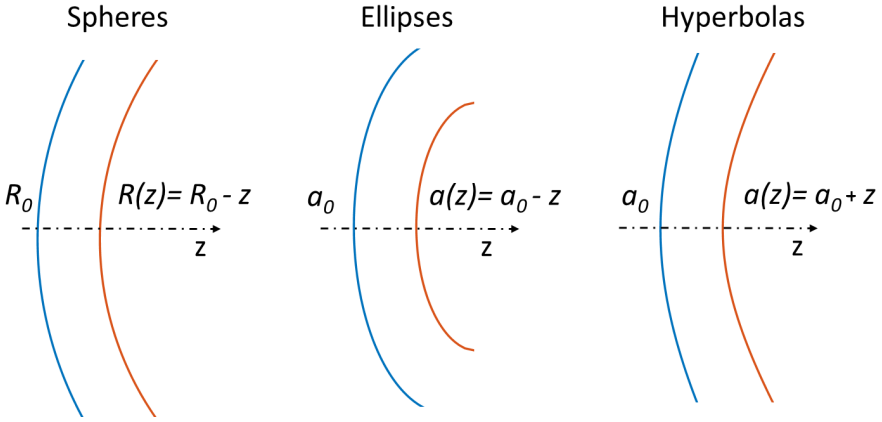

Figure 2.1: Concentric conics.

If R_0 is the apical radius of curvature and Q is the conic constant of the lens's external surface, we have that the apical radius of curvature of a concentric conicoid with vertex at z is:

$$R(z) = R_0 - (Q+1)z \tag{2.1}$$

The concentric iso-indicial surface distribution of the earlier concentric model (see fig. 2.2, left) relies on a normalized radius r^2 where $0 \leqslant r \leqslant 1$, and it can be represented as a conicoid for both the anterior and posterior regions of the lens. For the anterior surface, the conicoid has its vertex at the origin and its center at $\Delta_{ant} = \varepsilon a$. The posterior surface vertex is at $z = t$, with center at $\Delta_{pos} = t + \varepsilon a$ from the vertex, resulting in the following equations:

$$r^2_{ant} = \frac{1}{f_{ant}}\left(\frac{(z-\Delta_{ant})^2}{a^2_{ant}} + \varepsilon_{ant}\frac{\omega^2}{b^2_{ant}} - O_{ant}\right) \tag{2.2a}$$

$$r^2_{pos} = \frac{1}{f_{pos}}\left(\frac{(z-\Delta_{pos})^2}{a^2_{pos}} + \varepsilon_{pos}\frac{\omega^2}{b^2_{pos}} - O_{pos}\right) \tag{2.2b}$$

Where z is the axial coordinate, $\omega^2 = x^2 + y^2$ is the radial coordinate, a, b are the semiaxes of the respective conics, and f and O serve as a scaling factor and an offset, respectively, to ensure that the normalized radius r^2 remains within its valid range [66].

We will now reformulate the concentric model by utilizing the apical radii of curvature of the anterior and posterior surfaces, R_{as}, R_{ps} respectively, and their conic constants, Q_a, Q_p. Let us consider the general equation for two conic surfaces, one with its vertex positioned at the origin ($z = 0, \omega = 0$) and the other one with vertex at an offset matching the lens thickness ($z = t, \omega = 0$), applicable to the anterior and posterior surfaces of the lens:

$$(Q_a+1)z^2 - 2R_{as}z + \omega^2 = 0 \tag{2.3a}$$

$$(Q_p+1)(z-t)^2 - 2R_{ps}(z-t) + \omega^2 = 0, \tag{2.3b}$$

Where the lens thickness t is the sum of the axial thicknesses of the anterior and posterior regions of the lens, $t = t_a + t_p$. The model proposed by Navarro et al. (2021, 2007) posits that each internal iso-indicial surface (IIS) corresponds

to a homogeneous shell with a uniform refractive index and that any IIS is a displaced and scaled replica of the lens's external surface. This distribution of iso-indicial surfaces consists of an anterior and posterior hemisphere, forming a cemented doublet. By substituting eq. (2.3) into eq. (2.2), we can reformulate r^2 in terms of the apical radii of curvature and conic constant.

$$r^2_{ant} = \frac{1}{f_{ant}}\left[(Q_a+1)z^2 - 2R_{as}z + \omega^2 - O_{ant}\right] \tag{2.4a}$$

$$r^2_{pos} = \frac{1}{f_{pos}}\left[(Q_p+1)(z-t)^2 - 2R_{ps}(z-t) + \omega^2 - O_{pos}\right] \tag{2.4b}$$

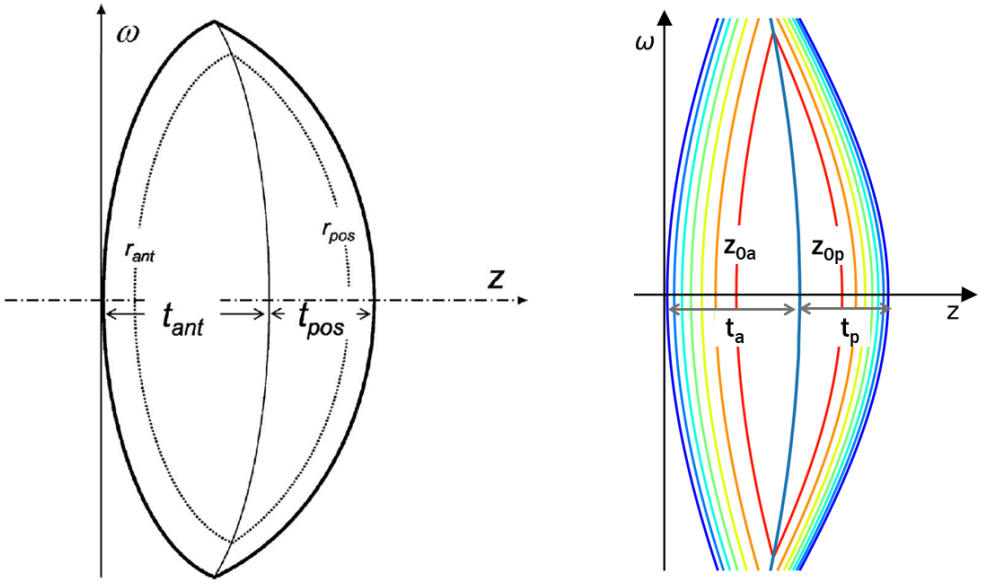

Figure 2.2: Comparison of the IIS parameterizations. *Left:* r^2 (Figure 1 in Ref. [66]). *Right:* z_0.

The parameter r^2 characterizes a set of iso-indicial surfaces, with each value of r^2 representing a distinct IIS, collectively populating the lens volume. However, in the current formulation, we utilize the variable z_0, which denotes the coordinate where a specific IIS intersects the z-axis ($z = z_0, \omega = 0$) [3]. Given that r^2 remains constant across the entire IIS, we can specify the IIS expression at the intersection point ($z = z_0, \omega = 0$) as follows:

$$r^2_{ant} = \frac{1}{f_{ant}}\left[(Q_a+1)z_0^2 - 2R_{as}z - O_{ant}\right] \tag{2.5a}$$

$$r^2_{pos} = \frac{1}{f_{pos}}\left[(Q_p+1)(z_0-t)^2 - 2R_{ps}(z-t) - O_{pos}\right] \tag{2.5b}$$

Combining eqs. (2.4) and (2.5) for each the anterior and posterior regions yields a general expression for conicoid surfaces parametrized in z_0, where each value of z_0 defines one IIS:

$$(Q_a+1)(z-z_0)^2 - 2[R_{as} - (Q_a+1)z_0](z-z_0) + \omega^2 = 0 \tag{2.6a}$$

$$(Q_p+1)(z-z_0)^2 - 2[R_{ps} - (Q_p+1)(z_0-t)](z-z_0) + \omega^2 = 0 \tag{2.6b}$$

The second terms in both eqs. (2.6a) and (2.6b) are an explicit expression of the concentric configuration of this earlier model and match the geometries shown in fig. 2.1:

$$R_a(z_0) = R_{as} - (Q_a + 1)z_0 = R_{as} - g_a z_0 \tag{2.7a}$$
$$R_p(z_0) = R_{ps} - (Q_p + 1)(z_0 - t) = R_{ps} - g_p(z_0 - t) \tag{2.7b}$$

2.1.2 General Non-Concentric Model

The GRINCU model was designed to incorporate more general iso-indicial surface configurations with non-concentric shells. Therefore, we introduced a unitless curvature radius gradient parameter G that multiplies $(Q + 1)$, resulting in a net curvature gradient $g = G(Q + 1)$. Note that the concentric configuration corresponds to a value of $G = +1$. Accordingly, we can rewrite eq. (2.7) incorporating the curvature gradient parameter for the anterior and posterior sections of the lens, respectively:

$$R_a(z_0) = R_{as} - G_a(Q_a + 1)z_0 = R_{as} - g_a z_0 \tag{2.8a}$$
$$R_p(z_0) = R_{ps} - G_p(Q_p + 1)(z_0 - t) = R_{ps} - g_p(z_0 - t), \tag{2.8b}$$

Where g_a and g_p are the net curvature gradients in the anterior and posterior regions. Replacing these expressions for $R_a(z_0)$, $R_p(z_0)$ in eq. (2.6) and solving for z_0, we obtain the expression for the surface profile of a biconvex IIS that crosses the z-axis at z_{0a} and z_{0p}:

$$z_{0a} = \frac{R_{as} + [g_a - (Q_a + 1)]z - \sqrt{(R_{as} - g_a z)^2 + [2g_a - (Q_a + 1)]\omega^2}}{2g_a - (Q_a + 1)} \tag{2.9a}$$
$$z_{0p} = \frac{R_{ps} + [g_p - (Q_p + 1)]z + g_p t + \sqrt{(R_{ps} - g_p(z - t))^2 + [2g_p - (Q_p + 1)]\omega^2}}{2g_p - (Q_p + 1)} \tag{2.9b}$$

It is important to note that eqs. (2.2) and (2.9) offer different ways to parameterize the IIS, either using r^2 or z_0. However, eq. (2.9) enables the direct incorporation of the curvature gradient parameter G. This curvature gradient parameter's range of validity is determined by the external geometry of the lens. Setting the condition that $R_a(z_0)$ and $R_p(z_0)$ do not change sign in their respective intervals–$(0, t_a)$ and (t_a, t)–, we obtain:

$$G_a < \frac{R_{as}}{(Q_a + 1)t_a} \tag{2.10a}$$
$$G_p < \frac{-R_{ps}}{(Q_p + 1)t_p} \tag{2.10b}$$

Or, using the net gradient:

$$g_a < \frac{R_{as}}{t_a} \tag{2.11a}$$
$$g_p < \frac{-R_{ps}}{t_p} \tag{2.11b}$$

2.1.2.1 Paraboloids

Rotationally symmetric paraboloids have a conic constant of $Q = -1$, and their apical radius of curvature is proportional to their semilatus rectum, l, with $R = 2l$. By substituting $Q = -1$ into eqs. (2.8a) and (2.8b), we derive the following expressions for z_{0a} and z_{0p}:

$$z_{0a} = z - \frac{\omega^2}{2R_{as}} \tag{2.12a}$$

$$z_{0p} = z - \frac{\omega^2}{2R_{ps}} \tag{2.12b}$$

This configuration is akin to setting $G = 0$, as the net gradient is effectively zero in both instances, given that $g = G(Q+1) = 0$. Consequently, for the iso-indicial surface distribution, the apical radius of curvature remains constant across all values of z_{0a} and z_{0p}. In other words, the iso-indicial surfaces are parallel to the lens's anterior and posterior external surfaces within their respective regions.

$$R_a(z_0) = R_{as} \tag{2.13a}$$

$$R_p(z_0) = R_{ps} \tag{2.13b}$$

2.1.3 General Non-rotationally Symmetric Model

We will now generalize the rotationally symmetric two-axis conicoid configuration to the more general three-axis case. Let us replace ω^2/b^2 with its non-rotationally symmetric (general) version $x^2/c^2 + y^2/d^2$ in eq. (2.2a). For the anterior surface of the lens, with its apex at the origin ($fr^2 + O = 1$) and center at $\Delta = \varepsilon a$, we have:

$$\frac{(z-\Delta)^2}{a^2} + \varepsilon\left(\frac{x^2}{c^2} + \frac{y^2}{d^2}\right) = 1 \tag{2.14}$$

The rotationally symmetric conicoid is characterized by two parameters, either semiaxes (a, b) or apical radius and conic constant (R, Q), depending on the formulation. The non-rotationally symmetric conicoid, on the other hand, is defined by the three semiaxes (a, c, d). To incorporate surface astigmatism, we introduce a parameter D, allowing the surface to be described by three alternative parameters (R, Q, D). For simplicity, let us assume that the maximum and minimum radii of curvature are along the x- and y-axis. Then, we can define $D = (R_x - R_y)/2$ as the deviation, $R = (R_x + R_y)/2$ as the average curvature radius, and $Q = (Q_x + Q_y)/2$ as the average conic constant [3]. With a change of variables, $a = R/(Q+1)$, $\varepsilon c^2 = R_x^2/(Q_x+1)$ and $\varepsilon d^2 = R_y^2/(Q_y+1)$ and further reorganizing the equation in terms of (R, Q, D), we arrive at:

$$\omega^2 = R\left(\frac{x^2}{R+D} + \frac{y^2}{R-D}\right) \tag{2.15}$$

Ultimately, the surface can be rotated by any angle θ around the optical axis. By applying a counterclockwise rotation matrix $\boldsymbol{\nu}' = R(-\theta)\boldsymbol{\nu}$ to the vector $\boldsymbol{\nu} = (x, y)$, we derive the expression for a general spherocylindrical IIS.

$$\omega^2 = R\left(\frac{(x\cos\theta + y\sin\theta)^2}{R+D} + \frac{(-x\sin\theta + y\cos\theta)^2}{R-D}\right) \tag{2.16}$$

The general non-rotationally symmetric IIS is characterized by four parameters: R, commonly referred to as the radius of the sphere; D, the radius of the cylinder; θ, the orientation axis of the cylinder; and Q, the average conic constant. To apply this geometry, we substitute ω^2 in eqs. (2.9a) and (2.9b) for ellipsoids or hyperboloids, or in eqs. (2.12a) and (2.12b) for paraboloids.

2.2 REFRACTIVE INDEX DISTRIBUTION

Most experimental measurements [19, 21, 79, 80] and models [59, 66, 70, 81] indicate that the axial distribution of the refractive index in the anterior and posterior regions adheres to a power law. The GRINCU lens [3] specifies the refractive index distributions for the anterior and posterior regions using Eq. (13) in their publication, with the parameter $z_0 = z_0(z, \omega)$ representing the iso-indicial surfaces for varying values of n. In the paraxial region, it is assumed that the index distribution is solely dependent on z, hence $z_0 = z_0(z, 0)$:

$$n(z_0) = \begin{cases} n_a(z_0) = n_c + \delta_n(s_a)^p \text{ for } z \leqslant z_{0a} \leqslant t_a \\ n_p(z_0) = n_c + \delta_n(s_p)^p \text{ for } t_a < z_{0p} \leqslant t \end{cases} \tag{2.17}$$

Where $s_a = 1 - z_{0a}(z, \omega)/t_a$ and $s_p = (z_{0p}(z, \omega) - t_a)/t_p$ are normalized in such a way that s_a and s_p equal 1 at the lens surface and 0 at the lens core, n_c is the maximum refractive index of the lens, $\delta_n = n_s - n_c$ is the refractive index difference between the lens core and surface (n_s), t_a and t_p are the anterior and posterior thicknesses, and $t = t_a + t_p$ is the total axial thickness of the lens. Exponent p is an age-dependent parameter that determines the power law of the refractive index distribution inside the lens. The generic expression of z_{0a} and z_{0p} is provided in eqs. (2.9a) and (2.9b) above.

2.2.1 Gradient of n

The GRINCU model is formulated in cylindrical coordinates (z, ω). Therefore, we need to apply the chain rule to determine the partial derivatives in Cartesian coordinates. After that, we can calculate the refractive index gradient, which is represented as $\nabla n = \left(\frac{\partial n}{\partial x}, \frac{\partial n}{\partial y}, \frac{\partial n}{\partial z}\right)$.

$$\frac{\partial n}{\partial x} = \frac{dn}{dz_0} \cdot \frac{dz_0}{d\omega^2} \cdot \frac{d\omega^2}{dx} \tag{2.18a}$$

$$\frac{\partial n}{\partial y} = \frac{dn}{dz_0} \cdot \frac{dz_0}{d\omega^2} \cdot \frac{d\omega^2}{dy} \tag{2.18b}$$

$$\frac{\partial n}{\partial z} = \frac{dn}{dz_0} \cdot \frac{dz_0}{dz} \tag{2.18c}$$

The refractive index depends on z_0; its derivatives in the anterior and posterior regions are:

$$\frac{dn}{dz_{0a}} = -\frac{\delta_n \cdot p}{t_a}\left(1 - \frac{z_{0a}}{t_a}\right)^{p-1} \tag{2.19a}$$

$$\frac{dn}{dz_{0p}} = \frac{\delta_n \cdot p}{t_p}\left(\frac{z_{0p} - t_a}{t_p}\right)^{p-1} \tag{2.19b}$$

In this context, δ_n represents the difference in refractive index between the surface of the lens and its core, while p denotes the exponent of the power law. The term t_a refers to the anterior axial thickness of the lens.

The parameter z_0 is defined as a function of the cylindrical coordinates, specifically $z_0(z, \omega^2)$. Consequently, two sets of derivatives are necessary: relative to z.

$$\frac{dz_{0a}}{dz} = \frac{1}{2G-1}\left(G-1+ + \frac{G(R_{as} - G(Q_a+1)z)}{\sqrt{(R_{as}-G(Q_a+1)z)^2 + (2G-1)(Q_a+1)\omega^2}}\right) \tag{2.20a}$$

$$\frac{dz_{0p}}{dz} = \frac{1}{2G-1}\left(G-1- - \frac{G(R_{ps} + G(Q_p+1)(t-z))}{\sqrt{(R_{ps}+G(Q_p+1)(t-z))^2 + (2G-1)(Q_p+1)\omega^2}}\right) \tag{2.20b}$$

And relative to ω^2:

$$\frac{dz_{0a}}{d\omega^2} = -\frac{1}{2\sqrt{(R_{as} - G(Q_a+1)z)^2 + (2G-1)(Q_a+1)\omega^2}} \tag{2.21a}$$

$$\frac{dz_{0p}}{d\omega^2} = \frac{1}{2\sqrt{(R_{ps} + G(Q_p+1)(t-z))^2 + (2G-1)(Q_p+1)\omega^2}} \tag{2.21b}$$

Where G represents the curvature gradient parameter, Q_a and Q_p are the conic constants of the anterior and posterior lens surfaces, respectively, and R_{as} and R_{ps} denote their apical radii of curvature.

Lastly, ω depends on the cartesian coordinates (x, y):

$$\frac{d\omega^2}{dx} = R\left(\frac{2\cos\theta(x\cos\theta + y\sin\theta)}{R+D} - \frac{2\sin\theta(-x\sin\theta + y\cos\theta)}{R-D}\right) \tag{2.22a}$$

$$\frac{d\omega^2}{dy} = R\left(\frac{2\sin\theta(x\cos\theta + y\sin\theta)}{R+D} + \frac{2\cos\theta(-x\sin\theta + y\cos\theta)}{R-D}\right) \tag{2.22b}$$

Where R represents the radius of curvature and D is the toricity. It is important to note that the derivatives of ω with respect to x and y have the same formula for both the anterior and posterior lenses. To calculate these derivatives, one must use R_{as} and D_a for the anterior region and R_{ps} and D_p for the posterior region.

2.2.1.1 Paraboloids

The derivatives of n and ω^2 are consistent for all conicoids, including paraboloids. However, the derivatives of z_0 differ from eqs. (2.20) and (2.21).

$$\frac{dz_0}{dz} = 1 \tag{2.23}$$

$$\frac{dz_0}{d\omega^2} = -\frac{1}{2R} \tag{2.24}$$

Where R is the radius of curvature. The equations are identical in form for both the anterior and posterior lens regions; however, R_{as} should be applied to the former, while R_{ps} is used in the latter.

2.2.2 Central Interface

The anterior and posterior surfaces cross the optical axis at coordinates $(z_{0a}, \omega = 0)$ and $(z_{0p}, \omega = 0)$, respectively, converging at an intersection point (z_i, ω_i). In a rotationally symmetric scenario, the intersection of the two halves of the IIS forms a circumference with a radius of ω_i. By definition, both hemispheres of the IIS possess the same refractive index value $n_a(s_a) = n_p(s_p)$. Consequently, the intersection requires equal parameters, $s_a = s_p$.

$$1 - \frac{z_{0a}(z, \omega)}{t_a} = \frac{z_{0p}(z, \omega) - t_a}{t_p} \tag{2.25}$$

The locus of the intersections (z_i, ω_i) of the anterior and posterior hemispheres of each IIS forms a central interface surface [66] that intersects the optical axis at $z_{0a} = z_{0p} = t_a$. Thus, the GRIN lens can be viewed as a cemented doublet with a continuous refractive index at the interface. In non-rotationally symmetric configurations, ω_i depends on (x_i, y_i). To maintain eq. (2.25) in its two-dimensional form, it is sufficient to set the condition that $\omega_{ia} = \omega_{ip}$, which can be achieved by ensuring that $\theta_a = \theta_p$ and $D_p = R_{ps}/R_{as} \cdot D_a$. In contrast with Navarro's 2007 adaptive GRIN model, where the interface's analytical solution is a conic surface (see Eq. (8) in Ref [66]), in the present, more general formulation, the interface surface has no direct algebraic solution. However, it can be computed numerically.

2.2.3 Dispersive Model

The Cauchy equation eq. (2.26) describes the refractive index variation with wavelength by reassigning the refractive index values from $n_d = n(\lambda = 587.56\,\text{nm})$, used in traditional eye models, to n_{555}, which is the wavelength corresponding to the peak spectral sensitivity of the human eye. In the present model, we adopt the (A, B, C, D) coefficients and GRIN lens refractive indices presented in Ref. [38]. The refractive index values for the lens surface and core coefficients proposed in that work were adapted from Navarro et al. 2007 and are based on experimental data [19].

$$n(\lambda) = A + \frac{B}{\lambda^2} + \frac{C}{\lambda^4} + \frac{D}{\lambda^6} + \dots \tag{2.26}$$

The chromatic dispersion model of the GRIN structure assumes that both the refractive indices of the lens surface and core are wavelength-dependent (i.e., $n_s = n_s(\lambda)$ and $n_c = n_c(\lambda)$), resulting in the relationship $\delta_n = n_s(\lambda) - n_c(\lambda) = \delta_n(\lambda)$. Consequently, n_s, n_0, and δ_n follow Cauchy equations, making the index distributions in eq. (2.17) also dependent on the wavelengths: $n_a = n_a(z, \omega, \lambda)$ and $n_p = n_p(z, \omega, \lambda)$. Similar assumptions are applied in other dispersive GRIN models, such as treating the constant term of a polynomial model as a function of λ [63] or using concentric iso-dispersive contours [81].

2.3 NUMERICAL IMPLEMENTATION

Symbol	Unit	Value	Description
G_a	-	-1	Anterior curvature gradient parameter
G_p	-	-1	Posterior curvature gradient parameter
Q_a	-	-4	Anterior conic constant
Q_p	-	-3	Posterior conic constant
R_{as}	mm	$12.7 - 0.058 \times a$	Anterior surface radius
R_{ps}	mm	$-5.9 + 0.013 \times a$	Posterior surface radius
d	mm	4.5	Equatorial semidiameter
t	mm	2.93 $+0.0236 \times a$	Axial thickness
t_a	mm	$0.6t$	Anterior axial thickness
t_p	mm	$0.4t$	Posterior axial thickness
p	-	$2.85 + 1.1 \cdot 10^{-7} \times a^4$	Refractive index power law exponent
n_a	-	1.3374	Aqueous and vitreous refractive index
n_s	-	1.3726	Lens surface refractive index
n_c	-	1.4264 $+3.55 \cdot 10^{-4} \times a$ $-7.5 \cdot 10^{-6} \times a^2$	Lens core refractive index
D_a	-	0, 0.10	Anterior surface toricity
D_p	-	0, 0.10	Posterior surface toricity
θ	rad	$0, \pi/6$	Astigmatism axis

Table 2.1: Lens parameters used in the model implementation. a: age in years.

The GRINCU lens model was implemented in Python to verify the formulation prior to conducting finite ray tracing. For comparative purposes, we have included two examples: a centered, rotationally symmetric setup ($D_a = D_p = 0$ and $\theta = 0$) and an astigmatic lens ($D_a = 0.10R_{as}$, $D_p = 0.10R_{ps}$, and $\theta = 30^0$),

utilizing the lens geometric parameters and refractive index values for a 32-year-old published GRIN lens model [38]. The specific lens geometric and refractive index values applied are detailed in table 2.1. Initially, we determined z_{0a} and z_{0p} for a three-dimensional grid matching the lens dimensions and categorized the points into anterior and posterior regions based on these conditions:

- Points inside the lens: $s_a \leqslant 1$ and $s_p \leqslant 1$
- Central interface: $s_a = s_p$. Note that the interface belongs to both anterior and posterior regions. For computational convenience, we assign it to the anterior region.
- Anterior region: $s_a \geqslant s_p$
- Posterior region: $s_a < s_p$

Next, we computed the refractive index distribution $n(x, y, z)$ and its gradient $\nabla n(\partial n/\partial x, \partial n/\partial y, \partial n/\partial z)$ within a three-dimensional sampling grid at a resolution of 0.01 mm. The equations of the derivatives used for these calculations are detailed in Section 2.2.1.

Figure 2.3 illustrates the axial refractive index distribution $n(z)$ for GRINCU lenses at ages 20, 50, and 80. To simplify the analysis, the lens thickness and central refractive index were kept constant, making the distribution solely dependent on the exponent p. This exponent p influences the gradient's steepness [19, 27, 59, 66, 73, 82, 83]. A higher value of p, corresponding to older ages, results in a broader plateau of constant index at the lens center and a steeper gradient index near the lens edge, thereby reducing the lens power [59].

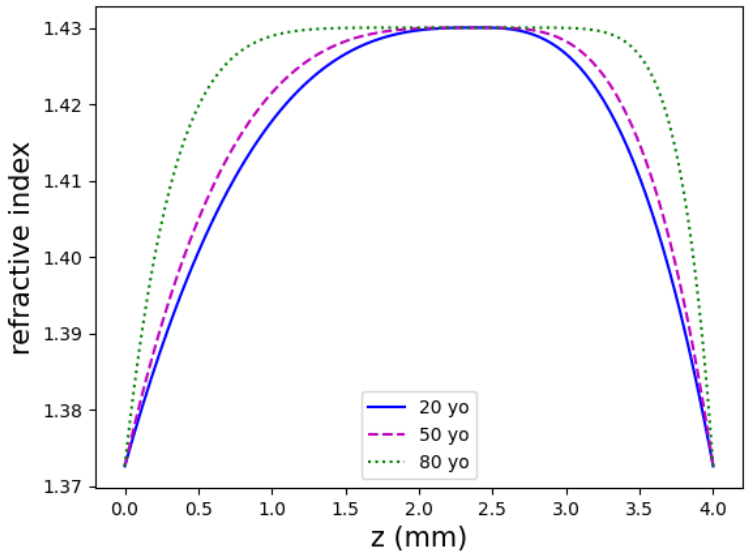

Figure 2.3: Axial distribution of the refractive index for a GRINCU lens of ages 20, 50, and 80 ($p = 3.87$, 4.54, and 8.36, respectively.)

Figure 2.4a depicts a centered, rotationally symmetric lens, while fig. 2.4b illustrates an astigmatic lens with an axis of $\pi/6$. The top row, from left to right, presents the refractive index distribution of the lens observed from a sagittal section at $y = 0$, a transverse section at plane $z = t_a$, and a sagittal section at the

boundary between the anterior and posterior regions of the lens. The bottom row displays the same sections at plane $y = 0$ for the three partial derivatives, which will later be used for finite ray tracing. The distinction between the astigmatic lens and the rotationally symmetric lens is particularly noticeable in the section at $z = t_a$, where the astigmatic lens exhibits a diagonal elongation. The partial derivative $\partial n/\partial y$ at $y = 0$ (bottom center in both figs. 2.4a and 2.4b) is zero for the rotationally symmetric configuration; however, due to the finite sampling grid, we obtained some nonzero values on the order of 10^{-5}, which can be categorized as noise. The same partial derivative was nonzero for the astigmatic lens (fig. 2.4b), as expected from eq. (2.16). Observe the discontinuity in the three partial derivatives at the central interface, where the gradient changes its sign from positive to negative values. This discontinuity could be mitigated through various approaches, such as employing higher-order models for the ISS geometry [78]. However, it is important to note that these discontinuities in the derivatives require careful consideration when performing ray tracing through GRINCU lenses. A potential solution is to handle the anterior and posterior regions separately, effectively treating the lens as a cemented doublet.

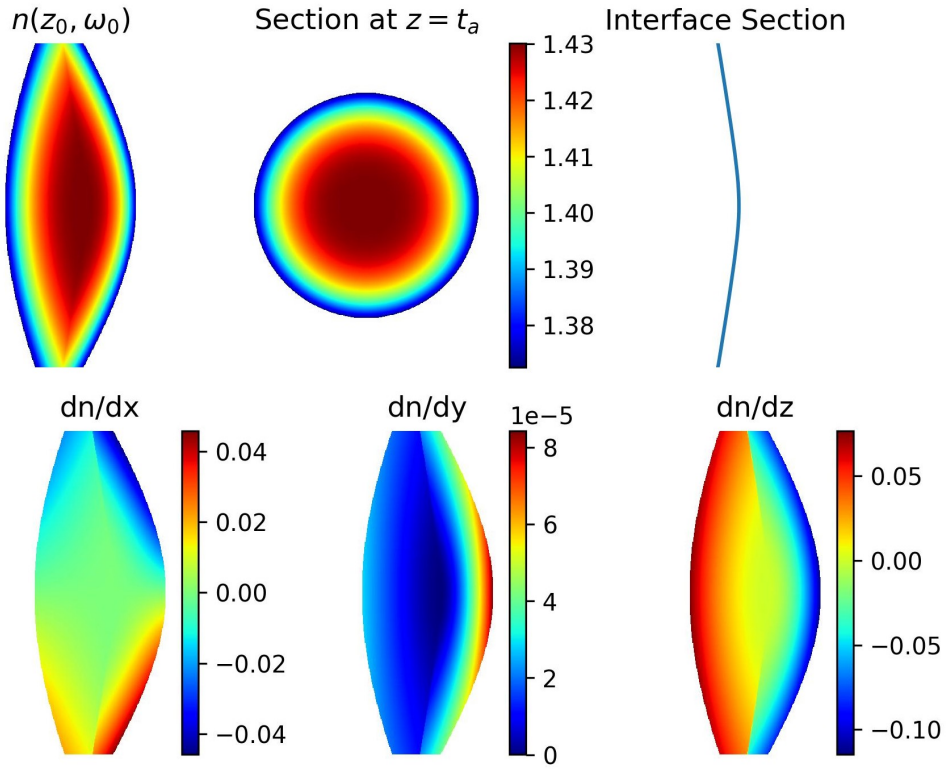

(a) Rotationally symmetric lens.

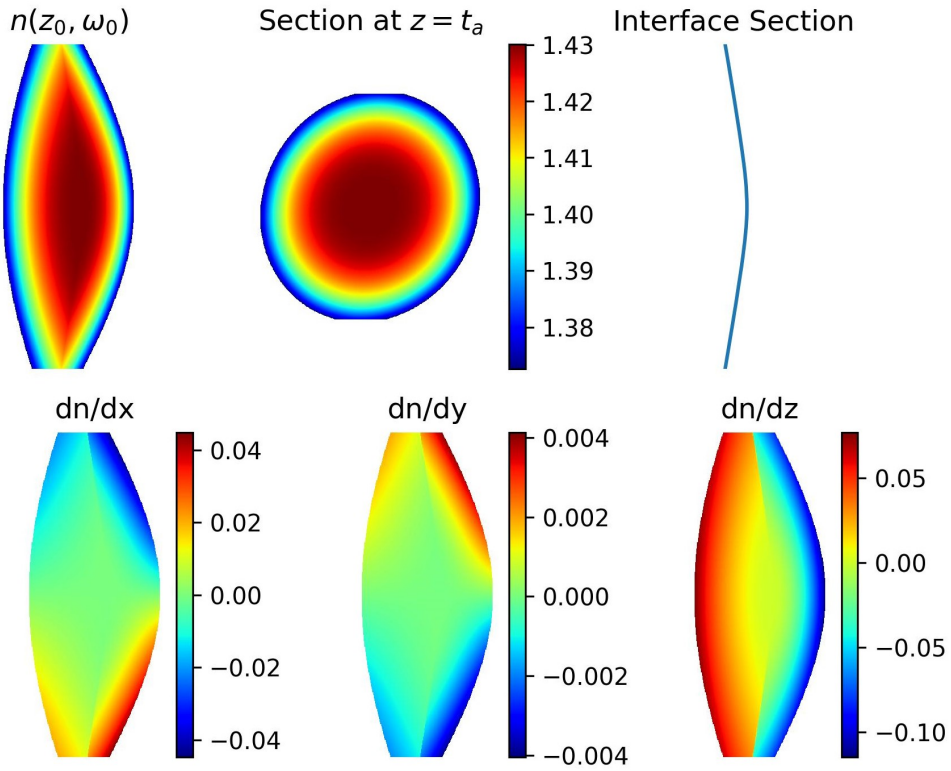

(b) Astigmatic lens with 10% toricity and 30^0-axis.

Figure 2.4: Sections of the refractive index distribution, its derivatives, and the anterior-posterior interface.

3 ANALYTICAL RAY TRANSFER MATRIX

3.1 RAY TRACING IN GRIN LENSES

Ray tracing computation in continuous GRIN lens models is typically approached by solving the Euler–Lagrange equation for the ray trajectories [84]. Paraxial ray tracing is crucial for determining the first-order properties of an optical system, such as focal distances, principal planes, nodal points, and lens power. This method is theoretical and has practical applications in optical design, engineering, and clinical practice, including lens prescription. The ray transfer matrix offers an analytical approximation, significantly reducing computational load compared with other methods.

Different approaches to GRIN lens modeling include Smith and Atchison's [85] parabolic approximation for calculating equivalent lens power and Pérez et al.'s [86] gradient parameter method for tracing axial and field rays through the lens. Díaz [87] later introduced the ray transfer (ABCD) matrix formalism for paraxial ray tracing through different GRIN lens models. Ray tracing in GRIN crystalline lenses is typically approached by considering the lens as either a continuous slab [88] or consisting of a finite number of shells [89]. Shell-type lenses, made up of numerous cemented meniscus lenses, use an onion-type layered structure for ray tracing and do not require other assumptions, such as the parabolic approximation, which is fundamental for the continuous slab method [85, 87]. However, ray tracing through shell-type lenses involves multiplying typically hundreds or even thousands of two-by-two matrices, which can be computationally intensive.

The present chapter introduces a novel unified approach that formulates the ray transfer matrix of onion-type GRIN lenses in the continuous limit. This approach, which treats each iso-indicial surface inside the lens as a refracting optical surface with a known curvature radius and refractive index value, offers a robust and general formulation applicable to various GRIN lens models. The advantage of using a shell-type model is that it is explicit: the analytical expression of the whole family of iso-indicial surfaces, including their curvature radii, is provided. We demonstrate that it is possible to derive an analytical ray transfer (ABCD) matrix for these models, enabling us to perform analytical paraxial ray tracing.

3.2 MATRIX FORMULATION

3.2.1 Discrete Shells

We will now derive the ray tracing matrix for a generic GRIN lens characterized by a refractive index expressed in cylindrical coordinates, $n(\omega, \theta, z)$, where z

stretches along the optical axis. This refractive index is a continuous function that depends solely on z within the paraxial region $n(\omega \simeq 0, \theta, z) \simeq n(z)$. The refractive index $n(z)$ is also differentiable. Its derivative $dn(z)/dz = n'(z)$ exists within the anterior and posterior regions of the lens. From this point forward, we will assume that light travels from left to right toward increasing z values. For a given layer k, the iso-indical surface (IIS) crosses the z-axis at a distance z_k from the origin at the anterior surface vertex. As light traverses this IIS, it refracts at the surface and then travels through the IIS thickness until it reaches the next layer, $k+1$. Since matrices are multiplied in reverse order of the ray path [90], the ray propagation matrix L_k of this layer is the product of the translation across the layer thickness, Δz, and the refraction occurring at the surface of the IIS.

$$\begin{aligned} \mathbf{L}_k(z_k) &= \begin{bmatrix} 1 & -\Delta z \\ 0 & 1 \end{bmatrix} \begin{bmatrix} 1 & 0 \\ \dfrac{\Delta n}{(n+\Delta n/2)R_k} & \dfrac{n-\Delta n/2}{n+\Delta n/2} \end{bmatrix} = \\ &= \begin{bmatrix} 1 & -\dfrac{(n-\Delta n/2)\Delta z}{n+\Delta n/2} \\ \dfrac{\Delta n}{(n+\Delta n/2)R_k} & \dfrac{n-\Delta n/2}{n+\Delta n/2} \end{bmatrix}, \end{aligned} \tag{3.1}$$

where Δz is the shell thickness, which is assumed to be constant in both the discrete and continuous cases, while Δn represents the refractive index difference between the left and right sides of the IIS. Note that n is the refractive index value precisely at the IIS (refracting surface). When $\Delta z \to 0$, the refractive index inside each shell becomes a linear function of z, so when evaluating the refractive index values on either side of the IIS, we can use the mean value of $n(z)$ within those shells. Based on this approach, $n + \Delta n/2$ is the refractive index to the right side of the refracting surface, and $n - \Delta n/2$ is the refractive index to the left.

In the differential limit, by the definition of a derivative, Δn can be expressed as $n'\Delta z$, where n' is the derivative of the refractive index relative to z (dn/dz). We assume that n' is also a function of z in the paraxial region, $n' = n'(z)$. The apical radius of curvature of the IIS refracting surface is denoted as $R_k = R(z_k)$. Let us approximate the four elements of L_k in the limit where $\Delta z \to 0$.

$$L_{k(11)} : 1 - \frac{\Delta z \Delta n}{(n+\Delta n/2)R_k} = 1 - \frac{n'\Delta z^2}{(n+\Delta n/2)R_k} \simeq 1 + \mathcal{O}(\Delta z)^2 \tag{3.2a}$$

$$\begin{aligned} L_{k(12)} : &- \frac{\Delta z(n-\Delta n/2)}{n+\Delta n/2} = -\frac{\Delta z(n-\Delta n/2)^2}{(n+\Delta n/2)(n-\Delta n/2)} = \\ &- \frac{n^2\Delta z - nn'\Delta z^2 + n'^2\Delta z^3/4}{n^2 - n'^2\Delta z^2/4} \simeq -\Delta z + \mathcal{O}(\Delta z)^2 \end{aligned} \tag{3.2b}$$

$$\begin{aligned} L_{k(21)} : &\frac{\Delta n}{(n+\Delta n/2)R_k} = \frac{\Delta n(n-\Delta n/2)}{(n+\Delta n/2)(n-\Delta n/2)R_k} = \\ &\frac{nn'\Delta z - n'^2\Delta z^2/2}{(n^2 - n'^2\Delta z^2/4)R_k} \simeq \frac{n'\Delta z}{nR_k} + \mathcal{O}(\Delta z)^2 \end{aligned} \tag{3.2c}$$

$$L_{k(22)} : \frac{n-\Delta n/2}{n+\Delta n/2} = \frac{(n-\Delta n/2)^2}{(n+\Delta n/2)(n-\Delta n/2)} = \tag{3.2d}$$

$$\frac{n^2 - nn'\Delta z + n'^2\Delta z^2/4}{n^2 - n'^2\Delta z^2/4} \simeq 1 - \frac{n'\Delta z}{n} + \mathcal{O}(\Delta z)^2$$

The residue $\mathcal{O}(\Delta z)^2$ in both eqs. (3.1) and (3.2) includes terms of Δz raised to the second power or higher. As the displacement approaches zero ($\Delta z \to 0$), the residue also tends to zero ($\mathcal{O}(\Delta z)^2 \to 0$), making this term negligible in a first-order approximation. The resulting matrix is the sum of the identity matrix $\mathbb{I}$, a new matrix A that multiplies Δz, and the residue:

$$L_k(z_k) = \begin{bmatrix} 1 & -\Delta z \\ \dfrac{n'}{nR_k}\Delta z & 1 - \dfrac{n'}{n}\Delta z \end{bmatrix} + \mathcal{O}(\Delta z)^2 = \mathbb{I} + A \cdot \Delta z + \mathcal{O}(\Delta z)^2, \tag{3.3}$$

where matrix A is independent of Δz:

$$A = \begin{bmatrix} 0 & -1 \\ \dfrac{n'(z)}{n(z)R(z)} & -\dfrac{n'(z)}{n(z)} \end{bmatrix} \tag{3.4}$$

To compute the ray transfer matrix of the complete GRIN lens, we multiply all the K layers in reverse order of ray propagation. For simplicity, $A_k = A(z_k)$ is the matrix A corresponding to the IIS crossing the optical axis at z_k:

$$\begin{aligned} M &= \prod_{k=1}^{K} L(z_k) = \prod_{k=1}^{K} \left(\mathbb{I} + A_k\Delta z + \mathcal{O}(\Delta z)^2\right) = \\ &= \left(\mathbb{I} + (A_1 + A_2)\Delta z + A_1A_2\Delta z^2 + (A_1 + A_2)\mathcal{O}(\Delta z)^2 + \mathcal{O}(\Delta z)^2\right) \cdot \\ &\quad \cdot \prod_{k=3}^{K} \left(\mathbb{I} + A(z_k)\Delta z + \mathcal{O}(\Delta z)^2\right) \end{aligned} \tag{3.5}$$

$$M \simeq \mathbb{I} + \sum_{k=1}^{K} A(z_k)\Delta z + \mathcal{O}(\Delta z)^2 \tag{3.6}$$

The matrix product can be approximated to a matrix sum by neglecting higher-order powers of Δz. As shown above in eq. (3.5), these appear in cross terms $A_iA_k\Delta z^2$ and any multiplication by $\mathcal{O}(\Delta z)^2$. After this approximation, only the identity matrix $\mathbb{I}$ and the sum of single terms $A_k\Delta z$ remain.

3.2.2 The Continuous Case

To formulate GRIN lenses in the continuous limit, we replace Δz with dz and the sum in eq. (3.6) with an integral:

$$\begin{aligned} M \simeq \mathbb{I} + \int_0^t A(z)dz &= \begin{bmatrix} 1 & -\int_0^t dz \\ \int_0^t \dfrac{n'(z)}{n(z)R(z)}dz & 1 - \int_0^t \dfrac{n'(z)}{n(z)}dz \end{bmatrix} \\ &= \begin{bmatrix} 1 & -t \\ \int_0^t \dfrac{n'(z)}{n(z)R(z)}dz & 1 + \log\left(\dfrac{n(0)}{n(t)}\right) \end{bmatrix} \end{aligned} \tag{3.7}$$

The anterior vertex of the lens is at $z = 0$, and t represents the lens thickness. The ray transfer matrix M for the entire GRIN distribution can be obtained by integrating the elements of the differential matrix $L_k(z_k)$ (eq. (3.3)).

Now, let us examine the scenario of a meniscus lens. In the absence of a curvature gradient, $R(z) = R_s$, with R_s being the apical curvature radius of the external surfaces, the iso-indicial surfaces are parallel. In this situation, the integral defined in element M_{21} has a straightforward solution:

$$\int_0^t \frac{n'(z)}{n(z)R_s}dz = \frac{1}{R_s}\int_0^t \frac{n'(z)}{n(z)}dz = \frac{1}{R_s}\log\left(n(z)\right)\Big|_0^t = \frac{1}{R_s}\log\left(\frac{n(t)}{n(0)}\right) \tag{3.8}$$

Since the refractive indices at the anterior and posterior surfaces are identical, $n(0) = n(t)$, the integral is zero, leading to $M_{21} = 0$ and $M_{22} = 1$. In this case, M represents a pure translation, and the GRIN media does not contribute to the lens power.

In the case of a biconvex lens, we can picture it as a cemented doublet featuring a positive radius R_{as} for the anterior side and a negative radius R_{ps} for the posterior side. Let t_a and t_p represent the thicknesses of the anterior and posterior regions, respectively, with the total thickness being $t = t_a + t_p$. The integral in element M_{21} can then be expressed as the sum of these two sections, resulting in:

$$M_{21} = \frac{1}{R_{as}}\log\left(\frac{n(t_a)}{n(0)}\right) + \frac{1}{R_{ps}}\log\left(\frac{n(t)}{n(t_a)}\right) \tag{3.9}$$

Given that the refractive index at the surface is $n_s = n(0) = n(t)$, and at the center of the lens is $n_c = n(t_a)$, it follows that:

$$M_{21} = \frac{1}{R_{as}}\log\left(\frac{n_c}{n_s}\right) + \frac{1}{R_{ps}}\log\left(\frac{n_s}{n_c}\right) = \left(\frac{1}{R_{as}} - \frac{1}{R_{ps}}\right)\log\left(\frac{n_c}{n_s}\right) \tag{3.10}$$

This expression is analogous to the power of a thin lens in air, with the refractive indices replaced by their logarithms. Note that when the refractive index is identical at the anterior and posterior surfaces $n(0) = n(t)$, element M_{22} equals one for any type of lens.

3.2.3 Lens Surface Contribution

Matrix M corresponds to the ray propagation inside the lens, where the gradient refractive index $n(z)$ is continuous and has a derivative $n'(z)$. Because of the abrupt change in refractive index at the surfaces, we can formulate the refraction at the anterior and posterior surfaces separately. The lens matrix can now be expressed as the product of three matrices: S_p, refraction at the anterior surface; M, ray propagation in the GRIN media; and S_a, refraction at the anterior surface.

$$L = S_p M S_a, \text{ with} \tag{3.11}$$

$$S_a = \begin{bmatrix} 1 & 0 \\ \dfrac{n_a - n_{0a}}{n_a R_{as}} & \dfrac{n_{0a}}{n_a} \end{bmatrix} \text{ and } S_p = \begin{bmatrix} 1 & 0 \\ \dfrac{n_{0p} - n_p}{n_{0p} R_{ps}} & \dfrac{n_p}{n_{0p}} \end{bmatrix} \tag{3.12}$$

Here, n_a and n_p represent the refractive indices of the anterior and posterior lens surfaces, respectively, while n_{0a} and n_{0p} denote the refractive indices of the surrounding media of the anterior and posterior surfaces. For simplicity, we assume the lens is immersed in a medium such that $n_{0a} = n_{0p} = n_0$, and the entire lens surface has a uniform refractive index $n_s = n_a = n_p$. Consequently, the matrix product for a ray propagating across the whole lens is given by:

$$L = \begin{bmatrix} 1 - t\dfrac{n_s - n_0}{n_s R_{as}} & -t\dfrac{n_0}{n_s} \\ \left[\dfrac{n_s - n_0}{n_0}\left(\dfrac{1}{R_{as}} - \dfrac{1}{R_{ps}}\right)\right] + \left[\dfrac{(n_0 - n_s)^2}{n_0 n_s R_{as} R_{ps}}t\right] + \dfrac{n_s}{n_0}\int_0^t \dfrac{n'(z)}{n(z)R(z)}dz & 1 - t\dfrac{n_0 - n_s}{n_s R_{ps}} \end{bmatrix} \tag{3.13}$$

The main theoretical result of this work is the ray transfer matrix of a biconvex GRIN lens comprised of infinitesimal shells or layers–each characterized by its refractive index and curvature radius–.

3.2.4 Lens Power

The most significant element in this matrix is L_{21}, which represents the inverse of the focal length and thus determines the lens power. The first term of L_{21} reflects the power of a standard thin lens with a refractive index equal to the surface index value n_s. The second term pertains to the power of a thick lens. The third term, which includes the integral, accounts for the contribution of the GRIN inner structure to the lens power. This follows a straightforward additive principle. The other elements of matrix L are analogous to those of a homogeneous lens, denoted as $H = S_p \mathcal{T} S_a$, where the GRIN matrix, M (eq. (3.7)), is replaced by a translation matrix, $\mathcal{T}$, for the propagation of a ray through homogeneous media of refractive index n_s. To transform the ray transfer matrix of a homogeneous lens H into a GRIN lens matrix L, we need to add the GRIN structure's contribution (the integral term) to H_{21}.

$$L_{21} = H_{21} + \frac{n_s}{n_0}\int_0^t \frac{n'(z)}{n(z)R(z)}dz = H_{21} + \frac{\phi_G}{n_0}, \tag{3.14}$$

where ϕ_G is the GRIN contribution to the lens power. Or in matrix form:

$$\begin{aligned} L = &\begin{bmatrix} 1 - t\dfrac{n_s - n_0}{n_s R_{as}} & -t\dfrac{n_0}{n_s} \\ \left[\dfrac{n_s - n_0}{n_0}\left(\dfrac{1}{R_{as}} - \dfrac{1}{R_{ps}}\right)\right] + \left[\dfrac{(n_0 - n_s)^2}{n_0 n_s R_{as} R_{ps}}t\right] & 1 - t\dfrac{n_0 - n_s}{n_s R_{ps}} \end{bmatrix} + \begin{bmatrix} 0 & 0 \\ \dfrac{n_s}{n_0}\displaystyle\int_0^t \frac{n'(z)}{n(z)R(z)}dz & 0 \end{bmatrix} \\ = &H + \begin{bmatrix} 0 & 0 \\ \dfrac{n_s}{n_0}\displaystyle\int_0^t \frac{n'(z)}{n(z)R(z)}dz & 0 \end{bmatrix} = H + \begin{bmatrix} 0 & 0 \\ \dfrac{\phi_G}{n_0} & 0 \end{bmatrix} = H + \mathcal{G} \end{aligned} \tag{3.15}$$

Where $\mathcal{G}$ is a single-element matrix containing the contribution of the GRIN inner structure to the lens power. To compute this power, element L_{21} is

multiplied by the external refractive index, here denoted as n_0. The theoretical result presented in eq. (3.13) is particularly noteworthy because it offers a straightforward and intuitive approach. When the refractive index $n(z)$ is continuous and differentiable, and its derivative $n'(z)$ exists within the interval, the integral can be numerically solved using the trapezoidal rule, for example. As detailed below in Section 3.3.3, the integral can be resolved analytically or approximated with a high degree of accuracy in certain instances.

3.3 APPLICATION TO THE CRYSTALLINE LENS

The human lens is a classic example of an onion-type GRIN distribution. Most experimental studies [19, 21, 79, 80] and theoretical models [59, 66, 70, 78] indicate that the axial distribution in the anterior and posterior segments adheres to a power law. Our GRINCU lens model, presented in Chapter 2, describes these anterior and posterior refractive index distributions using Equation (13) from Ref. [3] in terms of the parameter $z_0 = z_0(\omega, \theta, z)$, which characterizes the iso-indicial surfaces for any given refractive index value n. In the paraxial region, it is assumed that the index distribution is solely a function of z, thus $z_0 = z_0(0, 0, z)$. The refractive index distribution is described by eq. (2.17):

$$n(0,0,z_0) = \begin{cases} n_a(z_0) = n_c - \delta_n \left(1 - \dfrac{z_0}{t_a}\right)^p & \text{for } z \leqslant z_{0a} \leqslant t_a \\ n_p(z_0) = n_c - \delta_n \left(\dfrac{z_0 - t_a}{t_p}\right)^p & \text{for } t_a < z_{0p} \leqslant t \end{cases}$$

The GRINCU lens is distinguished by having a gradient parameter $g = G(Q+1)$ for the curvature radius, in addition to the gradient refractive index. In this application example we adopt the most straightforward mathematical approach by using a constant G value ($G = G_a = G_p$). Consequently, based on eqs. (2.8a) and (2.8b), the apical radii of curvature of the iso-indicial surfaces for the anterior and posterior regions of the lens are, respectively:

$$R_a(z_0) = R_{as} - G(Q_a + 1)z_0 = R_{as} - g_a z_0 \tag{3.16a}$$

$$R_p(z_0) = R_{ps} - G(Q_p + 1)(z_0 - t) = R_{ps} - g_p(z_0 - t) \tag{3.16b}$$

Here, Q_a and Q_p are the conic constants of the external surfaces, which remain constant throughout all iso-indicial surfaces. Therefore, the curvature radius gradients, $-g_a$ and $-g_p$, are constant inside the anterior and posterior parts of the lens. For spheres ($Q = 0$), the gradient is $-G$.

3.3.1 Numerical Implementation

In eqs. (2.17), (3.16a) and (3.16b), $n(z)$ and $R(z)$ are explicitly defined as functions of z; and $n'(z) = dn/dz$ can be straightforwardly derived from eq. (2.17). These three functions make up the integral in element L_{21} (eq. (3.14)), which is proportional to the GRIN contribution to the total lens power as a function of z. To calculate this power, we multiply the integral by the refractive index of the surrounding medium, n_0, and evaluate the integral, splitting it into anterior and posterior sections:

$$\phi_G = -\frac{n_s p \delta n}{t_a} \int_0^{t_a} \frac{(1 - z/t_a)^{p-1}\, dz}{[n_c + \delta n\,(1 - z/t_a)^p]\,(R_{as} - g_a z)} + \frac{n_s p \delta n}{t_p} \int_{t_a}^{t} \frac{((z - t_a)/t_p)^{p-1}\, dz}{[n_c + \delta n\,((z - t_a)/t_p)^p]\,(R_{ps} - g_p(z - t))} \tag{3.17}$$

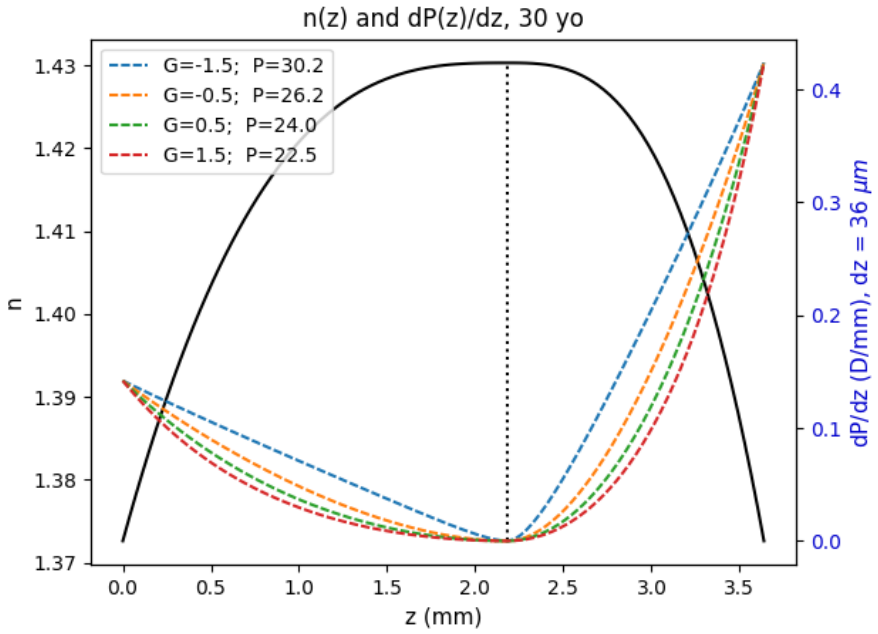

Figure 3.1: The convex-up solid line shows the variation of n along z in the paraxial region. The concave-up dashed lines represent $dP(z)/dz$ for different G values. The total lens power for each G is displayed in the legend.

Note that the integral is dimensionless, and ϕ_G is given in diopters when the thicknesses are given in meters. Figure 3.1 illustrates the axial distribution of the refractive index $n(z)$ and the contribution of each layer to the overall lens power represented as the approximate differential $dP(z)/dz$, for various values of the gradient parameter G. In this example, which uses a 30-year-old GRINCU lens model, a finite layer thickness of $dz = 36$ mum (corresponding to $t/100$ and resulting in 100 layers) was applied. Since the integration of $dP(z)$ generally lacks an analytical solution, numerical integration was performed using the trapezoidal rule. The resulting total lens powers for this example are provided in the legend. The convergence achieved with the trapezoidal rule is demonstrated in fig. 3.2 and is further discussed in Section 3.4.1.

3.3.2 Exact Integration

In the absence of a curvature gradient, when $G = 0$ or $Q = -1$, the iso-indicial surfaces are parallel in both the anterior and posterior sections of the lens. Under these conditions, eq. (3.17) has a precise analytical solution: R_{as} and

R_{ps} can be extracted from the integrals, which then simplify into logarithmic expressions.

$$\phi_G = n_s \left(\frac{1}{R_{as}} - \frac{1}{R_{ps}} \right) \log \left(\frac{n_c}{n_s} \right) \tag{3.18}$$

This expression is similar to that of a thin biconvex lens, except that the difference in refractive indices is replaced by the difference in their respective logarithms, each multiplied by the surface index.

3.3.3 Analytical Solution

The GRIN contribution to the refractive power is found by solving the integral in element M_{21} in matrix M (eq. (3.7)). The integrals for the anterior and posterior regions, F_a and F_p, respectively, are calculated separately eq. (3.17) to obtain $\phi_G = F_a + F_p$. In the case of the GRINCU lens model, the integrals are computed along the optical z axis, where $\omega = 0$, $z_{0a} = z$, and $z_{0p} = z$.

$$F_a = -\frac{n_s p \delta n}{t_a} \int_0^{t_a} \frac{(1 - z/t_a)^{p-1}\, dz}{[n_c + \delta n\,(1 - z/t_a)^p]\,(R_{as} - g_a z)} \tag{3.19a}$$

$$F_p = \frac{n_s p \delta n}{t_p} \int_{t_a}^{t} \frac{((z - t_a)/t_p)^{p-1}\, dz}{[n_c + \delta n\,((z - t_a)/t_p)^p]\,(R_{ps} - g_p (z - t))} \tag{3.19b}$$

These integrals cannot be solved in terms of known functions, but we worked out a highly accurate approximated solution. First, we apply a change of variable $x = (1 - z/t_a)^p$ to F_a, and $x = ((z - t_a)/t_p)^p$ to F_p.

$$F_a = -n_s \delta n \int_0^1 \frac{dx}{(n_c + x\delta n)\left(R_{as} - g_a t_a (1 - x^{1/p})\right)} \tag{3.20a}$$

$$F_p = \; n_s \delta n \int_0^1 \frac{dx}{(n_c + x\delta n)\left(R_{ps} + g_p t_p (1 - x^{1/p})\right)} \tag{3.20b}$$

The fraction $1/(n_c + x\delta n)$ can be written as an m-order series expansion:

$$\frac{1}{n_c + x\delta n} = \frac{1}{n_c} \sum_{k=0}^{m-1} \left(-\frac{\delta n}{n_c} x \right)^k + \frac{(-x\delta n/n_c)^m}{n_c + x\delta n}\,; \quad m = 1, 2, 3... \tag{3.21}$$

Substituting this factor in eqs. (3.20a) and (3.20b) and reversing the order of the sum and the integral returns:

$$F_a := -\frac{n_s \delta n}{n_c} \sum_{k=0}^{m-1} \left(-\frac{\delta n}{n_c} \right)^k \int_0^1 \frac{x^k dx}{\left(R_{as} - g_a t_a (1 - x^{1/p})\right)} + \mathcal{O}_a(m) \tag{3.22}$$

$$= n_s \sum_{k=0}^{m-1} \frac{(-\delta n/n_c)^{k+1}}{(k+1)(R_{as} - g_a t_a)}\, {}_2F_1 \left(\begin{matrix} 1, (k+1)p \\ (k+1)p + 1 \end{matrix} \middle| \frac{-g_a t_a}{R_{as} - g_a t_a} \right) + \mathcal{O}_a(m) \tag{3.23}$$

$$F_p := \frac{n_s \delta n}{n_c} \sum_{k=0}^{m-1} \left(-\frac{\delta n}{n_c}\right)^k \int_0^1 \frac{x^k dx}{\left(R_{ps} + g_p t_p (1 - x^{1/p})\right)} + \mathcal{O}_p(m) \tag{3.24}$$

$$= - n_s \sum_{k=0}^{m-1} \frac{(-\delta n/n_c)^{k+1}}{(k+1)(R_{ps} + g_p t_p)} \, {}_2F_1 \left(\begin{matrix} 1, (k+1)p \\ (k+1)p + 1 \end{matrix} \middle| \frac{g_p t_p}{R_{ps} + g_p t_p} \right) + \mathcal{O}_p(m) \tag{3.25}$$

Where ${}_2F_1 \left(\begin{matrix} a, b \\ c \end{matrix} \middle| z \right)$ is the Gaussian hypergeometric function [91], and $\mathcal{O}_a(m)$ and $\mathcal{O}_p(m)$ are residues of order m and higher that result from replacing the independent term of eq. (3.21) in eqs. (3.20a) and (3.20b).

$$\mathcal{O}_a(m) := n_s \delta n \left(-\frac{\delta n}{n_c}\right)^m \int_0^1 \frac{-x^m dx}{\left(R_{as} - g_a t_a (1 - x^{1/p})\right)(n_c + x\delta n)} \tag{3.26}$$

$$\mathcal{O}_p(m) := n_s \delta n \left(-\frac{\delta n}{n_c}\right)^m \int_0^1 \frac{x^m dx}{\left(R_{ps} + g_p t_p (1 - x^{1/p})\right)(n_c + x\delta n)} \tag{3.27}$$

Given that $1/(n_c + x\delta n) \leqslant 1/(n_c + \delta n)$ for $\delta n < 0$ within the interval $0 \leqslant x \leqslant 1$, it can be replaced with the constant $1/(n_c + \delta n)$ and factored out of the integral. Consequently, the absolute values of $\mathcal{O}_{m(a)}$ and $\mathcal{O}_{m(p)}$ are constrained, and we can apply the same modification as shown in eqs. (3.22) and (3.24).

$$|\mathcal{O}_a(m)| \leqslant n_s \left(-\frac{\delta n}{n_c}\right)^m \frac{-\delta n/(n_c + \delta n)}{(m+1)(R_{as} - g_a t_a)} \, {}_2F_1 \left(\begin{matrix} 1, (m+1)p \\ (m+1)p + 1 \end{matrix} \middle| \frac{-g_a t_a}{R_{as} - g_a t_a} \right) \tag{3.28}$$

$$|\mathcal{O}_p(m)| \leqslant n_s \left(-\frac{\delta n}{n_c}\right)^m \frac{-\delta n/(n_c + \delta n)}{(m+1)(R_{ps} + g_p t_p)} \, {}_2F_1 \left(\begin{matrix} 1, (m+1)p \\ (m+1)p + 1 \end{matrix} \middle| \frac{g_p t_p}{R_{ps} + g_p t_p} \right) \tag{3.29}$$

By disregarding the residual terms in equations eqs. (3.23) and (3.25), we can derive an analytical approximation for F_a and F_p by selecting an expansion order m. For a first-order approximation, we set $m = 1$, for a second-order approximation, $m = 2$, and so forth. We evaluated the first and second-order approximations ($m = 1$ and $m = 2$) against our numerical approximation. The first-order approximation ($m = 1$) showed a $1 - 2\%$ deviation in calculated lens power, whereas the second-order approximation ($m = 2$) demonstrated almost exact agreement, with a discrepancy of only 0.08%. Consequently, we adopted the second-order expressions for the GRIN contribution to the lens refractive power in element L_{21} (eq. (3.14)) of the analytical ray transfer matrix of our GRINCU lens model:

$$F_a \simeq - \frac{n_s \delta n/n_c}{R_{as} - g_a t_a} \, {}_2F_1 \left(\begin{matrix} 1, p \\ p + 1 \end{matrix} \middle| \frac{-g_a t_a}{R_{as} - g_a t_a} \right) + \frac{n_s (-\delta n/n_c)^2}{2(R_{as} - g_a t_a)} \, {}_2F_1 \left(\begin{matrix} 1, 2p \\ 2p + 1 \end{matrix} \middle| \frac{-g_a t_a}{R_{as} - g_a t_a} \right) \tag{3.30}$$

$$F_p \simeq \frac{n_s \delta n / n_c}{R_{ps} + g_p t_p} {}_2F_1\left(\begin{matrix}1, p \\ p+1\end{matrix}\middle| \frac{G(Q_p+1)t_p}{R_{ps}+g_p t_p}\right) - \frac{n_s(-\delta n/n_c)^2}{2(R_{ps}+g_p t_p)} {}_2F_1\left(\begin{matrix}1, 2p \\ 2p+1\end{matrix}\middle| \frac{G(Q_p+1)t_p}{R_{ps}+g_p t_p}\right) \tag{3.31}$$

Here, ${}_2F_1$ is the Gaussian hypergeometric function [91], which is built-in in both commercial and non-commercial computing environments –(specifically MATLAB and Python)—-. These expressions were tested against the numerical results, obtaining a close agreement, as discussed in Section 3.4.

3.4 RESULTS

All results in this section were obtained using the refractive index values listed in table 2.1, and a lens age of 30 years.

3.4.1 Discrete vs. Continuous Convergence

To evaluate the precision of the calculated power as described in eq. (3.17), we compared the numerical implementation of our method with the original direct matrix product approach, focusing on convergence. In our approach, we utilized $L_k(z_k)$ in eq. (3.1) for our matrix product, with $k = 1, 2, \ldots, N$, which are not normalized (contrary to Giovanzana *et al.* [89], who employed a normalized version of these matrices). Figure 3.2 presents the compared results of both methods. The horizontal axis indicates N, the number of integration steps or matrices (shells) used to compute the power. The vertical axis shows the total lens power as a function of the number of steps. The dashed blue line represents the numerical integration method, while the solid red line corresponds to the matrix product. Both methods yield nearly identical results, differing by only 0.04 D (0.13% difference).

Figure 3.3 summarizes the results of different refractive power matrix computation methods compared with the thin lens approximation (dotted red line) used by several authors before [3, 39, 70]. The thin lens approximation involves a more straightforward formulation and does not require matrix formalism. However, it yields a systematic overestimation of lens power by more than 0.3 D. The methods proposed in this work are labeled as analytical (continuous black lines), numerical (dashed green lines), and exact (red asterisk) for $G = 0$. The agreement between them is almost perfect. The matrix product (dashed blue line) yields slightly higher power than the numerical integration for more negative values of G, with a maximum difference of 0.54% for $G = -1.5$ and a minimum difference of 0.001% for near-zero Q_a values. The slab method, however (dash-dotted magenta line), has the opposite effect, yielding slightly less power than our analytical method. Section 3.4.3 below elaborates on how the slab method compares against our matrix product and numerical integration approaches.

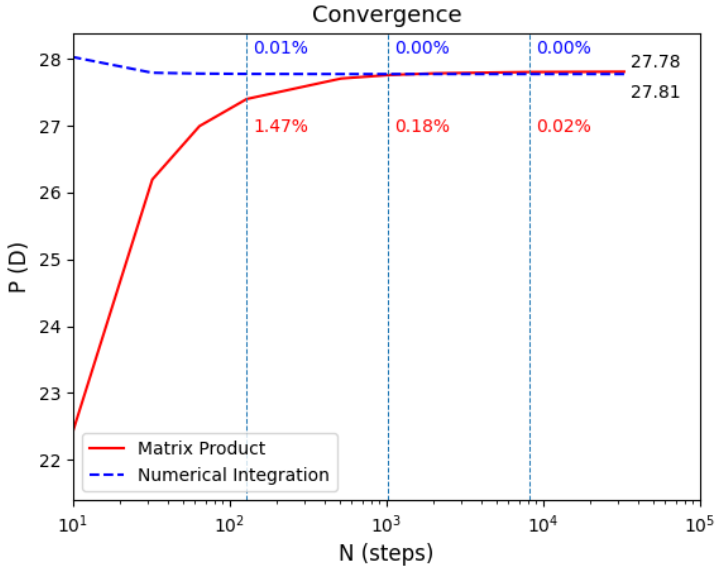

Figure 3.2: Computed power of the lens model versus the number of steps for two methods: matrix product and numerical integration. The percent difference with the last point ($N = 33,000$) is shown for three values of N.

3.4.2 Effect of G and Q on the Lens Refractive Power

The mathematical ray transfer matrix formulation described here is used to analyze how changes in the radius of curvature gradient, g, affect the refractive power of the lens. This net curvature gradient depends on a parameter, G, and on the conic constant of the external surface of the lens, Q ($g = G(Q+1)$). Both variables showed similar non-linear relationships with the power, albeit with opposite trends. Increasing G while maintaining fixed Q_a and Q_p values decreased power (fig. 3.3a).

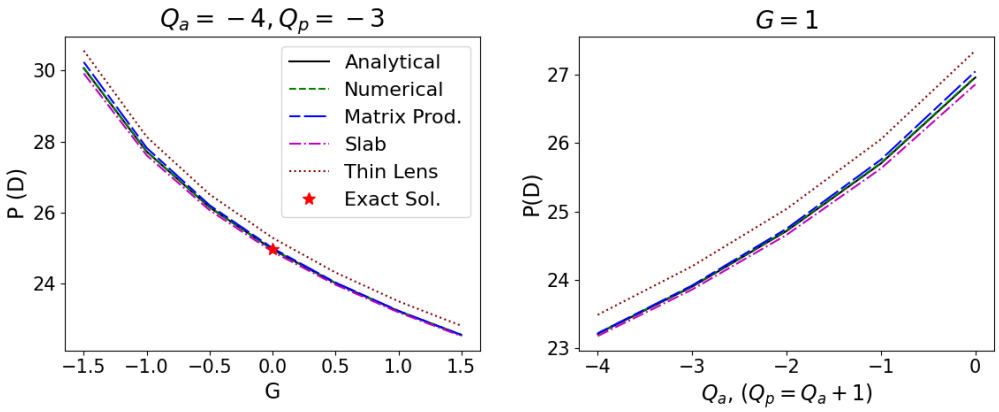

(a) Power dependence on G.

(b) Power dependence on Q_a.

Figure 3.3: Comparison of various methods for computing lens power and its dependence on G and Q_a, Q_p.

Oppositely, increasing Q_a and Q_p while keeping G fixed increased power (fig. 3.3b). This means that ellipsoid surfaces ($Q > 0$) deliver more power than

hyperbolic surfaces ($Q < 0$). Previous literature has reported a reduction in GRIN lens power with increasingly negative Q values [66], which would align with our findings. Still, the authors found the result non-intuitive because the paraxial power is unaffected by conic constants in homogeneous lenses. This new formulation provides a simple and direct explanation for this effect, as the curvature radius gradient is directly proportional to $(Q + 1)$. However, further study is needed to fully understand the relationship between the conic constant and the paraxial lens power.

3.4.3 Comparison with Slab Method

For comparison purposes, we also implemented the ABCD matrix slab method (denoted by dash-dotted magenta lines in fig. 3.3) using Díaz's [87] parabolic approximation formulation. This method slightly underestimates power compared with the matrix product and the differential shell method proposed here. The line is not generally parallel to the thin lens approximation (refer to fig. 3.3). A closer match is observed for more negative Q values and higher G values (with a minimum difference of 0.17% in both cases). Conversely, the most significant discrepancy of 0.53% occurs at non-negative Q values (see fig. 3.3b). Despite this, the differences are consistently within 0.16 D. The agreement between the slab and the shell methods is reasonable, particularly for the typically negative conic constant values used in lens models.

Using $G = 1$ and $Q_a = -4$, $Q_p = -3$, we obtained the following GRIN lens matrices for the matrix product, L_m, our numerical integration, L_n, and the slab method, L_s:

$$L_m = \begin{bmatrix} 0.9793 & -3.4258 \\ 0.0174 & 0.9603 \end{bmatrix}; L_n = \begin{bmatrix} 0.9915 & -3.5447 \\ 0.0174 & 0.9831 \end{bmatrix}; L_s = \begin{bmatrix} 0.9787 & -3.4514 \\ 0.0171 & 0.9616 \end{bmatrix} \tag{3.32}$$

Matrix element L_{21}, which is proportional to the lens power, shows close agreement across the three methods, but slight differences exist in the other three elements. In our numerical integration, L_n, the diagonal elements are precisely 1, and the element $L_{n(12)} = -t \cdot n_a/n_s$ is directly proportional to the lens thickness (3.6380 mm). In the other two matrices, these elements differ from ours. The matrix product shows the most notable deviation with 3.3% less lens thickness than the numerical integration, while the slab method differs by 2.6%. Matrices L_m and L_s are nominally unitary, meaning their determinants equal one. However, due to the GRIN contribution to the homogeneous lens described by the result in eq. (3.15), the determinant of L_n is slightly greater than one. We conclude that all the ray transfer matrices compared here show reasonable agreement.

3.4.4 Validation with other GRIN Models

As previously noted, this matrix formulation's theoretical and numerical implementation can be broadly applied to various GRIN lenses, not just the human lens, given that:

a) the corresponding iso-indicial surfaces exhibit a shell-like distribution, meaning the contours form a shell structure around the axis,

b) we know the refractive index distribution along the optical axis, and

c) we can calculate the apical curvature radius of the iso-indicial surfaces using standard differential geometry techniques.

To illustrate the versatility of our approach, we applied it to the AVOCADO crystalline lens model [70], known as one of the most sophisticated in the field. A key reason for selecting this model is that the authors provide precise results for lens power calculations and compare ray tracing with the thin lens formula in Figure 3 of their publication [70]. Using our method, we reproduced their results, as depicted below in fig. 3.4. By comparing our plots and values with theirs, we can conclude that our model successfully replicated both the thin lens and ray tracing lens powers with remarkable accuracy.

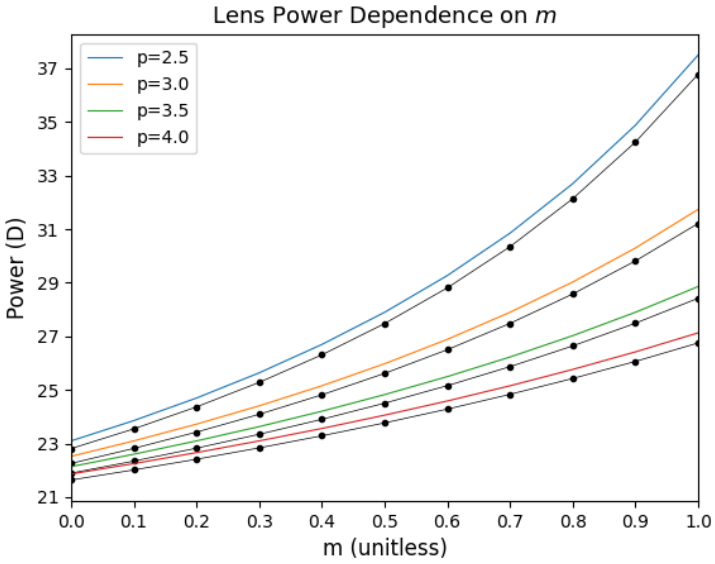

Figure 3.4: Lens power vs. coefficient m for different values of p. The solid lines are calculated with the thin lens approximation of the integral, and the dotted lines correspond to the numerical integration.

4 FINITE RAY TRACING

4.1 RAY TRACING SOFTWARE FOR GRIN LENS MODELS

Commercially available ray tracing software, such as Zemax, does not provide the ability to directly customize gradient index surfaces as described in Chapter 2. However, it is possible to create user-defined surfaces that can be integrated into the program [92]. In order to perform finite ray tracing on our model, we developed new user-defined surfaces for the GRINCU lens: one for singlet and another for doublet configurations. The main reason for implementing these two versions of the model is that, although the model is continuous, it can exhibit discontinuities in the gradient at the central interface, which could potentially bias the ray tracing. The doublet version mitigates this issue and allows us to cross-check and validate both versions. For verification purposes, these were implemented in two platforms. For Zemax, the surfaces were programmed in C++ and compiled into a .dll file for subsequent loading into Zemax OpticStudio [93]. The same singlet and doublet GRINCU lens surfaces were implemented in RTLib, a custom Matlab ray tracing library developed by Fernando Palos [2, 94].

To ensure the accuracy and validity of these implementations, we initially conducted a paraxial analysis for both the singlet and doublet lenses. Further tests were performed on aberrations to cross-validate the results between RTLib and Zemax.

4.2 GRINCU SURFACE IMPLEMENTATION

The general structure and content of user-defined surfaces are thoroughly outlined in Zemax's knowledge base [92]. The program is organized into several switch cases, each corresponding to different types of data Zemax requests during ray tracing. In this discussion, we will focus only on the sections of the program customized for the GRINCU lens. The same program structure is also utilized in RTLib, making the following descriptions applicable to both languages.

In the case of Zemax, the C++ program needs to be compiled to produce a DLL file, which is subsequently loaded into Zemax OpticStudio. In contrast, RTLib does not require compilation and lacks a user interface for surface editing, as it functions as a Matlab library. Two models were implemented: a singlet, where the internal GRIN distribution is configured in its entirety at once, and a cemented doublet, where the anterior and posterior GRIN regions are configured separately, with the interface dividing them.

4.2.1 Singlet

The code block labeled *case 6* contains the formulation of the lens model (Section 2.2). First, values are assigned for wavelength and age. The wavelength determines the dispersion coefficients for both the lens surface and the core refractive indices, whereas age influences the external radii of curvature, thickness, and gradient index (GRIN) distribution of the lens (see to Table 2.1 for the definitions and equations of the age-dependent parameters). Below is the structure of the MATLAB/C++ code for the singlet configuration.

First, z_0, ω^2, and the normalized variables s_a, s_p are computed at the coordinate (x, y, z):

```
% ANTERIOR REGION %

w2a = Ra * ((x*cos(theta) + y*sin(theta))^2 / (Ra + Da) + (y*cos(theta) -
    x*sin(theta))^2 / (Ra - Da));
% square root in z0 numerator
roota = sqrt((Ra - G * (Qa+1) * z)^2 + (2*G-1) * (Qa+1) * w2a);
if (Qa == -1.0)  % if parabola
    z0a = z - w2a / (2 * Ra);
else
    z0a = (Ra + (G-1) * (Qa+1) * z - roota) / (2*G-1) / (Qa+1);
end
sa = 1 - z0a / ta;

% POSTERIOR REGION %

w2p = Rp * ((x*cos(theta) + y*sin(theta))^2 / (Rp + Dp) + (y*cos(theta) -
    x*sin(theta))^2 / (Rp - Dp));
% square root in z0 numerator
rootp = sqrt((Rp + G * (Qp+1) * (t-z))^2 + (2*G-1) * (Qp+1) * w2p);
if (Qp == -1.0)  % if parabola
    z0p = z - w2p / (2 * Rp);
else
    z0p = (Rp + (G-1) * (Qp+1) * z + G * (Qp+1) * t + rootp) / (2*G-1) / (
        Qp+1);
end
sp = (z0p - ta) / t;
```

Depending on whether the coordinate (z_0, ω^2) is in the anterior or the posterior region of the lens, the refractive index and its partial derivatives are calculated either with s_a or s_p.

```
if (sa > sp)  % anterior region
    n = nc + dn * sa^p;                     % refractive index
    dndz0 = - dn * p * sa^(p - 1) / ta;     % refractive index derivative
    if (Qa == -1.0)  % if parabola
        dz0dz = 1;
        dz0dw2 = - 0.5 / Ra;
    else
        dz0dz = (G-1) / (2*G-1) + G * (Ra - G*(Qa+1) * z)  / (2*G-1) /
            roota;
```

```
        dz0dw2 = 1 / (2 * roota);
    end
    % partial derivatives
    dw2dx = 2*Ra * (cos(theta) * (x*cos(theta) + y*sin(theta)) / (Ra + Da)
         - sin(theta) * (-x*sin(theta) + y*cos(theta)) / (Ra -Da));
    dw2dy = 2*Ra * (sin(theta) * (x*cos(theta) + y*sin(theta)) / (Ra + Da)
         + cos(theta) * (-x*sin(theta) + y*cos(theta)) / (Ra -Da));
    % chain rule
    dndx = dndz0 * dz0dw2 * dw2dx;
    dndy = dndz0 * dz0dw2 * dw2dy;
    dndz = dndz0 * dz0dz;
    % pass the values of the derivatives to the ray tracing program
    obj.UD.dnds = [dndx, dndy, dndz];
else  % posterior region
    n = nc + dn * sp^p;                     % refractive index
    dndz0 = dn * p * sp^(p - 1) / tp;       % refractive index derivative
    if (Qp == -1.0)  % if parabola
        dz0dz = 1;
        dz0dw2 = - 0.5 / Rp;
    else
        dz0dz = (G-1) / (2*G-1) - G * (Rp + G * (Qp+1) * (t-z)) / (2*G-1)
            / rootp;
        dz0dw2 = 1 / (2 * rootp);
    end
    % partial derivatives
    dw2dx = 2 * Rp * (cos(theta) * (x*cos(theta) + y*sin(theta)) / (Rp +
        Dp) + sin(theta) * (x*sin(theta) - y*cos(theta)) / (Rp -Dp));
    dw2dy = 2 * Rp * (sin(theta) * (x*cos(theta) + y*sin(theta)) / (Rp +
        Dp) - cos(theta) * (x*sin(theta) - y*cos(theta)) / (Rp - Dp));
    % chain rule
    dndx = dndz0 * dz0dw2 * dw2dx;
    dndy = dndz0 * dz0dw2 * dw2dy;
    dndz = dndz0 * dz0dz;
    % pass the values of the derivatives to the ray tracing program
    obj.UD.dnds = [dndx, dndy, dndz];
end

% pass the refractive index value to the ray tracing program
obj.UD.index = n;
```

4.2.2 Doublet

In the doublet configuration, the interface is computed numerically by finding the points where `sa = sp` and then fitting this grid of points to a conic surface using Taubin's method (see Appendix B). From this fitting, we can determine the interface's apical radius of curvature, R_i, and conic constant, Q_i with the canonical transformation described in Appendix C. The anterior and posterior regions are then modeled in the ray tracing program as two successive surfaces, with the interface serving as the anterior boundary of the posterior region.

4.3 RAY TRACING WITH RTLIB

In RTLib, there is no graphical user interface as found in Zemax. Instead, the optical system and its components are programmed within an executable Matlab file. The default optical system is based on the Navarro eye model. All surfaces within the system can be modified, including parameters such as surface position, radius of curvature, thickness, and refractive index. Detailed instructions for these modifications can be found in the reference material, so they will not be discussed here. Below is an example of how to integrate a GRINCU lens into the optical system of an eye.

4.3.1 Singlet

The command `sys = opticSystem()` creates a 7-surface system with the following surfaces: (0) object surface, (1) 'dummy' stop, (2) cornea, (3) anterior chamber, (4) lens, (5) posterior chamber, and (6) image surface. Once the optical system is established, the crystalline lens type is set to a GRINCU surface, and the new lens parameters are defined. Below is a general example that can be tailored with any values.

```
%% anterior lens %%

sys.SetSurfaceVal(4,1,'grincu');        % lens type
sys.SetSurfaceVal(4,2,'GRINCU');        % lens label
sys.SetSurfaceVal(4,3,Ra);              % anterior radius of curvature
sys.SetSurfaceVal(4,4,t);               % lens thickness
sys.SetSurfaceVal(4,6,4.5);             % lens semidiameter
sys.SetSurfaceVal(4,7,Qa);              % conic constant
sys.SetSurfaceVal(4,9,[LTx,LTy,0]);     % lens tilt
sys.SetSurfaceVal(4,8,[LShx,LShy]);     % lens shift

%% build the internal GRINCU distribution %%
sys.SetSurfaceParam(4,1, [step, p, ta, Rp, Qp, ns, nc, G, tor, theta]);
```

Where `step` represents the step size used to construct the GRIN media within the lens, `p` is the age-dependent power law exponent, `ta` denotes the anterior lens axial thickness, and `Rp` and `Qp` are the posterior radius of curvature and conic constant, respectively. Additionally, `ns` and `nc` indicate the refractive indices at the lens surface and core, while `tor` and `theta` refer to the surface toricity and astigmatism angle.

```
%% posterior lens %%

sys.SetSurfaceVal(5,4,VCD);             % vitreous chamber depth
sys.SetSurfaceVal(5,3,Rp);              % radius of curvature
sys.SetSurfaceVal(5,5,naq);             % aqueous humor
sys.SetSurfaceVal(5,6,4.5);             % lens semidiameter
sys.SetSurfaceVal(5,7,Qp);              % conic constant
sys.SetSurfaceVal(5,9,[LTx,LTy,0]);     % lens tilt
sys.SetSurfaceVal(5,8,[LShx + t * tan(pi + LTy / 180),
```

```
                        LShy + t * tan(pi + LTx / 180)]);
                                            % lens shift
sys.SetSurfaceVal(sys.nsurf+1,5,nvi);    % image space refractive index (
    vitreous)
```

A lens-only system can be set up by adding the lines below after configuring the GRINCU lens. Note that `nvi` refers to the refractive index of the vitreous humor:

```
sys.delSurface(1);                       % deletes dummy stop
sys.delSurface(1);                       % deletes cornea
sys.delSurface(1);                       % deletes anterior chamber
% now surface (1) is the lens
sys.SetStop(1);                          % sets stop at the anterior lens
sys.SetSurfaceVal(0,5,nvi);              % object space refractive index
```

4.3.2 Doublet

In this case, after creating the eye optical system, the crystalline lens is divided into two surfaces, a *grincuA* and a *grincuP*, with thicknesses t_a and t_p corresponding to the anterior and posterior surfaces of the lens. Although they can be included, for simplicity, we will omit lens tilt and shift here.

```
%% anterior lens %%
sys.SetSurfaceVal(4,1,'grincuA');        % set lens type
sys.SetSurfaceVal(4,2,'GRINCU ant');     % set lens label
sys.SetSurfaceVal(4,3,Ra);               % anterior radius of curvature
sys.SetSurfaceVal(4,4,t);                % lens thickness
sys.SetSurfaceVal(4,6,4.5);              % anterior lens semidiameter
sys.SetSurfaceVal(4,7,Qa);               % anterior conic constant
% build the internal GRINCU distribution
sys.SetSurfaceParam(4,1, [step, p, ta, ns, nc, G, tor, theta]);
```

A new surface is added after (4) and configured as a grincuP (posterior region of the GRINCU lens) surface type. Note that in this configuration, the radius of curvature and conic constant of this surface are those of the interface. Therefore, it is necessary to execute `calcInterface()` to obtain these values.

```
%% calculate the interface parameters %%
interData = sys.calcInterface(Qa,Qp,G);
Ri = interData(1);
Qi = interData(2);

%% configure the posterior lens region %%
sys.addSurface(5);
sys.SetSurfaceVal(5,1,'grincuP');        % surface type
sys.SetSurfaceVal(5,2,'GRINCU pos.');    % surface label
sys.SetSurfaceVal(5,3,Ri);               % interface radius of curvature
sys.SetSurfaceVal(5,4,tp);               % posterior region thickness
sys.SetSurfaceVal(5,6,5);                % interface semidiameter
```

```
sys.SetSurfaceVal(5,7,Qi);              % interface conic constant
% build the internal GRINCU distribution
sys.SetSurfaceParam(5,1,[step, p, Rp, Qp, ns, nc, G, tor, theta]);
```

Last, the values of surface (6) must be changed to match the posterior lens geometry.

```
sis.SetSurfaceVal(6,3,Rp);              % radius of curvature
sis.SetSurfaceVal(6,7,Qp);              % conic constant
```

Similar to the singlet configuration, a lens-only system can be created by removing the first three surfaces and adjusting the object space refractive index to match that of the aqueous humor.

4.4 CROSS-VALIDATION RESULTS

A 30-year-old lens was modeled for ray tracing in Zemax and RTLib, using both singlet and doublet configurations. Several values of the external surfaces' conic constants Q_a, Q_p, and the curvature gradient G were tested to evaluate their effects on lens power and aberrations. The conic constant values were $Q_a = -4, -3, -2$, and -1, with $Q_p = Q_a + 1$; the curvature gradient parameter values were $G = -2, -1, 0$, and $+1$.

The lens power calculation produced comparable results in RTLib (Matlab), Zemax, and the direct matrix product (Python). Both RTLib and Zemax showed a maximum difference of 0.3% compared to the matrix product. Doublet and singlet versions yielded equivalent results. As illustrated in fig. 4.1a, when the anterior conic constant is fixed ($Q_a = -3$), more negative G values increase lens power. In contrast, with a fixed value for the curvature gradient parameter ($G = +1$), more negative Qa values result in reduced lens power (fig. 4.1b).

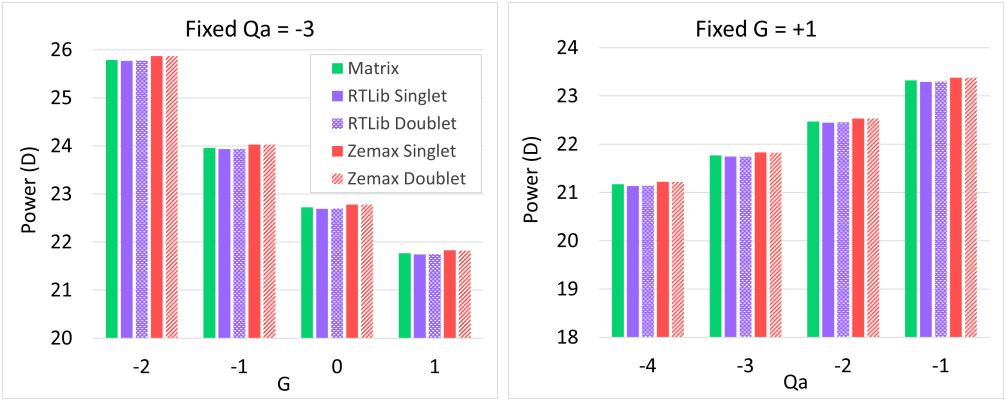

(a) Dependence on G. **(b)** Dependence on Q_a.

Figure 4.1: Comparison of lens power results for different ray tracing programs and lens configurations.

Similar to lens power, the results for the image principal plane position obtained from both software programs and the direct matrix product were

generally consistent, with a maximum difference of 0.6% across both ray tracing programs and configurations. Note that the image principal plane is measured from the rear surface of the lens. Figure 4.2a illustrates the relationship between the position of the image principal plane and G, using a fixed $Q_a = -3$, while Figure 4.2b shows its relationship with Q_a, with G held constant at $+1$. More negative values for both G and Q_a lead to increasingly negative image principal plane positions; in other words, more negative values of G and Q_a shift the image principal plane toward the anterior region.

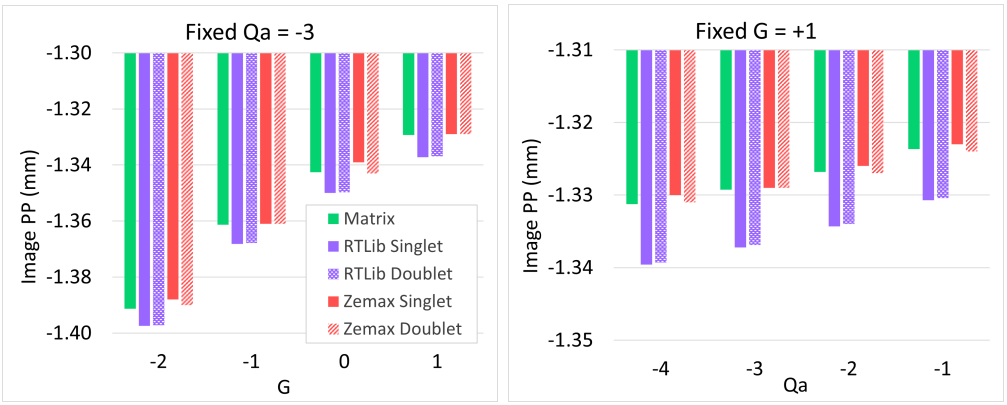

(a) Dependence on G. **(b)** Dependence on Q_a.

Figure 4.2: Comparison of image principal plane position results for different ray tracing programs and lens configurations.

Figure 4.3 compares the transverse aberration in microns as a function of pupil height for an on-axis ray fan, examining two values of Q_a in the concentric configuration ($G = +1$). For the sake of clarity, the doublet implementation in RTLib was excluded from these figures. There was strong agreement between the singlet and doublet in Zemax, as well as with the RTLib singlet. The differences were minor and tended to gradually increase with pupil height, with the largest difference (13%) occurring only for the most peripheral rays at a pupil height of 4 mm for $Q_a = -4$. Transverse aberration remained negligible

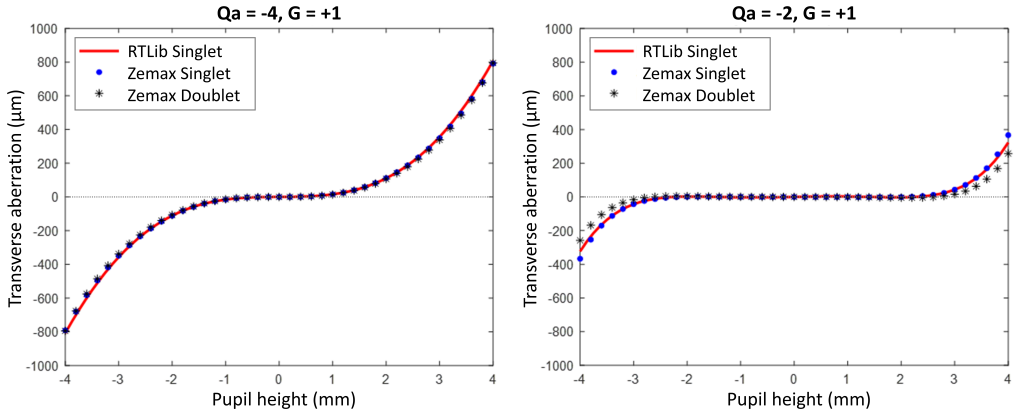

Figure 4.3: Ray bundles for $Q_a = -4$ (left) and $Q_a = -2$ (right), computed in Zemax and RTLib for the concentric configuration $(G = +1)$.

up to a pupil height of 2.5 mm for $Q_p = -2$ (section 4.4), while it reached 200 µm at the same pupil height and nearly 800 µm at the pupil edge for $Q_a = -4$ (section 4.4), indicating a strong effect of Q_a values on transverse aberrations (spherical aberration).

These results allowed us to cross-validate the various implementations and model versions of both paraxial (figs. 4.1 and 4.2) and finite ray tracing (fig. 4.3).

RESULTS

5 OPTICAL PERFORMANCE OF THE GRINCU LENS IN SYNTEYES

5.1 OPTICAL PERFORMANCE OF EYE MODELS

Eye models are invaluable tools in visual optics; they provide the best insights into the relationship between structure (anatomy) and function (optical properties and performance), making them essential for understanding human eye optics. Over time, the realism and fidelity of eye models have significantly improved, accounting for changes due to age [3, 63, 65, 66, 70], accommodation [36, 67, 81], or both [37, 38]. Traditional eye models typically represent average emmetropic eyes and are often limited by their generic parameters, failing to account for the intersubject variability highlighted in epidemiological studies. Reliable refractive calculations for personalized treatments require a detailed description of the eye's biometric dimensions and optical properties, and generic models fall short when attempting to replicate the optical behavior of an individual eye exactly. One critical factor in enhancing eye model accuracy is the inclusion of a gradient index (GRIN) inside the crystalline lens.

The GRIN distribution within the lens influences not only lens power but also ocular aberrations [59, 71, 73, 95, 96] and peripheral power [74]. Recent research also suggests that gradients in the curvature of the IIS can significantly impact lens performance [39]. However, comprehensive testing of these GRIN and GRCU models requires extensive ocular biometric data, which is currently limited or incomplete in public datasets. To bridge this gap, synthetic data platforms like SyntEyes offer an innovative solution. SyntEyes [2] is a platform that generates synthetic, virtually unlimited, biometric data sets that mimic the statistical properties and physiologically realistic variations found in actual human eye population data. This tool is valuable for vision scientists and clinicians as it allows for the simulation and analysis of optical properties without the need for individual biometric measurements.

In this Chapter, we examine how various curvature gradients of the crystalline lens iso-indicial surfaces (IIS) influence the performance of 200 randomly generated SyntEyes. Using customized Matlab ray tracing software to model light propagation through the eye optical system, we compute the cardinal points and power and evaluate the Zernike aberration coefficients for five different inner curvature gradients of the lens.

5.2 EYE BIOMETRIC DATA: SYNTEYES

The biometric data used in this study consists of the first 200 entries of a file containing 1000 randomly generated SyntEyes, which was provided as a supplement to the original paper [2]. SyntEyes is a higher-order statistical model based on the clinically measured biometry of 312 healthy right eyes

of White Western European individuals (57.1% women). The cohort had a mean spherical equivalent of -1.23 ± 2.29D (ranging from -8.63 D to $+3.63$ D), measured under non-cycloplegic conditions. The data generated by the model is statistically indistinguishable from the data it is based on and captures the typical biometric variations found in the general population in Belgium between the ages of 20 and 60. Table 5.1 displays the mean values and standard deviations of the SyntEyes variables considered in this study. Other biometric parameters that remained fixed for all eyes throughout this study are presented in Table 5.2.

Table 5.1: Biometry of the SyntEyes [2] and other data. Standard deviations are included where average values are provided.

Symbol	Unit	Value (SD)	Description
r_{ca}	mm	7.79 (0.23)	Anterior corneal radius of curvature
r_{cp}	mm	6.55 (0.24)	Posterior corneal radius of curvature
r_{la}	mm	10.56 (1.23)	Anterior lens radius of curvature
r_{lp}	mm	-6.95 (0.77)	Posterior lens radius of curvature
CCT	µm	548.49 (32.48)	Central corneal thickness
ACD*	mm	2.88 (0.42)	Anterior chamber depth
LT	mm	4.05 (0.39)	Lens thickness
VCD	mm	16.30 (1.00)	Vitreous chamber depth
LSh_x	mm	0.11 (0.03)	Lens shift, x-direction, relative to principal axis
LSh_y	mm	-0.07 (0.19)	Lens shift, y-direction, relative to principal axis
LTi_x	deg	3.68 (1.06)	Lens tilt around the y-axis
LTi_y	deg	0.10 (0.89)	Lens tilt around the x-axis
n_l	-	1.4316 (0.0092)	Refractive index (homogeneous lens model)

* Distance considered from the corneal endothelium to the anterior lens.

5.3 LENS MODELS

Each of the 200 SyntEyes models was configured with three distinct crystalline lens types: a two-surface homogeneous lens with a constant equivalent index nL (refer to Table 5.1 for the average value), a GRIN lens [66], and a GRINCU lens [3]. Detailed explanations of these lens models and their main characteristics can be found in Chapter 2. For the GRINCU lens specifically, we examine ocular optical performance using five different curvature gradient parameter G values:$+1$, 0, -1, -1.5, and -2, assuming for simplicity that $G_a = G_p = G$. Two particular cases are worth mentioning: when $G = 0$, the absence of a curvature gradient results in iso-indicial surfaces that are parallel to the lens's outer surface, and when $G = +1$, the IIS form concentric conics with the outer surfaces of the lens. The GRIN and the GRINCU lens model with $G = +1$ have an iso-indicial surface distribution concentric with the lens's external surfaces. While these models share significant similarities and provide comparable optical properties, they are not identical due to their distinct parametrization (r^2 for

the GRIN and z_0 for the GRINCU lens model). This difference in formulation changes the IIS distribution and the shape of the interface between the anterior and posterior regions.

Table 5.2: Other biometric parameters used in this study.

Symbol	Unit	Value	Description
Q_{ca}	-	-0.26	Anterior corneal conic constant[1]
Q_{cp}	-	0	Posterior corneal conic constant[2]
Q_{la}	-	-3.1316	Anterior lens conic constant[2]
Q_{lp}	-	-1.05	Posterior lens conic constant, modified[2]
p	-	3.3	Exponent of the refractive index distribution[3]
n_{co}	-	1.3774	Refractive index of the cornea[4]
n_0	-	1.3374	Refractive index of aqueous and vitreous humors[4]
n_s	-	1.3726	Refractive index of the lens surface[4]
n_c	-	Optimized	Refractive index of the lens center (GRIN, GRINCU)
RT	mm	0.20	Retinal thickness
t_a	mm	$0.6 \times$ LT	Axial thickness of anterior lenticular region[3]
t_p	mm	$0.4 \times$ LT	Axial thickness of posterior lenticular region[3]

[1] Kiely *et al.*, 1982
[2] Navarro *et al.*, 1985
[3] Navarro *et al.*, 2007
[4] Navarro, 2014

5.4 RAY TRACING

Using customized ray tracing software in Matlab, we calculated the cardinal points, overall power of the eye and lens, and ocular aberrations for each lens model. Ray tracing was performed using a wavelength of 555 nm and an entrance pupil diameter of 5 mm. Figure 5.1 provides a schematic representation of the optical system configuration of the eye. Within the dataset of 200 eyes, the radius of curvature and thickness of each surface varied, while the conic constants remained constant across all surfaces. The posterior cornea and retina were modeled as spheres. The anterior cornea was modeled as a prolate ellipse (with its major axis stretching along the principal axis). Both the anterior and posterior lens surfaces were hyperbolic, with Q values given in Table 5.2. All studied eyes included lens tilt and shift but did not account for lens toricity (astigmatism). The internal refractive index and iso-indicial curvature profiles of the GRIN and GRINCU crystalline models were assumed to be continuous.

To enable a standardized basis for comparison, the refractive index at the center (n_c) of the GRIN and GRINCU lenses was optimized to match the optical power of the corresponding homogeneous lens. The optimization was performed by running Matlab's function *fminsearch* on the lens power with a tolerance of 10^{-5} diopters.

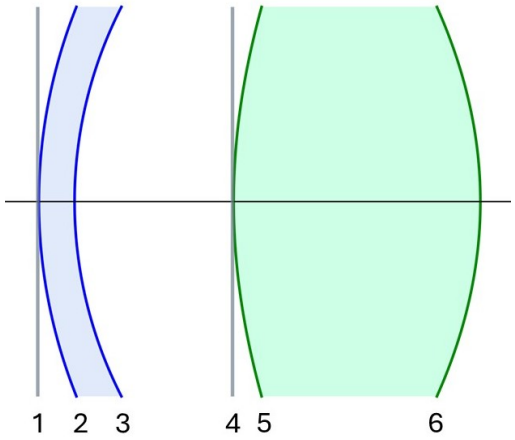

Figure 5.1: Configuration of the optical surfaces through which ray tracing was performed. 1. Entrance pupil, 2. Anterior cornea, 3. Posterior cornea, 4. Iris (stop), 5. Anterior lens, 6. Posterior lens.

5.5 RESULTS

Table 5.3: Average results of the paraxial analysis for the lens and eye optical systems. Standard deviations are shown in parentheses.

Model	G	n	VH_l (mm)	$V'H'_l$ (mm)	VH_e (D)	$V'H'_e$ (mm)	BFL_e (mm)	P_e (mm)
Equivalent	-	1.4316	2.319	−1.529	1.531	−5.605	16.465	60.67
		(0.0092)	(0.235)	(0.163)	(0.095)	(0.324)	(0.692)	(2.04)
GRIN	-	1.4344	2.393	−1.482	1.553	−5.608	16.481	60.61
		(0.0092)	(0.243)	(0.147)	(0.097)	(0.323)	(0.686)	(2.03)
GRINCU	+1	1.4341	2.372	−1.503	1.547	−5.612	16.471	60.63
		(0.0093)	(0.238)	(0.152)	(0.096)	(0.323)	(0.688)	(2.04)
GRINCU	0	1.4316	2.338	−1.542	1.536	−5.626	16.448	60.65
		(0.0092)	(0.230)	(0.161)	(0.095)	(0.322)	(0.691)	(2.04)
GRINCU	−1	1.4284	2.294	−1.592	1.524	−5.644	16.419	60.69
		(0.0093)	(0.218)	(0.175)	(0.094)	(0.322)	(0.696)	(2.05)
GRINCU	−1.5	1.4260	2.266	−1.625	1.515	−5.656	16.400	60.71
		(0.0097)	(0.209)	(0.186)	(0.093)	(0.322)	(0.700)	(2.05)
GRINCU	−2	1.4220	2.241	−1.671	1.508	−5.674	16.376	60.72
		(0.0112)	(0.208)	(0.209)	(0.093)	(0.323)	(0.706)	(2.05)

5.5.1 Lens Paraxial Analysis

The average crystalline lens power of all 200 SyntEyes was 22.27 D (SD = 2.04), corresponding to an average focal length of 60.064 mm. The average lens central refractive index required to match the equivalent homogeneous lens power was the highest for the GRIN lens model ($n_c = 1.4344$). It decreased with more

negative values of G, reaching $n_c = 1.4220$ for $G = -2$ (see fig. 5.2). The central lens refractive index values were higher than the equivalent refractive index of the homogeneous lens for $G = 0$ and $G = +1$ and lower for negative values of G.

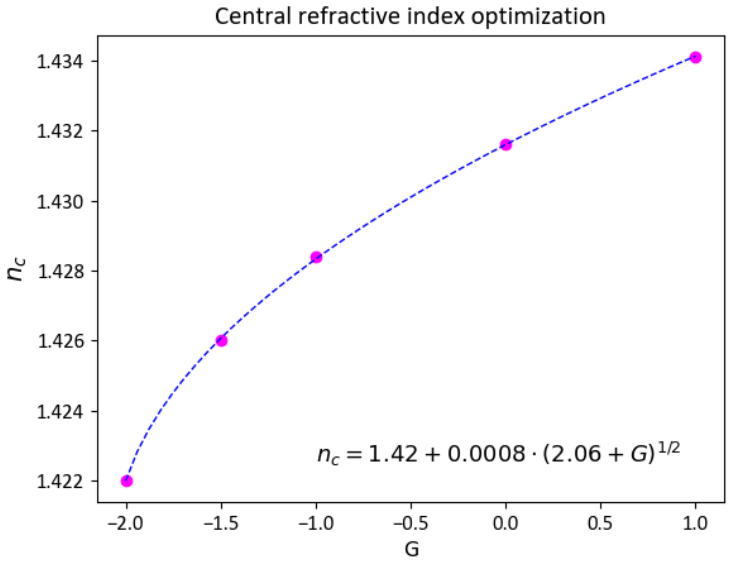

Figure 5.2: Variation of the central refractive index of the GRINCU lens with the curvature gradient parameter.

The principal planes of the lens exhibited a slight but noticeable shift in position for the GRIN and GRINCU models relative to the equivalent lens. Specifically, the principal planes shifted backward for the GRIN and GRINCU model with $G = +1$ and forward for the GRINCU configuration with $G < 0$ (fig. 5.3, Table 5.3). All GRIN and GRINCU models showed a reduced distance

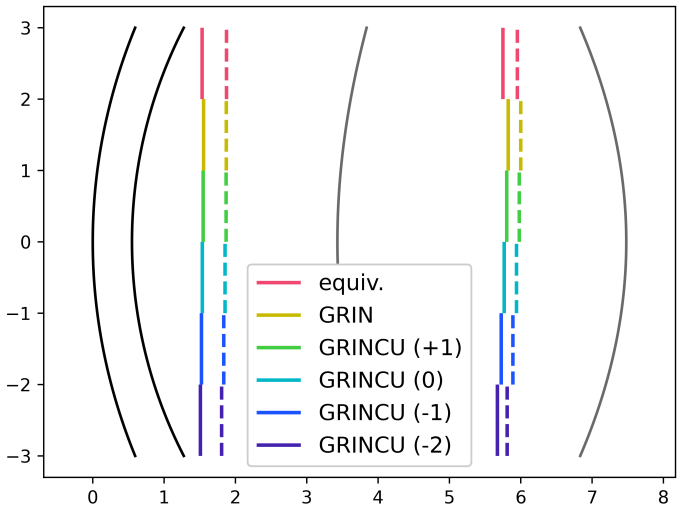

Figure 5.3: Position of the object (solid line) and image (dashed) principal planes of the lens (right) and the eye (left).

between the object and image principal planes compared to the equivalent lens. As did the focal length, the lens power remained constant across the models by design. As a result, the displacement of the principal planes with the varying curvature parameter G led to corresponding changes in the lens's front and back focal lengths (FFL and BFL). See Table A.4 in Appendix A for the full results of the paraxial analysis of both the lens and the eye.

5.5.2 Eye Paraxial Analysis

The average eye power varied between 60.63 and 60.72 diopters (0.09 D difference) for the GRINCU lens models with G = +1 and G = −2, respectively. The GRIN and GRINCU models with G = +1 and G = 0 showed lower power than the equivalent lens, while the GRINCU models with negative G values exhibited higher power. The principal planes of the eye system were shifted in a similar way as the principal planes of the lens, albeit by a smaller amount (fig. 5.3), and there was also a shortening of the distance between the object and the image's principal planes (Table 5.3).

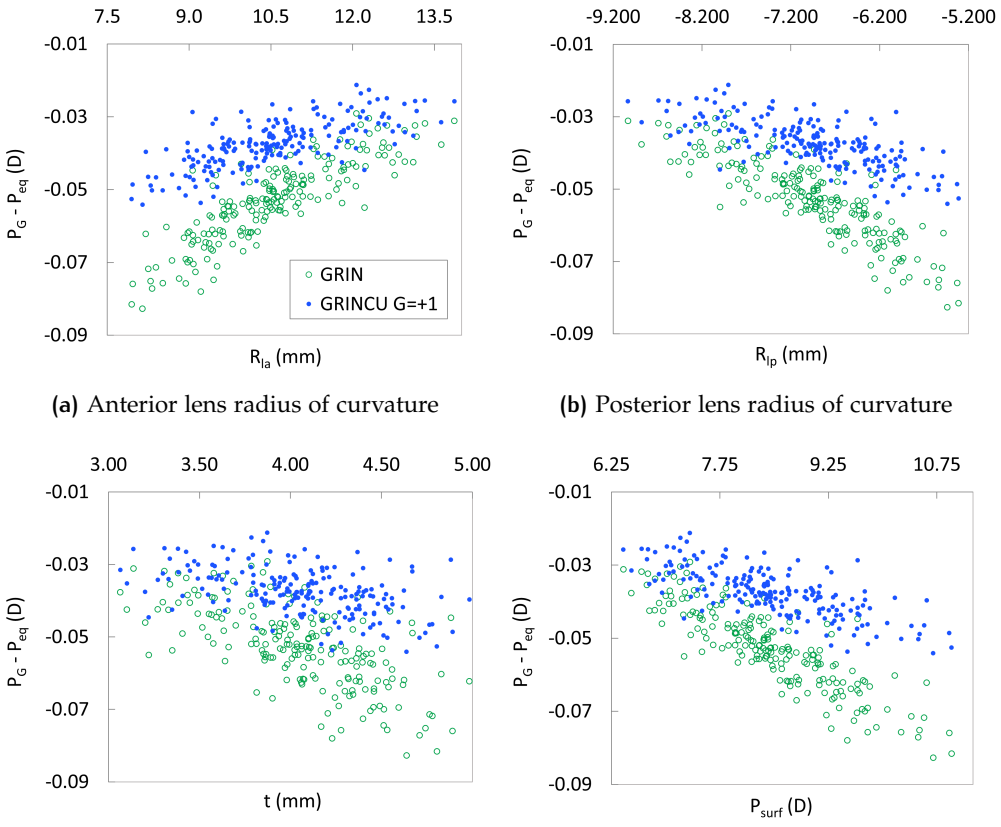

(a) Anterior lens radius of curvature

(b) Posterior lens radius of curvature

(c) Lens thickness

(d) Lens surface power

Figure 5.4: Difference in eye power between the GRIN and GRINCU concentric (G = +1) lens models and the homogeneous lens as a function of various lens geometrical parameters

Figures 5.4 and 5.5 compare the difference in optical power between the gradient index lens configurations and the equivalent lens model as a function

of lens geometry and GRINCU lens surface power. Figure 5.4 compares the GRIN and GRINCU models with G = +1 against each other, as they correspond to remarkably similar IIS configurations. The two models exhibit comparable eye powers, with a maximum difference of less than 0.1 D. The GRINCU model with G = +1 yields more ocular power than the GRIN model for thicker and more convex lenses. Both lens models demonstrate a closer agreement with the equivalent lens model and with each other when considering thinner and flatter lens geometries.

Figure 5.5 shows the results specifically for the GRINCU lens models. The curvature gradient parameter plays a significant role in determining the total eye power, with G $<$ 0 (IIS curvatures increasing towards the center of the lens) leading to an increase in power and G $\geqslant$ 0 (parallel, concentric, or decreasing curvature towards the center IIS) resulting in a decrease in power. Once again, a more substantial agreement is observed across all lens models when considering flatter and thinner lens geometries. In contrast, thicker, more powerful lenses with steeper radii show more significant differences in equivalent lens power.

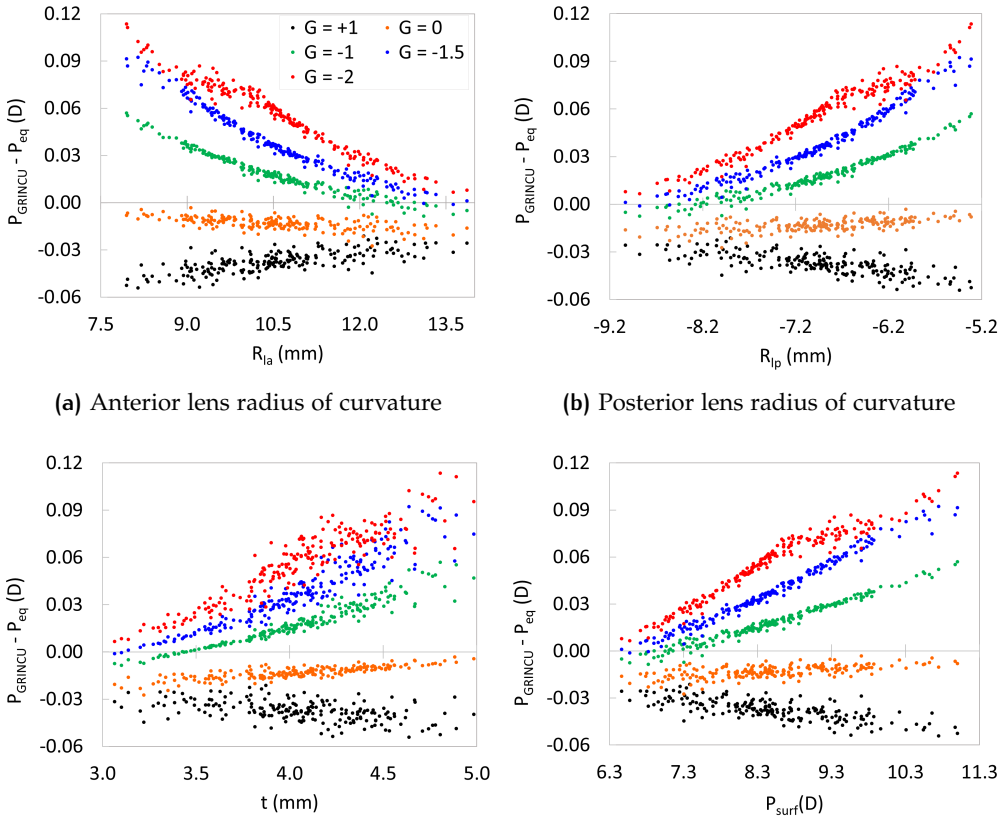

(a) Anterior lens radius of curvature

(b) Posterior lens radius of curvature

(c) Lens thickness

(d) Lens surface power

Figure 5.5: Difference in average eye power for different G values (GRINCU model) relative to the homogeneous lens power, as a function of lens geometrical parameters and lens surface power.

5.5.3 Eye Aberrations

The GRINCU models exhibit definite trends regarding the impact of curvature gradient on the ocular wavefront aberrations Zernike coefficients analyzed: oblique (Z3) and horizontal/vertical (H/V) astigmatism (Z5), defocus (Z4), vertical and lateral coma (Z7, Z8), and primary spherical aberration (Z12). Both astigmatisms are higher for the GRIN and GRINCU lens models than for the equivalent lens, decreasing for increasingly negative values of G (steeper curvature gradients). Defocus changes slightly for the GRIN and GRINCU models relative to the equivalent lens, decreasing relative to $G = 0$ as G becomes more negative. Lateral and vertical coma are reduced in the GRIN and all GRINCU lens models except for $G = -2$, which shows increased vertical coma (Z7) relative to the equivalent lens. Primary spherical aberration is higher than the equivalent lens for the GRIN and GRINCU models with $G \geqslant 0$ and lower for GRINCU models with $G < 0$. See Table A.1 for detailed Zernike aberration term results.

A two-sample T-test with unequal variance showed statistically significant differences between the equivalent homogeneous model and the GRIN and GRINCU lens models in both astigmatisms (Z3, Z5), lateral coma (Z8), and spherical aberration (Z12). Vertical coma (Z7) differed from the equivalent lens for the GRIN and GRINCU lenses with $G \geqslant 0$. The same test against the GRIN model revealed substantial differences with all GRINCU lenses, except those with $G = +1$, for primary spherical aberration. Significant differences in vertical and lateral coma were apparent for negative G values of GRINCU lenses. Notably, no statistically significant disparity in defocus was found across the models. The T-test results for the analyzed aberrations are detailed in Tables A.2 and A.3 of Appendix A.

5.6 DISCUSSION

5.6.1 Lens Power

The lens power is determined by two main factors: the internal gradient index of the lens and the curvature of its outer and inner surfaces. An IIS configuration where the curvature either decreases from the outer surface towards the center of the lens or stays constant ($G \geqslant 0$) requires a higher contribution from the central refractive index to achieve the desired lens power. Conversely, a configuration where the curvature increases from the outer surface towards the center ($G < 0$) requires a lower central refractive index to achieve the same desired power. A first-order analysis of this balance between the curvature gradient parameter G and the lens central refractive index n_c reveals a quadratic relationship (Figure 2). The coefficient values of this quadratic law will depend on multiple factors, like the target lens power, conic constants, radii of curvature of the external surfaces, and the lens surface refractive index.

In a homogeneous thick lens, the principal planes are positioned closer to the optically most powerful surface, with symmetrical lenses having centered principal planes. In the equivalent crystalline lens, the principal planes are

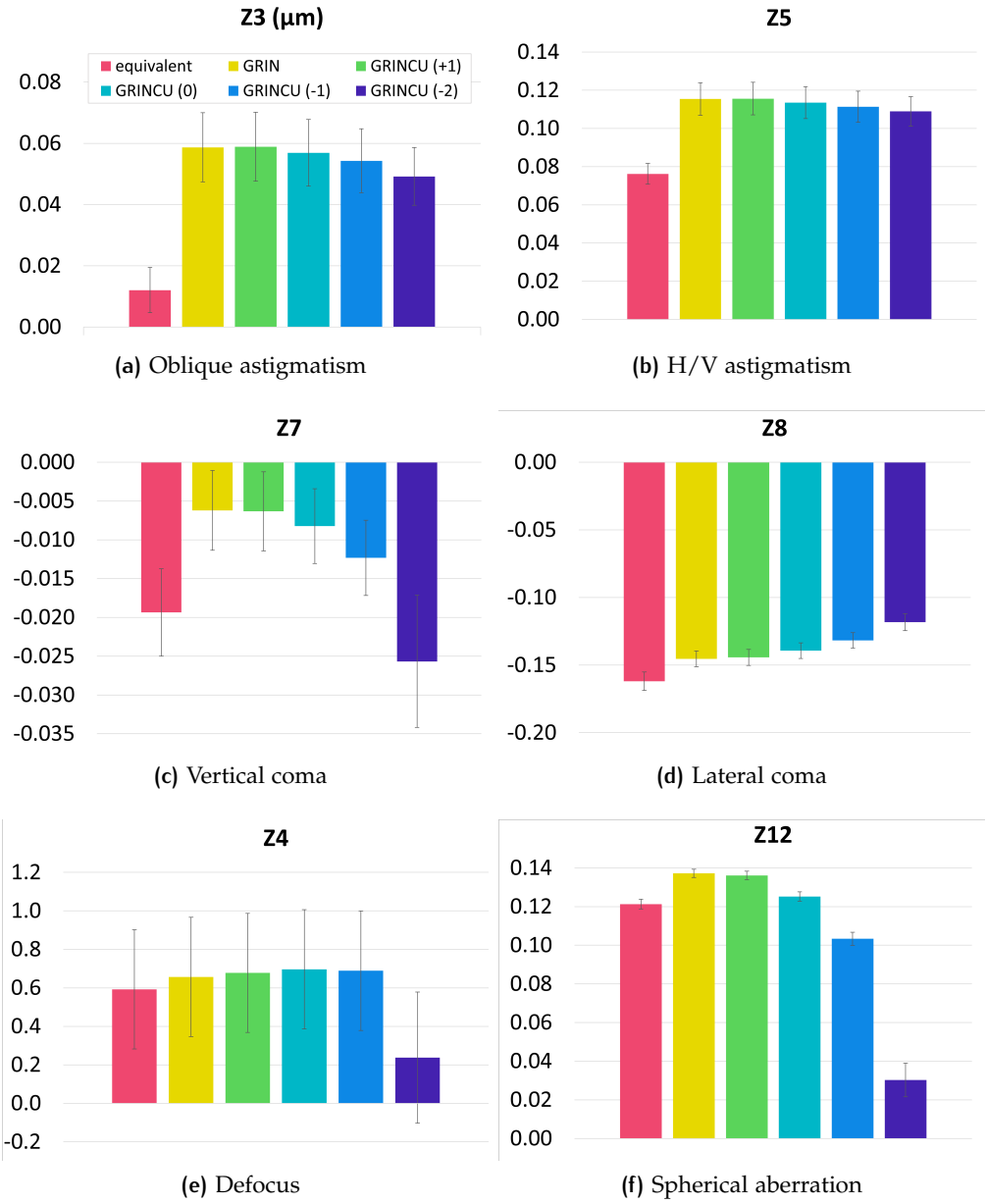

(a) Oblique astigmatism

(b) H/V astigmatism

(c) Vertical coma

(d) Lateral coma

(e) Defocus

(f) Spherical aberration

Figure 5.6: Aberration coefficients in microns (µm) as a function of curvature gradient, compared with the equivalent and GRIN lens models. The number in parenthesis denotes the G value of the GRINCU lens model

located toward the back of the lens, which has greater curvature. Let us consider the curvature gradient structure inside the lens for the highest and lowest values of G analyzed. If we consider the highest and lowest G values, $+1$ and -2, the total gradient ranges from $+2.13z_0$ to $-4.26z_0$ in the anterior and from $+0.05(z_0 - t)$ to $-0.10(z_0 - t)$ in the posterior region. The curvature gradient in the anterior region significantly impacts the lens's optical performance since the IIS curvatures change more drastically with G compared to the posterior region. Altering the curvature gradients results in changes in the power balance between the anterior and posterior regions of the lens, leading to the displacement of the principal planes towards the front of the lens for

$G < 0$ and towards the back of the lens for $G \geqslant 0$. These findings align with previous research indicating that an iso-indicial curvature gradient induces a shift in the principal planes compared to a homogeneous lens [98].

5.6.2 Principal Planes of the Eye

The displacement of the lenticular principal planes translates into a slight displacement of the ocular principal planes. The total ocular power, P_{eye}, and principal planes are computed as a function of the corneal power, P_{cornea}, lenticular power, P_{lens}, and distance $\overline{H_1' H_2}$ between the image principal plane of the cornea H_1' and the object principal plane of the lens H_2 (see eq. (5.1)). Since the position of the principal planes of the cornea does not change regardless of the lens model used, a change in the position of the principal planes of the lens results in a shift in the principal planes of the eye. Moreover, because P_{cornea} and P_{lens} are kept constant for each SyntEye, this distance also determines the variation in ocular power across lens models.

$$P_{eye} = P_{cornea} + P_{lens} - \frac{\overline{H_1' H_2} \cdot P_{cornea} \cdot P_{lens}}{n_0} \tag{5.1}$$

5.6.3 Eye Aberrations

It is commonly accepted that the internal optics significantly balance or compensate for the cornea's spherical aberration (Z12) and coma (Z7, Z8). Several studies analyzing the distinct contributions of the cornea and the lens to the overall ocular spherical aberration agree that the lens compensates for corneal spherical aberration [71, 99, 100] and that the gradient index plays a significant role in the crystalline lens spherical aberration at all ages, especially in young eyes [72, 73]. We found that the GRIN and GRINCU lens models with a negative curvature gradient ($G \geqslant 0$) increase spherical aberration relative to the equivalent lens model, and GRINCU lenses with a positive curvature gradient ($G < 0$) decrease it. The interplay of the gradient index and curvature gradient inside the lens may help explain the decoupling between the lenticular and corneal spherical aberration that occurs with aging.

In natural eyes, astigmatism (Z3, Z5) is caused by toric corneal and lenticular surfaces and tilted or displaced lenses. As the main focus of this study is the impact of the lens' internal properties on ocular performance, we modeled the corneal and lenticular surfaces as rotationally symmetric conics to reduce computational time. We did, however, incorporate lens tilt and shift. The GRIN and GRINCU lenses exhibited higher oblique (Z3) and H/V astigmatism (Z5) than the equivalent lens by roughly the same value, and a positive curvature gradient (IIS surfaces curving more towards the center) reduced the difference. An in vivo study on young emmetropic eyes [100] revealed that the lens compensated for corneal horizontal/vertical astigmatism but not for oblique astigmatism. Another study focusing on adult eyes [101] indicated that corneal and lenticular astigmatism offset each other in young individuals, a balance that diminishes with age. More recently, research on the role of the lens gradient index profile and ocular aberrations using a theoretical age-dependent GRIN model [72]

found that the lens gradient index contributes to corneal horizontal/vertical astigmatism in young eyes but compensates for it in older eyes. Because the present work is based on a statistical model over a wide range of ages, no direct comparison is possible for specific ages. However, these findings propose that the gradient index and curvature have distinct contributions to total ocular astigmatism, and their changes with age may help diminish it.

Coma (Z7, Z8) results from the principal planes being curved surfaces rather than flat planes [102]. Vertical coma arises from the different transverse magnifications of the rays passing through the lens's center and periphery. Lateral coma, on the other side, results from axial and peripheral rays focusing at different distances from the lens and is closely related to spherical aberration (Z12). We found that the lens gradient index reduced both vertical and lateral coma in the GRIN and GRINCU models relative to the equivalent lens. However, while the curvature gradient further enhances the reduction in lateral coma (Z8), it amplifies vertical coma (Z7), becoming higher than the equivalent lens for $G = -2$. One possible explanation for this effect is that the iso-indicial curvature gradient modifies the curvature of the lens's principal planes, increasing vertical coma with increasing curvature. Past studies on aberrations using eye models indicated that the lens compensates for corneal vertical coma [71], and the gradient index compensates for corneal horizontal coma [72]. The same in-vivo study mentioned above [100] showed that the lens has an additive effect on the corneal vertical coma but compensates for its horizontal coma, which aligns with our results for more negative curvature gradient parameters.

6 INTRACAPSULAR ACCOMMODATION MECHANISM

6.1 GULLSTRAND'S MECHANISM OF INTRACAPSULAR ACCOMMODATION

Determining the presence of an IAM (Intracapsular Accommodation Mechanism) in the crystalline lens is essential not only for historical and scientific reasons but also for its potential implications in designing accommodative intraocular lenses. As mentioned in Section 1.2.2.1, the occurrence and magnitude of an IAM are influenced by the lens model used (refer to Table 1.1). Thus, employing a realistic model is essential for evaluating the impact of the internal lens structure on its accommodating power. Given that the GRIN distribution and its changes during accommodation can significantly affect the IAM, and considering that Gullstrand's IAM is only possible in a non-homogeneous lens, GRIN models are deemed appropriate for studying this phenomenon. Most earlier models assumed a concentric shell configuration (refer to Navarro [75] for a list of significant GRIN models). Only the latest GRIN models [3, 70] have allowed for the modification of the inner curvature gradient, which has been shown to improve both lens power and accommodation amplitude [39]. The AVOCADO model [70] permits changes to the curvature gradient, albeit indirectly. To our knowledge, only the GRINCU model (which features a double gradient: refractive index and radius of curvature) [3] offers a direct and explicit way to modify the inner curvature gradient, thereby providing a better fit with experimental data.

This Chapter focuses on determining whether the human eye possesses an IAM as defined by Gullstrand. Specifically, we want to answer the question: if the crystalline lens were assumed to be homogeneous, would its equivalent refractive index increase during accommodation? To address this question, we tested for the presence of an IAM using a GRINCU accommodative lens model, which we believe is particularly well-suited for accurately quantifying an IAM. Our initial hypothesis is that, in addition to the increased curvature of the external lens surfaces, the gradient change in the inner shell curvature also plays a crucial role in accommodation [39]. While calculations in GRIN lens models can be complex, paraxial refraction accurately predicts clinical refraction [103] and the amplitude of accommodation [104]. Therefore, paraxial optics is a suitable approximation for evaluating the presence of IAM in accommodating GRIN lenses. Some proposed GRIN lens models [3, 70] have computed the paraxial power change during accommodation using ray tracing software or recursive algorithms that calculate the paraxial ray trajectories through each isoindicial surface. Instead, we employed a powerful and straightforward method based on the two-by-two ray transfer matrix [4, 87] presented in Chapter 3. Additionally, we examined whether a four-surface model based on the datasets could accurately predict the IAM obtained by a more realistic GRIN model.

In all cases, paraxial ray transfer matrix analysis was used to calculate the change in lens power and equivalent refractive index during accommodation, significantly simplifying the calculations.

6.2 ANALYSIS OVERVIEW

To assess the IAM in the GRINCU crystalline lens, we calculated the accommodative power change and the equivalent refractive index based on two separate sets of previously published experimental data [105–109]. These sources are likely the first in the literature to provide experimental geometry data for the lens nucleus surface. Refer to fig. 6.1 for a summary of the steps involved in the analysis.

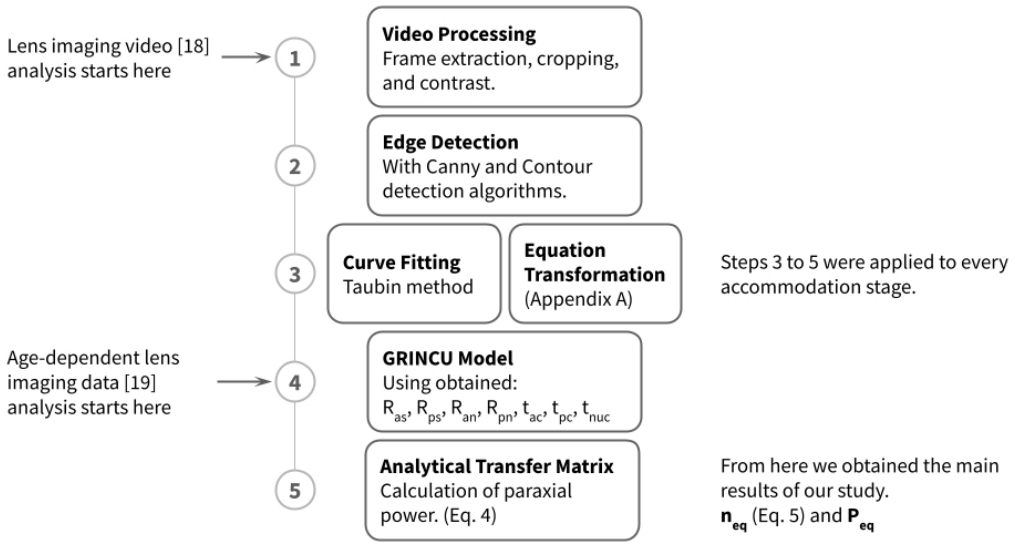

Figure 6.1: Flowchart showing the data analysis and results calculation process.

6.3 ACCOMMODATING LENS GEOMETRY

The first data set was obtained from an in-vivo accommodation video capturing both the external and internal geometry of the lens. The images were taken with a Topcon SL-45 Scheimpflug photographic camera (available at topconhealthcare.com) equipped with a charge-coupled device (CCD) attachment in place of the traditional film. The video depicts the lens of a 16-year-old individual as it disaccommodates from a maximum accommodation stimulus of 10.4 diopters (D) [105].

The second data set was gathered from a study involving 100 participants, whose ages ranged evenly from 18 to 70 years [106]. Scheimpflug photographic data were collected at 2D-intervals, spanning from zero to the maximum accommodation stimulus for all subjects. From this data, lens radii of curvature and thicknesses were extracted for the recorded ages and accommodation states, resulting in seven equations that describe the external and nucleus geometry of the lens based on age and accommodation [107–109]. This second data set

provided an average trend for a group of 100 lenses, unlike the first data set, which was based on a single individual.

6.3.1 16-year-old Lens

The first in-vivo experimental data were downloaded as a Scheimpflug greyscale video from an online publication by Hermans et al. [105]. This video was processed with Python [110] and OpenCV [111] to extract the pixel coordinates of the accommodating surfaces. The authors had already corrected their published video for two types of distortion: Type I, due to the inclined position of the CCD camera, and Type II, due to refraction through the cornea and anterior lens surface. Additionally, the surfaces of the nucleus had been fitted to central conics with the Levenberg-Marquardt method [105], so no further corrections were needed. The fitted nuclear boundaries are displayed as a green overlay in the published video. To extract the Cartesian coordinates of the surfaces of the lens, we analyzed the video in four steps:

1. We extracted, numbered, and cropped the video files to center the crystalline lens and saved them as a JPG file. The size of the video frames was 166 by 187 pixels.

2. The two external surfaces were mapped with Canny edge detection [112], followed by a contour detection algorithm, which returns a set of curves joining all the continuous points along the boundary.

3. The nucleus contour was mapped using the author's fit, shown as a green contour in the video. We, therefore, applied a green mask, eroded the edge, and used the contour detection function to find the boundary at each accommodative stage. All functions used in steps 1-3 are part of the OpenCV Python package (*Canny*, *findContours*, *drawContours*, *cvtColor*, and *erode*).

4. Finally, the unaccommodated thickness of the nucleus provided by Hermans *et al.* [105], i.e., $2.48\,\mathrm{mm}$, was used to calculate the pixel-to-mm ratio for the images. For all of the processed images, the origin of the coordinate system was set at the $(0,0)$ pixel.

At this stage of the analysis, each of the four lens surfaces at every accommodation stage in the video was represented by a contour defined by a set of (z-axial, ω-radial) coordinates. With four contours for each accommodation step or video frame, this amounted to 100 contours in total. To determine the surfaces' radii of curvature and conic constants, we employed Taubin's method for ellipse fitting [113] (detailed in Appendix B). This was followed by an equation transformation [114] to convert the quadric implicit equation into its canonical form (explained in Appendix C). Taubin's fitting algorithm is particularly well-suited for conic fitting due to two main features:

a) It uses linear least squares, which makes it simple and guarantees both convergence and a unique solution;

b) It uses a coordinate normalization that strongly enhances its robustness against displacements in the 3D space. Furthermore, such normalization has also shown (in an unpublished study from our laboratory) high accuracy in estimating the radius and conic constants, even in reduced conic cords.

The video data yielded several fits with RMS fit errors exceeding 20%, which were subsequently excluded from the analysis. All fits were included for the anterior external surface. In contrast, two fits for the posterior external surface, nine for the anterior nucleus surface, and eight for the posterior nucleus surface were excluded. The fits that were included had errors of less than 0.4% across all analyzed surfaces. Figure 6.2 provides examples of both included and excluded fits.

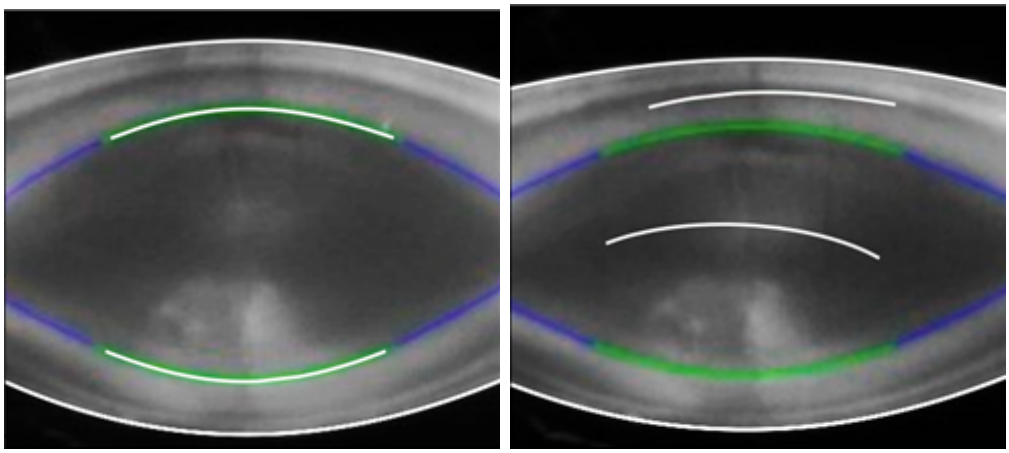

(a) All four fits were included. **(b)** Nucleus surface fits were excluded.

Figure 6.2: Example of fits that were included or excluded from the analysis. The detected contours appear as white curves overlaying the original images.

The resulting radii of curvature, along with the thicknesses of the cortex and nucleus, are illustrated in fig. 6.3. Since the conic constants were unnecessary for calculating paraxial lens power, they were omitted. It should be noted that the sequence of frames is reversed in all figures to depict increasing accommodation. To analyze these more or less correlated data points, we first computed a trend line. We then refined the linear regression by eliminating points that fell outside a confidence interval of $\pm 1.8\sigma$ and recalculated the slope and intercept, which significantly enhanced the R^2 value. Refer to Table 6.1 for the obtained fit parameters as a function of accommodation, as well as their R^2 values. The intercept (y_0) represents the first frame, which corresponds to the maximum accommodation stimulus of 10.4 D, and the slope value (m) is the variation with accommodation. R_{as}, R_{ps}, R_{an}, and R_{pn} are the radii of curvature of the anterior and posterior surfaces of the lens and the anterior and posterior surfaces of the nucleus, respectively. Q_{as} and Q_{ps} are the conic constants of the lens's anterior and posterior surfaces. And lastly, t_{ac}, t_{pc}, and t are the anterior cortex, posterior cortex, and total lens thicknesses.

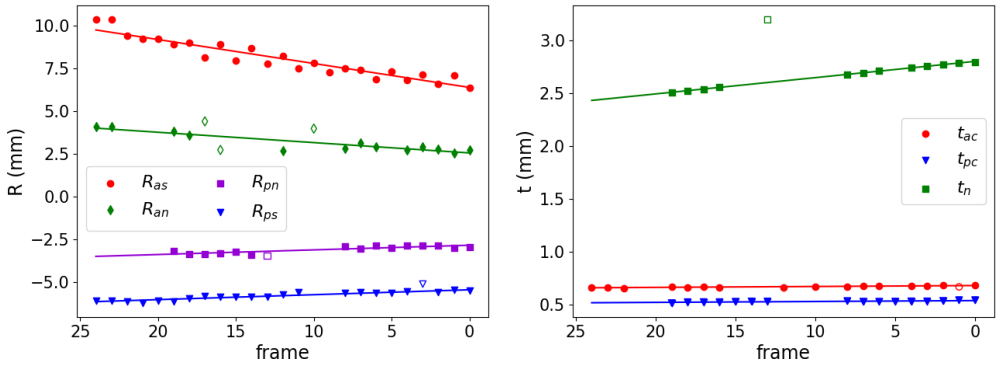

(a) Radii of curvature.

(b) Axial thickness of the lens cortex and nucleus.

Figure 6.3: Linear regression fits obtained from fitting the Scheimpflug video contours. The solid markers represent kept points, the empty markers show the points outside the confidence interval, and the solid line is the best-fit line.

Table 6.1: Scheimpflug Video Linear Regression Parameters (data set 1) [105].

	Q_{as} †	Q_{ps} †	R_{as}	R_{ps}	R_{an}	R_{pn}	t_{ac}	t_{pc}	t
y_0 [a]	−3.10	−0.37	6.37	−5.44	2.55	−2.84	0.68	0.54	4.02
m [b]	−9.24	−3.67	14.0	−2.88	6.04	−2.71	−0.0873	−0.0854	−1.70
R^2	0.134	0.558	0.917	0.884	0.846	0.743	0.710	0.674	0.999

[a] mm
[b] $mm/frame$
† Q_{as} and Q_{ps} are unitless.

6.3.2 Age-Dependent Study: Direct Fit

The external and nucleus geometry parameter equations for the lens, based on age-dependent data, were sourced directly from published studies: changes in lens cortex and nucleus thickness with accommodation [107], radii of curvature at zero diopters [108], and changes with age and accommodation [109]. All equations followed the format $y = y_0 + m_A \cdot yr + (m_B + m_C \cdot yr) \cdot D$, where age is in years and D represents the accommodation demand in diopters (see Table 6.2). In all equations, y_0 represents the 18-year-old unaccommodated lens. Calculations were performed for accommodating lenses of individuals aged 18, 29, and 45, with accommodation stimuli ranging from 0 D to 9 D.

6.4 MODEL IMPLEMENTATION

6.4.1 Refractive Index Distribution

The external parameters R_{as}, R_{ps}, Q_{as}, and Q_{ps} define the internal geometry of the iso-indicial surfaces. The refractive indices at the lens surface and lens core, respectively, are denoted by n_s and n_c. We consider the same refractive

Table 6.2: Scheimpflug photographic age and accommodation study fits for data set 2 [107–109]

	R_{as}	R_{ps}	R_{an}	R_{pn}	t_{ac}	t_{pc}	t_n
y_0	11.155	−8.267	3.782	−3.500	0.571	0.593	2.096
m_A (10^{-2}/yr)	−2.004	2.025	−0.5996	0.5537	1.2	0.5	−0.3
m_B (/D)	−0.4736	0.2788	−0.0776	0.1092	0.002	–	0.041
m_C (10^{-3}/(D · yr)	4.705	−4.375	−0.584	−1.010	–	–	–
18-year-old*	6.893	−5.758	3.084	−2.517	0.589	0.593	2.465
29-year-old*	7.539	−6.312	2.757	−2.620	0.937	0.738	2.378
45-year-old*	7.896	−6.618	2.577	−2.677	1.129	0.818	2.330

* Maximum accommodation values.
All quantities are in mm.

index for the anterior chamber and vitreous humor, labeled n_0. Last, t_a and t_p represent the axial thickness of the anterior and posterior regions of the lens.

The apical radius of curvature at any given IIS inside the GRINCU lens is given by eq. (2.8) in Chapter 2. Using the lens geometry obtained from the two datasets and assuming constant gradients, we computed g_a and g_p.

$$g_a = \frac{R_{as} - R_{an}}{t_{ac}} \tag{6.1a}$$

$$g_p = \frac{R_{pn} - R_{ps}}{t_{pc}} \tag{6.1b}$$

Where t_{ac} and t_{pc} represent the thicknesses of the anterior and posterior cortex, and R_{an} R_{pn} denote the radii of curvature for the anterior and posterior surfaces of the nucleus. In both situations, the resulting net curvature gradients are notably high, particularly in the anterior region of the lens. They decrease roughly linearly with accommodation (see fig. 6.5). This steep decrease in the radius of curvature towards the core might cause it to become zero or even reverse its sign within the nucleus, which is theoretically and physiologically implausible. To circumvent this issue, we employed distinct GRINCU configurations for the cortex and the nucleus: for the cortex, we applied the curvature gradients as calculated using eqs. (6.1a) and (6.1b) and illustrated in fig. 6.5, while within the nucleus, we assumed zero gradients, meaning $R_a(z_0) = R_{an}$ and $R_p(z_0) = R_{pn}$ for all z_0 values inside the nucleus (indicating no curvature gradient within the nucleus, thus the iso-indicial surfaces are parallel). Given that the refractive index is nearly constant within the nucleus, we can treat the nucleus as an almost homogeneous lens. Therefore, assuming constant curvature radii should not significantly affect our paraxial power calculations.

Each accommodative stage was modeled in Python for the four datasets: the 16-year-old lens in the video data and the three different ages (18, 29, and 45) selected from the age-dependent data set. We used refractive indices, defined at 587.56 nm, $n_a = n_v = 1.336$ [38] for the aqueous and vitreous humor, respectively, $n_s = 1.3709$ for the lens surface, and $n_c = 1.4181$ [19] for the lens core. The model implementation yielded an age- and external geometry-

dependent refractive index distribution, index derivatives, and iso-indicial surface profile for each accommodative stage.

6.4.2 Accommodative Power

The ABCD or ray transfer matrix provides a straightforward way to perform paraxial ray tracing and compute the cardinal points and power of a GRINCU lens [90]. This matrix formulation [1] is thoroughly explained in Chapter 3. Under this approximation, the GRIN contribution to the power is additive: the lens power is the sum of the GRIN and lens surface contributions to the power.

$$P = P_S + P_G = P_S + \int_0^t \frac{n'(z)}{n(z)R(z)}dz \tag{6.2}$$

Where P is the total lens power, and P_S and P_G are the contributions to the power by the lens surface and the internal GRINCU distribution. The surface power P_S was calculated with the standard homogeneous thick lens power equation using a refractive index equal to that of the surface $n_{lens} = n_s$ and the GRIN power P_G is given by an integral [1] (see eq. (3.14)). For each of the four cases studied, we computed the paraxial power at each accommodation step.

6.4.3 Equivalent Refractive Index

The effective refractive index introduced by Gullstrand [44] was the index that an unaccommodated two-surface homogeneous lens would require in order to deliver the same refractive power as an unaccommodated GRIN (or four-surface) lens, assuming both had the same external geometry. This equivalent index is found by replacing the GRIN lens power in the lensmaker's equation.

$$\begin{aligned} P_S =& P_a + P_p - \frac{tP_aP_p}{n_{eq}} \\ &\text{with } P_a = \frac{(n_{eq} - n_0)}{R_{as}} \text{ and } P_p = \frac{(n_0 - n_{eq})}{R_{ps}} \end{aligned} \tag{6.3}$$

Where P_a and P_p are the anterior and posterior surface powers, then solving for n_{eq} :

$$n_{eq} = n_0 + \frac{n_0(R_{as} - R_{ps}) + PR_{as}R_{ps} - \sqrt{(PR_{as}R_{ps} - n_0(R_{as} - R_{ps}))^2 + 4n_0PR_{as}R_{ps}t}}{2(-R_{as} + R_{ps} + t)} \tag{6.4}$$

Where n_{eq} is the equivalent refractive index, n_0 is the aqueous and vitreous humor refractive index, P is the unaccommodated total lens power, R_{as} and R_{as} the anterior and posterior surface radii of curvature, and t is the lens thickness.

Finally, for comparative purposes, we determined the equivalent power of a four-surface lens model comprising a homogeneous cortex and a homogeneous nucleus. This model uses two refractive indices: n_c for the nucleus, equal to the central index of the GRINCU model, and an equivalent refractive index n_{eqC} for the cortex, calculated to ensure the unaccommodated lens power matched that of a GRIN lens with identical external geometry. To compute the cortical equivalent refractive index in the four-surface model, we developed

a ray transfer matrix that sequentially tracks the ray path in reverse order across the lens surfaces and media: $M = S_{ps}T_{pc}S_{pn}T_nS_{an}T_{ac}S_{as}$. The matrices S_{as}, S_{ps}, S_{an}, and S_{pn} represent, respectively, refractions through the anterior and posterior external surfaces and anterior and posterior nucleus surfaces. Matrices T_{ac}, T_n, and T_{pc} are the translation matrices across the anterior cortex, nucleus, and posterior cortex. The paraxial refractive power of the four-surface lens was obtained by multiplying the matrix element M_{21} by the refractive index of the lens's surrounding media, $P_{eq,4} = n_0M_{21}$. Last, we optimized the equivalent cortex index n_{eqC} until $P_{eq,4}$ matched the lens power P in the unaccommodated state.

6.5 RESULTS

For each accommodation stage in all of the cases studied, we followed these steps in sequential order:

1. Extraction of the lens geometry:
   - Anterior and posterior lens external radius of curvature
   - Anterior and posterior nucleus surfaces radii of curvature
   - Anterior and posterior cortex thicknesses
   - Total lens thickness

   For the Scheimpflug video [105] (data set 1), we obtained these parameters (refer to fig. 6.3 and Table 6.1) using the method described in Section 6.3.1. For the age-dependent study (data set 2), they were calculated using Koretz *et al.*'s [106–109] original fits (see Table 6.2).

2. Calculation of the net radius of curvature gradient, g (fig. 6.5)

3. Implementation of the GRINCU model, using the geometrical parameters and curvature gradients obtained in points 1 and 2. The changes in the GRINCU lens geometry are displayed in a video, available in Lockett-Ruiz *et al.*'s online publication [4]. See fig. 6.4 for a screenshot of the accommodated state.

4. With the lens geometry and refractive index distribution obtained in point 3, we were able to compute:
   - The paraxial lens power and equivalent power (fig. 6.6)
   - The equivalent refractive index of a two-surface homogeneous lens (fig. 6.7)
   - The equivalent refractive power of a four-surface lens (fig. 6.8) with a homogeneous cortex and a homogeneous nucleus.

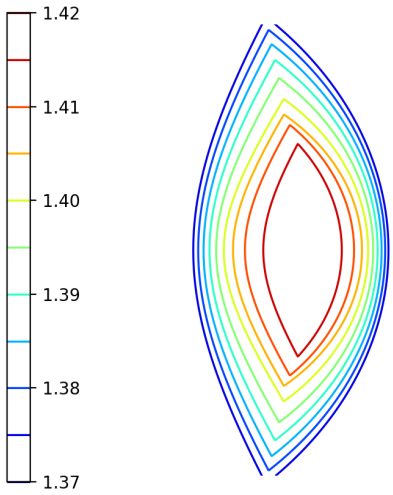

Figure 6.4: Accommodating iso-indicial surface (IIS) contours frame from Movie 1 in Ref. [4]

6.5.1 Lens Geometry

All accommodation cases showed similar trends in terms of lens geometry. The lens external and nucleus surface radii of curvature decreased with accommodation, the anterior surface undergoing the most change (fig. 6.3a). The nucleus axial thickness increased the most compared with the anterior and posterior cortex thicknesses (fig. 6.3b). Figure 6.5 displays the change in net curvature gradient for both datasets. The solid line represents the anterior region of the lens, and the dashed the posterior. The net gradient g decreased in magnitude roughly linearly for all datasets and ages considered. In general, the anterior gradient varied the most, which can be explained by the significant radius of curvature decrease of the anterior lens surface and the almost negligible change in cortex thickness (see eq. (6.1)). This asymmetry is the reason for the different shifts in g between the front and back surfaces of the lens seen in figs. 6.5a and 6.5b.

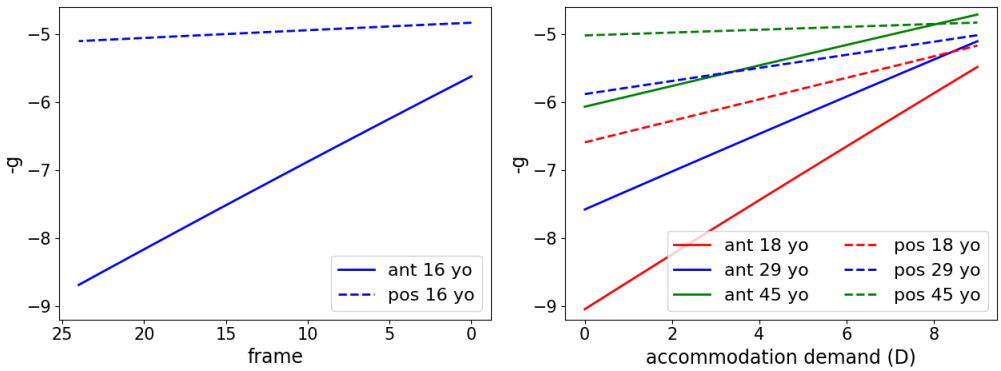

(a) 16-year-old lens.

(b) Age-dependent study.

Figure 6.5: Anterior (solid) and posterior (dashed) cortex net radius of curvature gradient as a function of accommodation.

6.5.2 Refractive Power

Figures 6.6 and 6.7 present the primary findings of this study. The refractive power increased consistently (fig. 6.6), showing a nearly quadratic trend in response to accommodation demand across all datasets. The GRINCU model predicted a total change in lens power from the unaccommodated to fully accommodated state (solid lines) that varied from 9.64 D for the 16-year-old subject in the experimental video (fig. 6.6a) to 5.86 D for the 45-year-old participant in the age-related accommodation study (fig. 6.6b). The dashed lines in fig. 6.6 illustrate the power of a two-surface homogeneous lens model, computed with a constant equivalent refractive index calculated for the unaccommodated state of the lens (eq. (6.4)). According to Gullstrand's definition, a positive IAM occurs when the GRIN lens power increases more during accommodation than that of its equivalent homogeneous lens. For all ages considered in this study, the GRINCU lens's refractive power was greater than the homogeneous lens's refractive power, thereby confirming a positive IAM. Figure 6.6b suggests that the IAM increases with age, which is supported by the increasing slope with age displayed in fig. 6.7b.

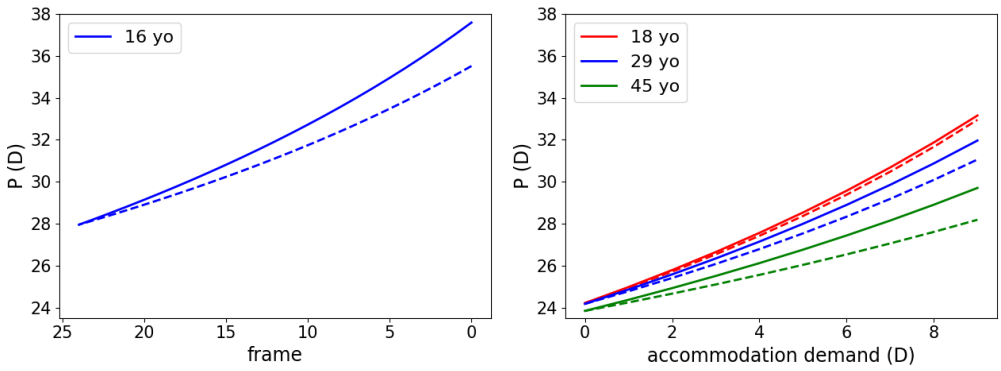

(a) 16-year-old lens. **(b)** Age-dependent study.

Figure 6.6: Accommodative refractive power of the GRINCU lens (solid), compared with the equivalent power of a two-surface homogeneous lens (dashed).

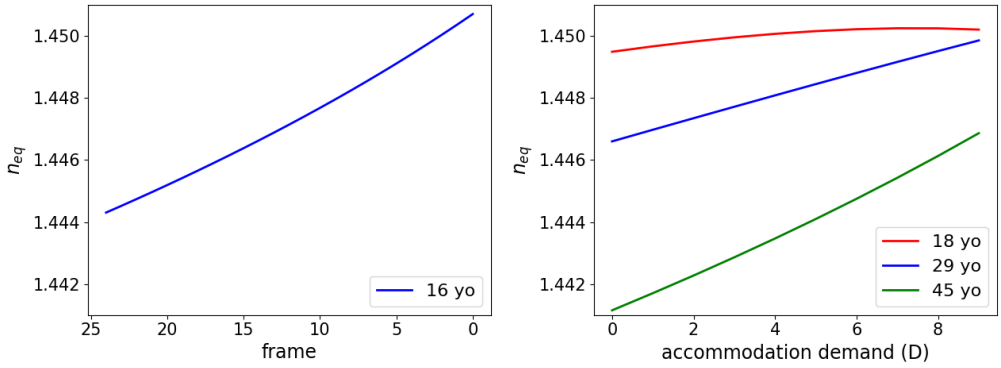

(a) 16-year-old lens. **(b)** Age-dependent study.

Figure 6.7: Equivalent refractive index at all accommodative states.

The four-surface model's power closely matched the GRINCU in the experimental video data analysis (fig. 6.8a), indicating that the four-surface and GRINCU models might be equivalent. However, the results for the experimental age-dependent fits (fig. 6.8b) differed significantly, as the four-surface model indicated a positive IAM that decreased with age.

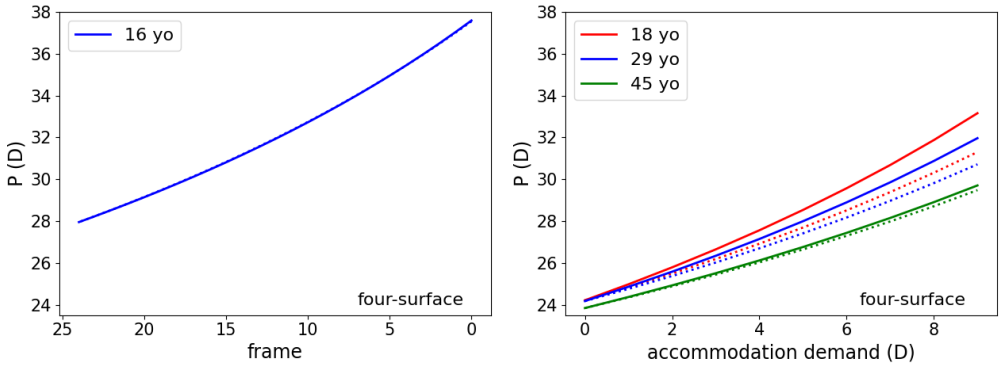

(a) 16-year-old lens.

(b) Age-dependent study.

Figure 6.8: Accommodative refractive power of the GRINCU lens (solid), compared with the equivalent power of a four-surface lens (dotted) with a homogeneous cortex and homogeneous nucleus.

6.5.3 Refractive Power at Zero Curvature Gradient

Figure 6.9 illustrates how the absence of a radius of curvature gradient (g) affects the intracapsular accommodation mechanism (IAM). When $g = 0$, the IAM is minimal, and the power of the homogeneous two-surface lens model closely aligns with that of the GRINCU lens. In this scenario, nearly the entire power increase is attributed to changes in surface curvature, with the GRIN contribution being negligible. It is worth noting that both the lens power and the power increase during accommodation are relatively low—ranging from 18 D in the unaccommodated state to 23 D when accommodated (+5 D)–compared with the results shown in fig. 6.6, which range from approximately 24 D to 33 D (+9 D)–. Therefore, to account for both the lens power and the total power increase during accommodation, it is essential to consider not only the changes in surface curvatures but also the gradient of the inner shells' radius of curvature. These findings support our parting hypothesis that links the IAM to the changes in the radius of curvature gradient during accommodation.

6.6 DISCUSSION

Table 6.3 builds upon Table 1.1 in Section 1.2.2, comparing the lens refractive power and equivalent refractive index changes between the unaccommodated and fully accommodated states observed in this study. It is important to note the distinct nature of the data in the first row (a 16-year-old's lens), which pertains to an individual case, versus the last three rows, which represent

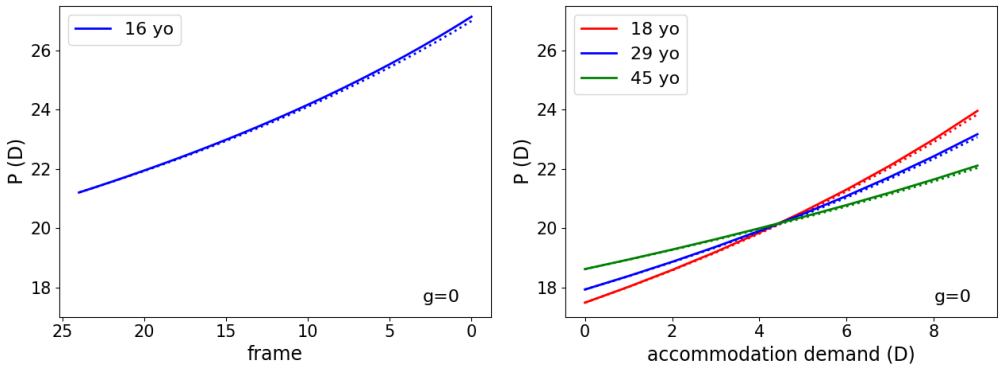

(a) 16-year-old lens. **(b)** Age-dependent study.

Figure 6.9: Accommodative refractive power of the GRINCU lens with no curvature gradient ($g = 0$) (solid), compared with a homogeneous lens (dotted).

average trends from a cohort of 100 eyes. When comparing different lens models, it becomes evident that the most significant increases in equivalent refractive index are associated with simplified lens models featuring two or four surfaces, unlike the more realistic GRIN or GRINCU models. Exceptions include the Le Grand eye model [35] and the findings of Hermans *et al.* [41], which considered accommodation lag and showed less change in lens power than the two or four-surface models. The difference between the variation in target vergence and the actual change in the accommodation response, known as the accommodative lag, could be crucial for studying the IAM's effect [41]. Table 6.3 shows that all models exhibited a positive IAM. Interestingly, the IAM value for the 16-year-old individual [105] (data set 1) was higher than for the 18-year-old from data set 2, despite their similar ages. This discrepancy may be attributed to individual variations (data set 1) compared to average trends (data set 2). Nonetheless, in all cases, the GRINCU model indicated a positive IAM for all ages. However, the accommodation change due to the lens's GRIN structure was not as pronounced as suggested by Gullstrand.

The results listed in Table 6.3 suggest that the IAM's contribution to the total accommodation response is less than one-third across all cases studied, with the highest contribution being 26% in the 45-year-old lens–lower than Gullstrand's calculation–. This modest contribution may seem to contradict other results, particularly for non-human primates [40], which suggested that the GRIN structure in the lens accounts for two-thirds of the total accommodation. However, there is no contradiction since the above-referenced study defines the GRIN contribution to lens power (P_G) as the difference between the total power (P) and the power contributed by the anterior and posterior surfaces ($P_G = P - P_S$). To determine the GRIN's effect on accommodation, the authors calculated the power increase due solely to the GRIN structure. Given that P is linear with P_S and P_G (eq. (6.2)), it is straightforward to derive the increase in the GRIN contribution in terms of surface and total power increases:

$$\Delta P_G = \Delta P - \Delta P_S \tag{6.5}$$

Table 6.3: Intracapsular accommodation mechanism findings across different accommodating studies and lens models, updated.

AUTHOR	MODEL	RELAXED		ACCOMMODATED		VARIATION	IAM
		P(D)	n_{eq}	P(D)	n_{eq}	$\frac{\Delta n_{eq}}{\Delta P}$ (10^{-3})	
Gullstrand [35]	4 surf.	19.11	1.4085	33.06	1.4260	1.25	+
Le Grand [35]	2 surf.	21.78	1.4200	30.70	1.4270	0.78	+
Navarro [36]	2 surf.	21.55	1.42	34.30	1.438	1.41	+
Hermans [41]	4 surf.	–	1.4345	–	1.4345	0	No
Garner [42]	GRIN	21.75	1.4277	30.65	1.4277	0	No
GRINCU, 16yo[a]	GRIN	27.95	1.4443	37.59	1.4507	0.66	+
GRINCU, 18yo[b]	GRIN	24.21	1.4495	33.16	1.4502	0.08	+
GRINCU, 29yo[b]	GRIN	24.17	1.4466	31.96	1.4499	0.42	+
GRINCU, 45yo[b]	GRIN	23.84	1.4412	29.70	1.4469	0.97	+

[a] Data set 1 (one eye)
[b] Data set 2 (100-eyes average trend)

Table 6.4: Accommodated and unaccommodated power ratios.

	16 yo[a]	18 yo[b]	29 yo[b]	45 yo[b]
P_G/P unaccommodated	68.30%	69.81%	69.00%	67.36%
$\Delta P_G/\Delta P$	74.44%	69.89%	72.01%	75.27%
IAM sign	+	+	+	+

[a] Data set 1 (one eye)
[b] Data set 2 (100-eyes average trend)

Where ΔP represents the change in the lens's total power, ΔP_S denotes the change in surface power, and ΔP_G indicates the change in power contributed by the GRIN structure. Our model forecasts unaccommodated ratios of P_G/P between 67% and 70% (refer to Table 6.4), aligning with the relative contributions reported by Hermans *et al.* [41]. Although the GRIN structure significantly contributes to accommodation, this alone does not ensure an increase in the equivalent refractive index or a positive IAM. Comparing Tables 6.3 and 6.4, one can see that the more the GRIN contributed to accommodation, as compared with the unaccommodated state, the greater the IAM observed. The present findings imply that a positive IAM requires that $\Delta P_G/\Delta P > P_G/P$, which would imply an increase in the equivalent refractive index. Indeed, the same authors observed a strong influence of the GRIN on the accommodation response [40], with no change in the lens's equivalent index during accommodation (IAM $= 0$).

What is new in the GRINCU model is that it provides an explicit quantitative explanation of the contribution of the inner lens shells' radius of curvature to the refractive power. Equation (6.2) indicates that the GRIN contribution to the power is additive and comprises the sum of each shell's contribution to the power. This contribution was proportional to the gradient index derivative n'

and the shell curvature (1/R), meaning that both the GRIN and inner curvature are equally important and have a common multiplicative effect [39]. The power contributed by each (differential) layer was similar to the power of a standard lens surface. The increase in lens power with accommodation results from the changes in index distribution and lens geometry. The only change in the index distribution with accommodation was the stretching of the index profile as the lens thickened (eq. (2.17)), which predicts a slight decrease in n' and, hence, a small reduction in lens power (integrand in eq. (6.2)). However, R and g vary greatly with accommodation, so the increase in lens power must be mainly due to the change of these two parameters (anterior and posterior).

7 AGING AND THE LENS PARADOX

7.1 THE LENS PARADOX

The lens paradox is the phenomenon by which the human crystalline lens loses refractive power with age despite the increase in external curvature and lens thickening associated with aging. In other words, it is the maintenance of emmetropia or the increase in hypermetropia with age (hypermetropic shift) despite the increase in the curvature of the lens. The steepening of the external surface curvatures would be expected to boost the effective lens power and thus produce a myopic shift. However, the opposite is observed, and the aging eye progresses towards hyperopia.

Brown first described the lens paradox in the 1970s [115]. He introduced Scheimpflug photography in ophthalmology and showed that the anterior lens surface becomes steeper with age, contrary to the prevailing theories of the time [116]. Initially, it was suggested that either a reduction in lens thickness [117] or changes in the refractive index difference between the lens nucleus and cortex might explain this paradox [118]. During youth, the nucleus has a higher refractive index than the cortex, and it was hypothesized that this might reverse with aging. On the one hand, an increase in the cortex refractive index would be explained based on increased light scatter [119]. On the other, a decrease in nuclear refractive index could be explained by a reduction in protein concentration [120]. However, considering the lens biochemistry, we can assume that the refractive indices at the lens's edge and center remain unchanged with age. Koretz and Handelman [121] demonstrated that internal changes in the lens must occur alongside external ones. They also proposed that for the eye to maintain focus as the lens changes shape with age, the equivalent refractive index of the lens should diminish over time. Dubbelman and Van der Heijde [122] supported this hypothesis by showing through cross-sectional data that the lens's equivalent refractive index indeed decreases with age in adults, thus (qualitatively) explaining the lens paradox. Pierscionek [123] proposed that a slight change in the eye's lens cortex's refractive index slope could counteract the lens curvature increase and prevent age-related myopia. Smith and Pierscionek [124] further examined this concept using a GRIN lens model with an elliptical iso-indicial surface distribution and found that the decrease in lens power is linked to a gradual steepening of the refractive index profile in the lens cortex.

While these explanations became increasingly realistic over time, they remained mainly qualitative. There is a need for a realistic, quantitative model of the aging lens that can effectively address the lens paradox by accurately predicting the age-related changes in the lens. One of the more recent attempts (Navarro, 2014) indicated that even an adaptive GRIN model fell short in this regard. We suggest that a thorough and accurate explanation requires mod-

ifications not only in the GRIN but also in the GRCU as the lens undergoes aging.

This chapter aims to model how the GRINCU changes with age. Specifically, we will analyze the variations in the curvature gradient over time and determine how the curvature gradient parameter G correlates with age. To do so, the GRINCU model will be fitted to experimental lens data, and the parameter G will be optimized to align with changes in lens power attributed to age.

7.2 THE AGING CRYSTALLINE LENS

To assess the effect of the curvature gradient on the decline in lens power with age, we depart from experimental data on both the optical performance of the crystalline lens [125] and its geometry and structure [19, 38, 126–128]. This approach enables us to refine the aging model by using the curvature radius gradient parameter as the only free variable.

7.2.1 Aging Lens Data

The lens power data used in this study corresponds to 1069 healthy right eyes of White Western European individuals, with 54.2% being women. The average age of the participants was 44.2 ± 14.2 years, and their ages ranged from 20 to 85 years. Eye biometrics were measured without cycloplegia to reflect their normal physiological state as closely as possible. The participants had a spherical equivalent of -0.84 ± 2.16 diopters (D). Data was collected between 2011 and 2013 across nine centers in six European countries. The collected parameters were organized into 5-year age bins, with averages and standard deviations calculated for each interval. For simplicity in calculations, the midpoint of each age bin was used in our analysis. Table 7.1 displays the lens powers from the reference and the age values used in the present Chapter.

Table 7.1: Distribution of lens power by age for the entire cohort.

Age range (yr)	Age value (yr)	Power (D)	Standard dev. (D)
< 25	23	26.17	2.10
$25 - 29$	28	25.88	1.98
$30 - 34$	33	25.76	2.07
$35 - 39$	38	25.39	1.84
$40 - 44$	43	25.06	2.17
$45 - 49$	48	25.17	1.89
$50 - 54$	53	24.65	1.68
$55 - 59$	58	23.98	2.10
$60 - 64$	63	23.64	1.93
$65 - 69$	68	23.29	2.02
$\geqslant 70$	73	22.51	1.68

7.2.2 Refractive Index

The literature has two main perspectives regarding the variability of lens nucleus and surface refractive index with age. Many studies suggest that these indices remain roughly unchanged as we age [19, 26, 27, 123, 129], while some indicate a slight decrease in the core refractive index over time [21, 73, 130, 131]. In the present Chapter, we use constant values for $n_c = 1.4181$ and $n_s = 1.3709$, as calculated by Jones et al. [19].

The refractive index distribution within the lens adheres to a power law characterized by the p-coefficient, which dictates the steepness of the gradient [19, 27, 59, 66, 82, 83, 132]. Lower p-coefficient values, indicative of curved profiles, are typically found in younger lenses. In contrast, higher p-coefficient values, associated with profiles featuring a broader central plateau and a steep gradient at the equatorial periphery, are observed in older lenses [19]. Increased p-coefficient values and a broader plateau also reduce the gradient index power [59]. The age-dependent p-coefficient applied in this Chapter is from Navarro et al.'s work [133], calculated as below with a in years:

$$p = 2.85 + 1.11 \times 10^{-7} \times a^4 \tag{7.1}$$

7.2.3 Lens Geometry

To properly optimize the model, it is essential to incorporate precise changes in lens geometry due to aging. We will apply two age-dependent geometrical models to compare and understand the interaction between the internal and external geometry of the lens—specifically, the curvature gradient and the lens's outer shape. The first set of age-dependent geometrical variables comes from Norrby's 2005 analysis [128] of Dubbelman's eye model [122, 127], compiled in Navarro's 2014 work [38]. Dubbelman's equations for lens radii of curvature and lens thickness (eqs. (7.2a) to (7.2c)) are linear regressions based on the in-vivo Scheimpflug imaging of the right eye of 102 healthy subjects aged between 16 and 65 years.

$$R_{as} = 12.7 - 0.058 \cdot a \tag{7.2a}$$

$$R_{ps} = -5.9 + 0.013 \cdot a \tag{7.2b}$$

$$t = 2.93 + 0.0236 \cdot a \tag{7.2c}$$

The second set of variables corresponds to Rozema's more recent Perpetual Eye Model [134]. The Perpetual model is based on a series of previously published bi-exponential regressions that relate ocular biometry and refractive error to age, drawing from 294 studies in the literature. The author graciously provided us with a file containing the age-related data, which includes 62 values for lens radius of curvature and thickness for ages 19 to 80 years. We determined that the best fit for the anterior and posterior lens radii of curvature was a 4th-degree polynomial (eqs. (7.3a) and (7.3b)), with R^2 values of 1 and

0.9995, respectively. The lens thickness was best represented by a linear trend (eq. (7.3c)) with an R^2 value of 0.9996.

$$\begin{aligned} R_{as} =& 11.291 + 0.0366 \cdot a - 0.0022 \cdot a^2 \\ &+ 2 \times 10^{-5} \cdot a^3 - 10^{-7} \cdot a^4 \end{aligned} \tag{7.3a}$$

$$\begin{aligned} R_{ps} =& -5.9328 - 0.0284 \cdot a + 0.0007 \cdot a^2 \\ &- 8 \times 10^{-6} \cdot a^3 + 3 \times 10^{-8} \cdot a^4 \end{aligned} \tag{7.3b}$$

$$t = 3.0683 + 0.0243 \cdot a \tag{7.3c}$$

For both implementations, the conic constants were maintained as age-independent, with values set at $Q_a = -4$ and $Q_p = -3$ [126], corresponding to hyperbolas. The anterior and posterior thickness ratio relative to the total thickness was maintained at 60% and 40%, respectively.

7.2.4 Model Optimization

Once the two lens external geometries are established, we proceed to implement the GRINCU lens model for all ages, adjusting the curvature gradient parameter (G) to align the lens power with the selected reference [125] (refer to Table 7.1 for the aging lens data).

In the GRINCU model, the lens power is the sum of the surface power and the power contributed by the GRIN structure (eq. (3.14)). This GRIN power is computed as an integral (eq. (3.15)) of the derivative of the refractive index in the z-axis, $n'(z)$, divided by the product of the refractive index, $n(z)$, and the iso-indicial surface apical radius of curvature, $R(z)$, which in our case results in Equation (3.17) below. (Refer to Chapter 2 for the formulation of the model and Chapter 3 for a detailed explanation of the lens power calculation.)

$$\begin{aligned} \phi_G =& -\frac{n_s p \delta n}{t_a} \int_0^{t_a} \frac{(1 - z/t_a)^{p-1}\, dz}{[n_c + \delta n\,(1 - z/t_a)^p]\,(R_{as} - g_a z)} \\ &+ \frac{n_s p \delta n}{t_p} \int_{t_a}^{t} \frac{((z - t_a)/t_p)^{p-1}\, dz}{[n_c + \delta n\,((z - t_a)/t_p)^p]\,(R_{ps} - g_p (z - t))} \end{aligned}$$

The net curvature gradients in the lens's anterior and posterior regions are determined by the curvature gradient parameter and the external surface conic constants, expressed as $g_a = G_a(Q_a + 1)$ for the anterior and $g_p = G_p(Q_p + 1)$ for the posterior. This Chapter adopts the most straightforward mathematical approach by setting an equal G value for the anterior and posterior lens regions ($G = G_a = G_p$). Note that because Q_a and Q_p are different, this single G value will result in distinct curvature profiles for the anterior and posterior regions. The equations for the IIS radii of curvature in the anterior and posterior regions are given by eqs. (2.8a) and (2.8b):

$$\begin{aligned} R_a(z_0) &= R_{as} - G_a(Q_a + 1) z_0 = R_{as} - g_a z_0 \\ R_p(z_0) &= R_{ps} - G_p(Q_p + 1)(z_0 - t) = R_{ps} - g_p (z_0 - t) \end{aligned}$$

To ensure the iso-indicial radii of curvature do not reach zero or change signs near the lens center, we set limits for $R_a(z)$ and $R_p(z)$ at 10% of their values at

the lens surface. In other words, if $R_a(z)$ or $R_p(z)$ reach the minimum limits as the radius of curvature decreases towards the lens center, we guarantee that the innermost iso-indicial surfaces maintain a constant radius of curvature equal to $R_{as}/10$ and $R_{ps}/10$.

Lens power for all ages in both geometries was computed by numerical integration using the trapezoidal rule. By adjusting G manually, we matched the calculated lens power to the data trendline with a precision of two decimal points. These age-fitted G values were then fit to a 4th-degree polynomial with age as the independent variable (see fig. 7.2). We also tried a linear and a quadratic fit, but the 4th-degree polynomial was the most accurate.

To better assess the effect of the curvature gradient on the lens power in comparison with the absence of a gradient, we also computed the lens power with a gradient parameter of $G = 1$, corresponding to a concentric iso-indicial surface configuration (see Section 2.1.1). Figure 7.1 shows the experimental data trendline, together with the adjusted G lens power values and the lens power calculated with $G = 1$ and the same geometry.

For both $G = 1$ and our age-fitted G values, we also calculated the equivalent refractive index to analyze its change with age (fig. 7.4) and see whether it aligns with the findings in the literature.

7.3 RESULTS

The initial stage in optimizing the aging GRINCU lens model entailed the following steps:

1. Fit the experimental average lens power values to a quadratic trend as a function of age.
2. Implement two distinct age-dependent lens geometries to model the GRINCU lens (refer to Section 2.3 for details).
3. Adjust the gradient parameter (G) at each age to correspond with the calculated trend from the reference [125].
4. Compute the lens power using a concentric configuration of the IIS (with $G = 1$) for the same ages and lens geometries applied in the previous steps. This is used mainly as a reference for comparison purposes.

The outcomes of this optimization are illustrated in fig. 7.1. Based on the lens power and G values obtained, we were able to:

5. Fit the G values obtained for each geometry to a polynomial function that varies with age (fig. 7.2).
6. Compute the equivalent refractive index for both the age-dependent G values and $G = 1$ (fig. 7.4).

7.3.1 Lens Power

Figures 7.1a and 7.1b display the lens power results. The black stars represent the experimental data, the dashed black line indicates the quadratic fit,

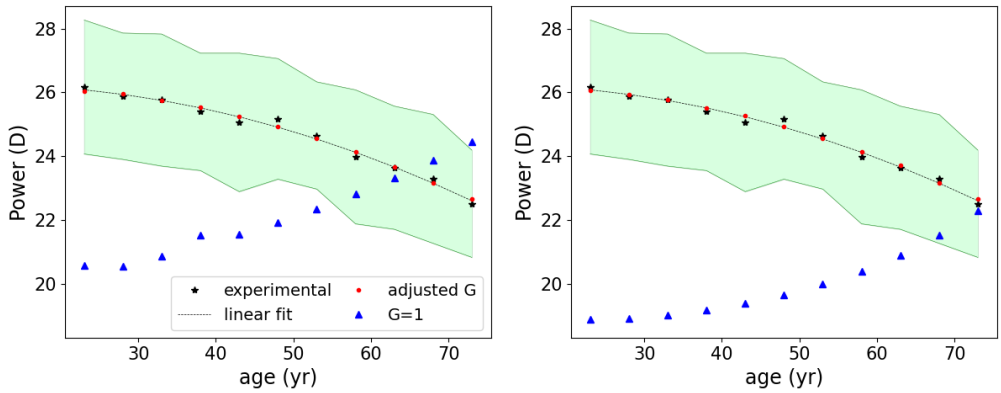

(a) Dubbelman's Eye Model **(b)** Perpetual Eye Model

Figure 7.1: Lens power trends with age.

$P(a) = 26.1537 + 0.0177 \cdot a - 0.0009 \cdot a^2$, and the green shaded area shows the standard deviation as referenced in Jongenelen et al. [125]. The red dots show the GRINCU lens powers obtained by adjusting the curvature gradient parameter G, while the blue triangles indicate the lens powers calculated using the same lens geometry with a constant curvature gradient parameter $G = 1$, representing a concentric configuration of the IIS. Comparatively, with the same curvature gradient ($G = 1$), the GRINCU lens geometry implemented using Dubbelman's parameters (fig. 7.1a) resulted in higher powers across all ages than the Perpetual model (fig. 7.1b). Nonetheless, both demonstrate an increasing trend in lens power with age, suggesting that the curvature gradient must change with aging in order for the lens power to decrease.

7.3.2 Curvature Gradient

The implementation of the two geometrical models showed an upward trend in the curvature gradient parameter (G), moving from more negative to more positive values (see fig. 7.2). This change was more pronounced with Dubbelman's parameters (fig. 7.2a) than with Rozemas's Perpetual model (fig. 7.2b). The trend in G was best described by a 4th-degree polynomial (fit equations displayed in fig. 7.2). In both cases, the curvature gradient parameter changes gradually and almost linearly between 23 and 53, then steepens significantly from 53 to 73 years old. This steepening that starts in the fifties suggests that internal lens changes accelerate during these years compared to earlier stages of life. The curvature gradient parameter changes signs in both geometries, occurring later in life in the Perpetual model (after 68) than in Dubbelman's model (before 58). Considering that $(Q_a + 1)$ and $(Q_p + 1)$ are both negative, negative values of G lead to positive values of g_a and g_p, meaning the radii of the iso-indicial surfaces decrease towards the center. Conversely, if G is positive, the net gradient is negative, causing the radius of curvature to increase from the surface to the lens center. In young lenses, the iso-indicial surfaces exhibit more curvature near the lens core compared with those closer to the surface, displaying a significant difference in curvature. As lenses mature, the

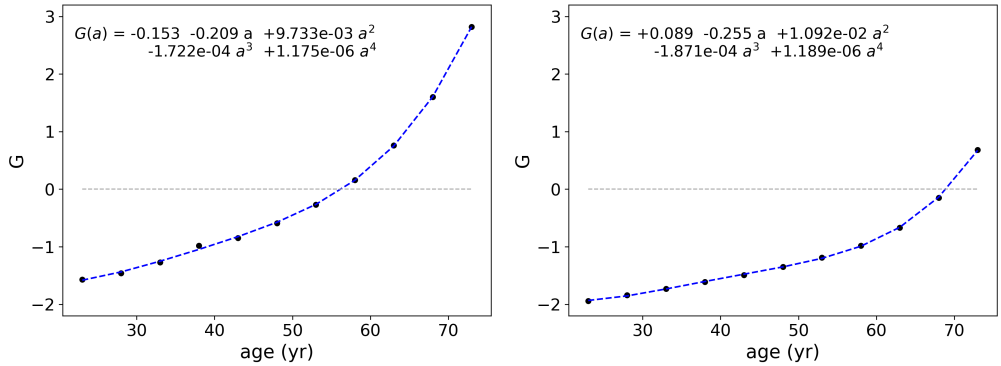

(a) Dubbelman's Eye Model **(b)** Perpetual Eye Model

Figure 7.2: Curvature gradient parameter G dependence on age.

difference in curvature between the superficial and deeper iso-indicial surfaces diminishes, eventually reaching a point where they are parallel (when $G = 0$). In older lenses, the iso-indicial surfaces near the core are flatter than those near the surface. This effect is more pronounced in the lenses implemented using Dubbelman's geometry than in those implemented using Rozema's Perpetual model. Figure 7.3 below illustrates the iso-indicial profile distribution for various ages within the range, modeled using both geometries. The change in curvature gradient of the isoindicial surfaces is evident in the age range shown.

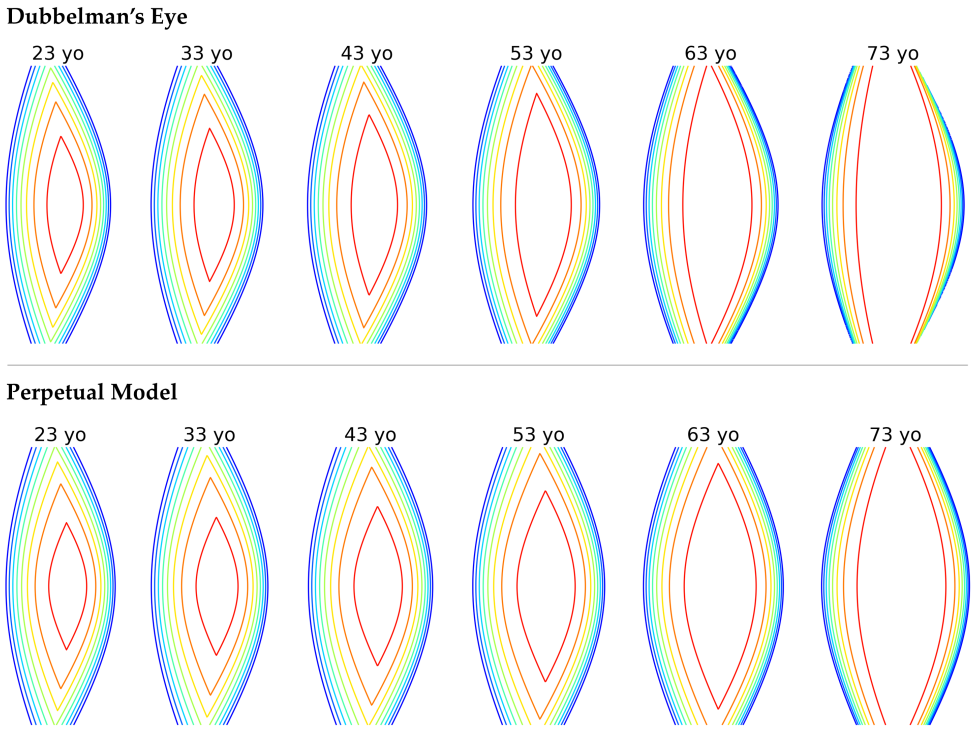

Figure 7.3: Sagittal lens section showing the iso-indicial surface distribution for each age and geometry.

The concentric case (G = 1) is only observed at a relatively advanced age. In the lens modeled with Dubbelman's geometry, this typically occurs around 58 years old, while in Rozema's Perpetual model, it happens around 70. Therefore, the concentric case examined in most previous models is not common; instead, it seems to appear only for a relatively brief period in older lenses.

7.3.3 Equivalent Refractive Index

Figure 7.4 shows the equivalent refractive index determined for two scenarios: one where the curvature gradient parameter changes with age (indicated by the red solid-dot line) and another with a constant curvature gradient parameter, G = 1, representing a concentric configuration of the IIS (depicted by the blue dash-dot line). For the varying curvature gradient, the equivalent refractive index decreases with aging. The Perpetual eye model yields refractive index values roughly 0.008 higher than the Dubbelman eye overall, but interestingly, both show a decrease of around 0.027 in the examined age range. Meanwhile, when G = 1, the equivalent refractive index remains relatively stable with age, and both geometrical models exhibit similar trends, with a change with age of less than 0.001. This suggests that the main age-related change in the lens's inner structure is not the GRIN but the GRCU.

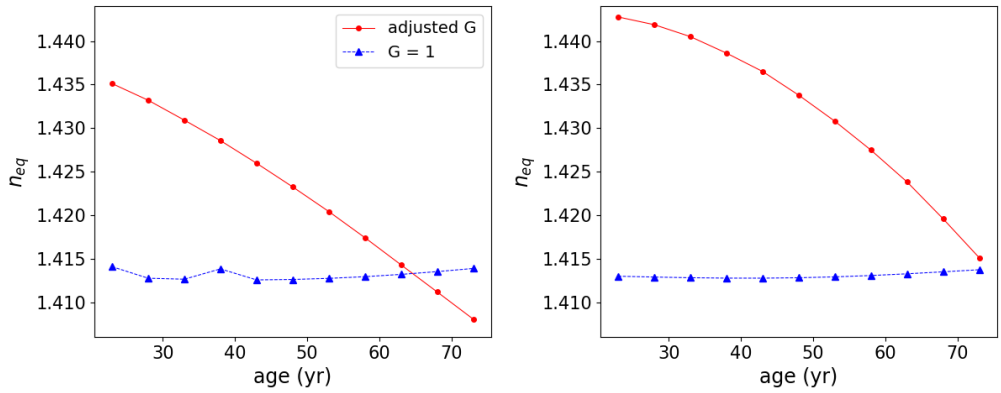

(a) Dubbelman's Eye Model **(b)** Perpetual Eye Model

Figure 7.4: Curvature gradient parameter G dependence on age.

7.4 DISCUSSION

The lens paradox has been confirmed by several researchers in the past, with a consensus that changes in the refractive index profile of the lens can prevent an aging lens from becoming myopic [39, 64, 89, 98, 122, 135, 136]. Smith et al [135] also reported that maintaining a constant refractive index profile throughout life would lead to increased lens power. In this chapter, the refractive index profile changes with age according to the age-dependent exponent p (). This power law flattens the axial refractive index profile over time, resulting in a decrease in the power contributed by the GRIN structure [98]. However, this

decrease in the GRIN contribution alone does not explain the lens paradox. In fact, our results suggest that even considering the changes in refractive index distribution, a concentric configuration of the IIS ($G = 1$) causes an increase in lens power with age. An age-dependent curvature gradient (GRCU) is necessary to explain the lens paradox, as suggested in previous studies [39].

In their 2001 in-vivo study, Dubbelman and van der Heide [126] investigated the lens paradox by assessing the lens's equivalent refractive index. They reported a decline of 0.018 between the ages of 20 and 65, a value significantly lower than Brown's findings, which indicated a decrease of approximately 0.025 in the same age range. Our computational results using the GRINCU model are more in line with Brown's, showing a decline of roughly 0.027 in the equivalent refractive index between the ages of 23 and 73. However, it appears that the decline in the equivalent refractive index accelerates slightly with age. If we analyze an age range of 23 to 63, which is more comparable to Dubbelman's study, the decrease in equivalent refractive index is recorded at 0.021 for Dubbelman's geometry and 0.019 for the Perpetual Eye model, making these values more aligned with their findings. Furthermore, our results may be affected by the selection of refractive indices for the lens core and surface, the age-dependent lens geometries, or a combination of both factors.

Giovanzana et al. [89] analyzed the lens paradox using the ABCD matrix formalism applied to a four-surface lens model. They reported that a homogeneous index of refraction for a lens with age-dependent geometry resulted in an increase in lens power of 1.63D between the ages of 20 and 70. To counteract the eye's increasing refractive power with age, they determined that the radius of curvature of the nucleus must increase. In younger lenses, the curvature of the nucleus was steeper than that of both external surfaces, whereas in older lenses, the nucleus became flatter than the posterior surface. Our findings corroborate their results, demonstrating a positive curvature gradient in younger lenses that flattens with age until it changes sign in the 50s according to Dubbelman's geometry, or around age 70 in Rozema's model, and gradually transitions to a negative gradient in the older years. The steepness of this gradient and its progression with age are significantly influenced by the choice of refractive indices for the lens surface and core, as well as the aging lens geometry. This aligns with Giovanzana et al.'s observations, which indicated that a higher central refractive index necessitates a greater radius of curvature of the nucleus to achieve the same optical power. Interestingly, the four-surface lens model can explain the lens paradox, whereas the standard concentric GRIN model cannot. This is because the four-surface lens model accounts for changes in the curvature gradient (the difference in curvature between the cortex and nucleus surfaces) with age. For future work, it may be worthwhile to explore whether a four-surface lens model with age-dependent refractive indices for the cortex and nucleus can serve as a reasonable approximation of the GRINCU lens.

DISCUSSION

8 CONCLUSIONS

8.1 ACHIEVEMENTS

- An enhanced formulation of Navarro's 2021 GRINCU crystalline lens model was implemented, with iso-indicial surfaces parameterized by the lens's external radii of curvature and conic constants rather than conic semiaxes and epsilon values. New configurations for paraboloid iso-indicial surfaces were also introduced, which were absent in the previous version of the model. Numerical implementations were developed for both rotationally symmetric and general astigmatic lens models, and chromatic dispersion was also included.

- A custom ray transfer matrix was created for onion-shaped GRIN lenses by applying a differential approximation to the matrix product of a large number of layers. An expression for the overall power of the GRIN lens was derived from the ray transfer matrix. The correctness and accuracy of this expression were verified by comparing the resulting lens power with that obtained from the direct matrix product. Finally, an analytical solution specifically for the crystalline lens was obtained, yielding precise results as well.

- Both finite and paraxial ray tracing for the GRINCU model was conducted in two different software applications: Zemax (commercial) and RTLib (public), a custom ray-tracing library for Matlab. User-defined surfaces were created for both singlet and doublet configurations, followed by ray tracing to determine the lens power, cardinal points, and aberrations. Cross-validation tests were conducted between the two programs and the singlet and doublet configurations to verify the accuracy of the results.

- The GRINCU lens model was implemented into SyntEyes [2], a synthetic biometric data database that closely mimics real biometric data from the population. This data included corneal and lens curvatures and thicknesses, anterior chamber and vitreous depth, and the refractive power of both the lens and cornea, as well as the overall eye. Using ray tracing in RTLib, the optical properties were obtained for various curvature gradients of the GRINCU lens alongside a homogeneous lens model. The outcomes were compared in order to evaluate the gradient-index model against the homogeneous lens and to examine how different curvature gradient configurations affect the eye's optical properties.

- An accommodation model of the GRINCU lens was implemented based on experimental data from the literature. Gullstrand's intracapsular accommodation mechanism (IAM) was evaluated by analyzing the observed

changes in the lens's inner curvature gradient with accommodation in different age groups. The refractive index distribution, refractive power, and equivalent refractive indices were calculated at various accommodative states for two sources in the literature. The IAM's contribution to accommodative power was determined for a 16-year-old lens in one source and for ages 18, 29, and 45 in the other.

- Empirical data from aging lenses were utilized to incorporate age-related changes, such as lens growth and variations in the refractive index distribution, into the GRINCU model. The curvature gradient of the GRINCU lens was configured so that the lens power would match experimentally measured values for individuals aged 23 to 73. Curvature gradient and equivalent refractive index as a function of age were computed for two different aging lens geometries to provide a quantitative explanation of the lens paradox.

8.2 CONCLUSIONS

1. The ray transfer matrix for onion-type continuous GRIN lens media resembles that of a single layer but with the matrix elements A, B, C, and D substituted by their respective integrals. This allows for cost-effective and straightforward calculations of the optical system's power. The integrals for elements A, B, and D are zero; therefore, the GRIN media ray transfer matrix is a single-element (C) matrix $\mathcal{G}$.

2. The lens ray transfer matrix can be expressed as the sum $L = H + \mathcal{G}$, where H represents the ray transfer matrix of a standard homogeneous lens with a refractive index equal to that of the lens surface, and $\mathcal{G}$ encapsulates the contribution of the GRIN inner structure.

3. In meniscus lenses with identical curvature radii of the anterior and posterior surfaces, the absence of a curvature gradient results in zero contribution of the GRIN to the lens's refractive power. Conversely, in biconvex lenses, where the anterior and posterior curvatures have opposite signs, the GRIN does contribute to the refractive power. The expression of this power is analogous to the power of a thin lens in air, with the refractive indices replaced by their logarithms.

4. The radius of curvature gradient, G, and the conic constant, Q, significantly influence the power of crystalline lens models. More negative Q values result in lower lens power compared to more positive values. Conversely, more negative curvature gradient parameters lead to increased lens power.

5. Different implementations of finite ray tracing through GRINCU lenses–whether in custom software like MATLAB or commercial platforms like ZEMAX, as well as in singlet or doublet configurations–yielded equivalent results in both lens power and aberrations, indicating a cross-validation of these methods.

6. An iso-indicial curvature gradient induces a displacement in the principal planes in a GRINCU lens relative to those of a homogeneous lens of the same external geometry and power. A positive gradient ($g > 0$) shifts the principal planes towards the front of the lens, while a negative gradient ($g < 0$) shifts them towards the back of the lens.

7. In eyes with identical geometry, a positive curvature gradient of the lens's IIS results in increased ocular power. A positive curvature gradient also increases vertical coma while decreasing astigmatism, lateral coma, and spherical aberration.

8. The contribution of the intracapsular accommodation mechanism (IAM) to the increase in power during accommodation is significantly lower than that predicted by Gullstrand, particularly for younger lenses.

9. The gradient radii of curvature of the inner surfaces of the lens contribute to the refractive power change during accommodation, having a multiplicative effect with the change in refractive index distribution.

10. For lens models with gradient refractive index (GRIN) and radius of curvature (GRCU), the intracapsular accommodation mechanism is positive and increases between 18 and 45 years of age. This age-related increase might partially offset the decline in accommodation response associated with aging.

11. Using experimentally measured lens geometry and optical performance data from the literature, the GRINCU lens model can quantitatively explain the lens paradox to a high degree of accuracy.

12. To explain the decline of lens power with aging, it is necessary to assume that the iso-indicial curvature gradient changes with age. In younger lenses, the inner surfaces are more curved than the outer ones. Conversely, in older lenses, the inner surfaces may even become flatter than the outer surfaces.

13. The decrease in curvature gradient (GRCU) with age contributes more to the decline in lens power than the changes in axial GRIN distribution. In fact, a concentric configuration of the IIS (G=1) maintains the equivalent refractive index almost constant with age, resulting in an increase in lens power with age.

8.3 FUTURE LINES OF RESEARCH

There are several intriguing research areas to pursue:

- Implementation of additional models for finite ray tracing, such as the AVOCADO (Sheil), which implicitly includes variable curvature gradients. An interesting approximation to the GRINCU model could be the simpler 4-surface lens model. Conducting a validation study of this approach may prove valuable for upcoming implementations.

- The development of increasingly realistic and precise eye models is essential for multiple basic, applied, and clinical applications. Several potential subfields of interest can be highlighted:
  - Generic (population average) wide-angle eye models that include changes with age, such as the Perpetual model [134], and accommodation.
  - Population models that expand on the work already done in this thesis with synthetic eye models in Chapter 5 (*Optical Performance of the GRINCU Lens in SyntEyes*).
  - The combination of biomechanical and optical models is particularly intriguing, as it not only represents a potential application of this thesis but also serves as a direct extension of the OBERON project, developed within the Marie Skłodowska-Curie Actions (MSCA), of which this thesis was part.
  - There are numerous potential applications for more realistic and accurate eye models in the clinical field, including assessing vision quality, developing optical implants (IOLs), planning treatments, and customizing surgeries (such as cataract and other refractive procedures).

TRADUCCIONES AL ESPAÑOL

9 RESÚMENES

1. INTRODUCCIÓN

Este primer capítulo presenta una revisión detallada de la anatomía, fisiología y características ópticas del ojo humano, con especial énfasis en el cristalino y su función esencial en la visión. Comienza describiendo la anatomía ocular, destacando la composición en capas del ojo: la capa fibrosa externa (esclerótica y córnea), la capa vascular media (iris, cuerpo ciliar y coroides) y la capa neural interna (retina). Aunque la córnea es el principal elemento refractivo óptico del ojo, el cristalino destaca como un componente clave, capaz de adaptar su geometría mediante el proceso de acomodación para enfocar objetos a diferentes distancias. Esta capacidad de adaptación se ve mejorada por el gradiente de índice de refracción (GRIN) del cristalino, que aumenta su potencia óptica y reduce las aberraciones.

Hay dos procesos que son esenciales para la función del cristalino: la acomodación y el envejecimiento. La acomodación es el proceso mediante el cual el cristalino varía su curvatura exterior y grosor para enfocar objetos cercanos. El mecanismo de acomodación intracapsular propuesto por Gullstrand atribuye en parte el aumento de potencia del cristalino durante la acomodación a los cambios en la distribución interna del índice de refracción. Este mecanismo sugiere que tanto los cambios externos como internos en la estructura del cristalino contribuyen a aumentar su potencia refractiva durante el proceso de acomodación. Se resalta el papel del GRIN en este mecanismo, que permite al cristalino alcanzar una mayor potencia refractiva de lo que sería posible con un índice de refracción homogéneo. En cuanto a los cambios relacionados con la edad, el crecimiento continuo y la agregación de proteínas afectan la estructura y las propiedades refractivas del cristalino. Estos cambios conducen, a medio plazo, a la presbicia, caracterizada por la pérdida de la capacidad de acomodación, y a largo plazo, a las cataratas, que opacan el cristalino y deterioran la visión.

La calidad óptica del ojo se ve principalmente afectada por las aberraciones, que se definen como desviaciones de los rayos de luz respecto a su trayectoria ideal. Entre estas aberraciones se encuentran las de bajo orden, como los errores refractivos esféricos (miopía e hipermetropía), el astigmatismo y la presbicia, y las aberraciones de alto orden, que son más complejas y menos comunes.

Por último, se incluye una revisión histórica de los modelos de ojo, en particular aquellos enfocados a replicar el comportamiento del cristalino. Modelos GRIN u otros más complejos como el GRINCU-objeto de esta tesis y que incluye un doble gradiente de índice (GRIN) y de curvatura (GRCU)-, buscan captar los cambios ópticos y estructurales que ocurren en el cristalino con la acomodación y la edad, proporcionando información valiosa para el diseño de intervenciones correctivas, como las lentes intraoculares y otros dispositivos ópticos. En este

sentido, el capítulo enfatiza la importancia de un modelado óptico preciso para avanzar en las ciencias de la visión y mejorar los tratamientos para los errores refractivos y las deficiencias visuales relacionadas con la edad. En general, establece una base integral para comprender la compleja relación entre la estructura, la función y el rendimiento óptico del ojo.

2. FORMULACIÓN DEL MODELO

El modelo GRINCU introduce un parámetro de gradiente de curvatura G que permite que la curvatura de las superficies isoíndice (IIS) varíe con la profundidad, lo que da lugar a configuraciones no concéntricas. En este modelo, tanto el cristalino como las IIS son biconvexos. La distribución del índice de refracción dentro de la lente se caracteriza por una ley de potencia derivada de datos experimentales, con distribuciones diferenciadas para las regiones anterior y posterior del cristalino. A diferencia de modelos previos, la interfaz en el modelo GRINCU es una superficie curva formada por el lugar geométrico de las intersecciones de los hemisferios anterior y posterior de las IIS. Este modelo también contempla superficies con simetría no rotacional, incorporando parámetros para el astigmatismo y el ángulo de rotación. Incluye, además, un componente dispersivo, definido por las ecuaciones de Cauchy, para considerar las variaciones del índice de refracción con la longitud de onda.

La parametrización de este modelo, junto con la incorporación del gradiente de curvatura y de superficies con simetría no rotacional, mejora la capacidad del modelo para simular el comportamiento óptico de la lente. Esta versatilidad permite la adaptación del modelo a geometrías y distribuciones del índice de refracción individuales, lo cual lo hace especialmente adecuado para estrategias de corrección visual personalizadas.

Esta formulación mejorada optimiza el modelo de Navarro (2021) al parametrizar las superficies isoíndice de forma explícita como función de los radios de curvatura, R_{as} y R_{ps}, y las constantes cónicas Q_a y Q_p de las superficies anterior y posterior de la lente lente, en lugar de depender de los semiejes de la cuádrica. Un hallazgo clave de este desarrollo es que, además de los radios externos de la lente, la curvatura de cada IIS también depende de la constante cónica externa. El gradiente de curvatura neto de las IIS está determinado por el producto de la constante cónica de las superficies externas y un parámetro de gradiente de curvatura, G, que puede ajustarse para cada caso individual.

3. MATRIZ DE TRANSFERENCIA ANALÍTICA

Se presenta aquí la formulación de una matriz de transferencia de rayos, o matriz ABCD, para lentes GRIN tipo cebolla. En estas lentes, denominadas así porque están conformadas por la superposición de muchas capas, cada IIS puede considerarse una superficie refractiva. Normalmente, la matriz ABCD de una lente GRIN se calcula multiplicando un número significativo de matrices de traslación y refracción, correspondientes a las capas que componen la lente. Si aplicamos una aproximación diferencial al grosor de las capas, el producto

de las matrices se puede simplificar a una suma. Los elementos A, B, C y D de esta matriz de transferencia GRIN aproximada se calculan mediante la integración de cada elemento de la matriz de una sola capa. Cabe destacar que esta matriz ABCD difiere de la de una lente homogénea en un término de integración en el elemento C, que refleja la contribución GRIN a la potencia óptica de la lente. Por lo tanto, la potencia total de la lente GRIN es la suma de la potencia de la lente homogénea y la contribución del GRIN, lo que da lugar a una expresión compacta y directa para la matriz ABCD. Después de obtener la matriz ABCD, se adapta esta formulación al cristalino y se implementan técnicas de integración numérica y analítica para determinar la potencia óptica del modelo de lente GRINCU. La aproximación analítica da una solución precisa usando funciones hipergeométricas gaussianas. Como última comprobación, se comparan las soluciones de este análisis con las de otras matrices de transferencia existentes en la literatura, analizando cómo la constante cónica (Q) de las superficies isoíndice y el gradiente de curvatura (G) afectan la potencia en diferentes modelos de lente.

4. TRAZADO DE RAYOS FINITO

El software comercial de trazado de rayos, como Zemax, no admite de forma nativa superficies GRIN personalizadas, pero se pueden incluir mediante la creación de superficies definidas por el usuario (*user-defined surfaces* en inglés). Con este objetivo, se implementaron las versiones singlete y doblete del modelo GRINCU en C++ y se exportaron a archivos DLL para su integración con Zemax OpticStudio. Además del software comercial, estos modelos se programaron también en RT Lib, una biblioteca de trazado de rayos para Matlab. Para validar la equivalencia entre el singlete y doblete y los dos software de trazado de rayos, se realizó un análisis paraxial y se compararon las propiedades ópticas—como la potencia refractiva, las distancias focales y los planos principales—entre Zemax, RT Lib y Python. En una segunda verificación, se evaluó el desenfoque, así como las aberraciones esféricas primaria y secundaria, comparando resultados entre Zemax y RT Lib.

Las superficies definidas por el usuario para las lentes GRIN siguen la estructura de DLL establecida por Zemax. En el caso de la lente tipo singlete, la distribución GRIN se configuró como un todo, mientras que en el doblete se modelaron por separado las regiones anterior y posterior de la lente. Para el modelo doblete, la interfaz se configuró como una superficie cónica, utilizando métodos numéricos para calcular la intersección de los hemisferios anterior y posterior, ajustando estos datos a una cónica mediante el método de Taubin. Aunque RT Lib no dispone de una interfaz gráfica, permite la definición y modificación de sistemas ópticos dentro de los scripts de Matlab. Esta flexibilidad amplía las capacidades de modelado proporcionadas por Zemax, creando un marco integral para el diseño y la aplicación de lentes GRIN personalizadas.

5. RENDIMIENTO ÓPTICO DE SYNTEYES CON LENTES GRIN

Para caracterizar la lente GRINCU, se analizaron los efectos de diferentes modelos de cristalino en el rendimiento óptico del ojo. Utilizando las biometrías de 200 SyntEyes, un banco de ojos sintéticos basados en datos estadísticos experimentales, se implementó cada uno de ellos con tres modelos de lente: una lente homogénea de dos superficies, una lente GRIN y nuestro modelo GRINCU, que incorpora un gradiente de curvatura en las superficies isoíndice. Mediante el trazado de rayos finito en los 200 ojos, se analizaron estos modelos de cristalino, evaluando cinco gradientes de curvatura diferentes para la configuración GRINCU. Durante el análisis, se calcularon los puntos cardinales y los coeficientes de Zernike promedio para cada muestra de SyntEyes, así como los puntos cardinales para cada modelo de lente.

Las configuraciones de lentes GRINCU con una curvatura creciente de las IIS hacia el centro producen un desplazamiento anterior de los planos principales de la lente, resultando en una mayor potencia ocular en comparación con el modelo de lente homogénea. En cuanto a las aberraciones ópticas, gradientes de curvatura de las IIS más pronunciados hacia el centro de la lente reducen el astigmatismo, el desenfoque, el coma lateral y la aberración esférica primaria. En conclusión, la interacción entre el gradiente de índice de la lente y el gradiente de curvatura de las IIS modifica las propiedades ópticas del ojo en su conjunto, destacando el papel fundamental de la configuración interna de la lente en el rendimiento óptico.

6. MECANISMO DE ACOMODACIÓN INTRACAPSULAR

El mecanismo de acomodación intracapsular (IAM, por sus siglas en inglés) puede interpretarse como un aumento en el índice de refracción equivalente del cristalino durante el proceso de acomodación del ojo. El objetivo de este capítulo es evaluar la presencia del IAM analizando los cambios observados en el gradiente de curvatura interna del cristalino cuando este acomoda. Para ello, se ajustó un modelo de lente GRINCU a datos experimentales publicados sobre los cambios en la geometría externa y del núcleo del cristalino durante la acomodación. Los datos se obtuvieron de dos fuentes: un vídeo Scheimpflug que mostraba un cristalino de 16 años acomodando y un estudio con 100 participantes sobre la acomodación y su dependencia de la edad. De este estudio, se obtuvieron ecuaciones para cada parámetro geométrico en función de la edad y el estímulo acomodativo, y se calcularon los valores para tres edades diferentes.

En cada caso analizado—el cristalino de 16 años del vídeo y los de 18, 29 y 45 años del estudio—se calculó la potencia refractiva y el índice equivalente para cada estado acomodativo utilizando la matriz de transferencia descrita en el Capítulo 3. Se observa un IAM positivo en todos los casos, con un índice de refracción equivalente que aumenta con la acomodación. Los resultados del estudio dependiente de la edad indican que el IAM no disminuye con la edad; por el contrario, parece aumentar entre los 18 y los 45 años. Estos hallazgos sugieren que la contribución del IAM a la respuesta total de acomodación

es inferior a un tercio de la potencia en todos los casos analizados, siendo la mayor contribución del 26% para el cristalino de 45 años, un valor inferior a los cálculos de Gullstrand.

7. EXPLICACIÓN CUANTITATIVA DE LA PARADOJA DEL CRISTALINO

La paradoja del cristalino es el fenómeno por el cual el cristalino humano pierde potencia refractiva a pesar del aumento de la curvatura exterior y grosor asociados con el envejecimiento. En este capítulo, se modela una lente GRINCU dependiente de la edad y se propone una explicación cuantitativa de esta paradoja. Utilizando diversas fuentes de la literatura, se configuró un cristalino de geometría variable con la edad y se implementó este modelo para un rango de edades entre 23 y 73 años. Ajustando el gradiente de curvatura (G) de las superficies isoíndice para cada edad, se optimizó la estructura interna de la lente para que la potencia refractiva se alineara con las medidas experimentales correspondientes a este rango de edad. Para contrastar los resultados obtenidos al variar G, también se modeló una configuración concéntrica de las IIS ($G = 1$) para cada edad. De las dos configuraciones, sólo el modelo con gradiente de curvatura variable puede replicar de manera satisfactoria el declive de la potencia asociado al envejecimiento, mientras que la configuración concéntrica muestra una tendencia de aumento de la potencia con la edad.

En las lentes jóvenes, las superficies isoíndice más cercanas al núcleo presentan una mayor curvatura que las más superficiales, lo que corresponde a valores negativos del parámetro de gradiente de curvatura ($G < 0$). A medida que la lente envejece, esta diferencia de curvatura disminuye, alcanzando una disposición paralela de las superficies isoíndice cuando $G = 0$. En las lentes más maduras, las IIS superficiales presentan más curvatura que las cercanas al núcleo, lo que corresponde a valores positivos de G ($G > 0$). Se observa, además, que un gradiente de curvatura variable con la edad afecta al índice de refracción equivalente de la lente, resultando en una disminución de aproximadamente 0.027 en su valor. En contraste, la configuración concéntrica mantiene un índice de refracción equivalente constante a lo largo de la vida. Para explicar la paradoja del cristalino, es esencial considerar cómo varía no sólo el gradiente del índice de refracción, sino también el gradiente de curvatura de las superficies isoíndice.

10 CONCLUSIONES

10.1 LOGROS

- Se ha desarrollado una formulación mejorada del modelo de cristalino GRINCU de Navarro (2021), en la que las superficies iso-índice están parametrizadas con los radios de curvatura externos y las constantes cónicas de la lente, en lugar de los semiejes cónicos y los valores de épsilon. Esta nueva formulación admite configuraciones paraboloides de las superficies iso-indiciales, lo cual no era posible en la versión anterior del modelo. Se han implementado numéricamente dos versiones del modelo: uno con simetría de rotación y un modelo general, astigmático. El modelo incluye además dispersión cromática.

- Se ha derivado una matriz de transferencia de rayos específica para lentes GRIN de tipo cebolla utilizando una aproximación diferencial del producto matricial de un gran número de capas. A partir de esta matriz de transferencia, se obtuvo y se verificó una ecuación integral para calcular la potencia óptica de la lente GRIN. Por último, se formuló una solución analítica específica para la lente del cristalino, con resultados precisos.

- Se ha realizado el trazado de rayos paraxial y finito para el modelo GRINCU en dos aplicaciones de software diferentes: Zemax (comercial) y RTLib (de acceso público), una biblioteca personalizada de trazado de rayos para Matlab. Con tal fin, se crearon superficies definidas por el usuario para configuraciones de lente en singlete y doblete, tras lo cual se llevó a cabo el trazado de rayos para determinar la potencia de la lente, los puntos cardinales y aberraciones. Se realizó una validación cruzada tanto entre los programas como entre el singlete y el doblete para verificar la precisión de los resultados.

- Se ha implementado el modelo GRINCU en SyntEyes [2], una base de datos sintética de biometría ocular que imita con gran precisión los datos biométricos reales de la población. Estos datos incluían las curvaturas y espesores de la córnea y la lente, la profundidad de la cámara anterior y del vítreo, así como la potencia refractiva de la lente, la córnea y del ojo en su conjunto. Mediante el trazado de rayos en RTLib, se determinaron las propiedades ópticas para diversas configuraciones de gradientes de curvatura en la lente GRINCU y se compararon con las de un modelo de lente homogénea. Los resultados permitieron evaluar el modelo de índice de gradiente frente al modelo homogéneo y analizar cómo las diferentes configuraciones de gradiente de curvatura afectan las propiedades ópticas del ojo.

- Se ha modelado la acomodación en lentes GRINCU a partir de datos experimentales de la literatura. Se realizó un estudio del mecanismo de acomodación intracapsular (IAM) de Gullstrand mediante el análisis de los cambios observados en el gradiente de curvatura interna de la lente con la acomodación en diferentes grupos de edad. Utilizando datos de dos fuentes bibliográficas, se calculó la distribución del índice de refracción, la potencia refractiva y los índices de refracción equivalentes en distintos estados de acomodación. Con estos datos, se determinó la contribución del IAM a la potencia acomodativa en una lente de 16 años en una de las fuentes, y en lentes de 18, 29 y 45 años en la otra.

- Se ha analizado la paradoja del cristalino. Para ello, se incorporaron al modelo GRINCU datos empíricos sobre el envejecimiento de la lente cristalina procedentes de dos fuentes bibliográficas. Estos datos incluían los cambios en la geometría de la lente y variaciones en la distribución del índice de refracción. A continuación, se ajustó el parámetro de gradiente de curvatura (G) para alinearlo con los valores de potencia refractiva medidos experimentalmente en individuos de entre 23 y 73 años. Para examinar el comportamiento del gradiente de curvatura interna con el envejecimiento, los valores obtenidos de G se ajustaron a un polinomio de cuarto grado para cada una de las dos geometrías.

10.2 CONCLUSIONES

1. La matriz de transferencia de rayos para medios de lente GRIN continuos tipo cebolla es similar a la de una única capa, donde los elementos A, B, C y D de la matriz se reemplazan por sus respectivas integrales. Esto permite el cálculo eficiente y directo de la potencia del sistema óptico. Las integrales de los elementos A, B y D son cero; por lo tanto, la matriz de transferencia de rayos del medio GRIN es una matriz de un solo elemento (C), denominada $\mathcal{G}$.

2. La matriz de transferencia de la lente puede expresarse como la suma $L = H + \mathcal{G}$, donde H representa la matriz de transferencia de una lente homogénea estándar con un índice de refracción igual al de la superficie de la lente, y $\mathcal{G}$ encapsula la contribución de la estructura interna GRIN.

3. En lentes tipo menisco con radios de curvatura anterior y posterior idénticos, la ausencia de un gradiente de curvatura implica que la contribución del GRIN a la potencia refractiva de la lente es nula. Por el contrario, en lentes biconvexas, donde las curvaturas anterior y posterior tienen signos opuestos, el GRIN sí contribuye a la potencia.

4. Diferentes implementaciones de trazado finito de rayos a través de lentes GRINCU–ya sea en software personalizado como RTLib o en plataformas comerciales como Zemax, así como en configuraciones de singlete o doblete–dan resultados equivalentes tanto en potencia refractiva como en aberraciones, lo cual indica una validación cruzada de estos métodos.

5. El gradiente del radio de curvatura, G, y la constante cónica, Q, tienen un impacto notable en la potencia refractiva de los modelos del cristalino. Los valores más negativos de Q dan lugar a menos potencia refractiva que los valores positivos. Por el contrario, parámetros más negativos del gradiente de curvatura dan lugar a un aumento en la potencia de la lente.

6. El gradiente de curvatura de las IIS desplaza los planos principales en una lente GRINCU cuando se comparan con los de una lente homogénea de la misma geometría externa y potencia. Un gradiente positivo ($g > 0$) desplaza los planos principales hacia la cara anterior de la lente, mientras que un gradiente negativo ($g < 0$) los desplaza hacia la cara posterior.

7. En ojos con idéntica geometría, un gradiente positivo de curvatura en la IIS de la lente genera un aumento en la potencia ocular. Además, incrementa la coma vertical y reduce el astigmatismo, la coma lateral y la aberración esférica.

8. La contribución del mecanismo de acomodación intracapsular (IAM) al aumento de la potencia durante la acomodación es considerablemente menor que la predicha por Gullstrand, especialmente en lentes jóvenes.

9. El gradiente de curvatura de las IIS de la lente contribuye al cambio de potencia refractiva durante la acomodación. Esta contribución tiene un efecto multiplicativo con la variación en la distribución del índice de refracción.

10. En modelos de lente con gradiente de índice (GRIN) y gradiente de curvatura (GRCU), el mecanismo de acomodación intracapsular es positivo y aumenta entre los 18 y 45 años. Este incremento con la edad podría compensar parcialmente el deterioro en la respuesta acomodativa asociado al envejecimiento.

11. Usando datos experimentales de la geometría y el rendimiento óptico del cristalino, el modelo GRINCU permite explicar cuantitativamente la paradoja del cristalino con un alto grado de precisión.

12. Para explicar la pérdida de potencia refractiva de la lente con el envejecimiento, es necesario asumir que el gradiente de curvatura iso-índice cambia con la edad. En lentes jóvenes, las superficies internas son más curvadas que las externas. En cambio, en lentes más maduras, las superficies más profundas pueden llegar a ser incluso más planas que las externas.

13. La disminución del gradiente de curvatura (GRCU) con la edad contribuye en mayor medida a la reducción de la potencia de la lente que los cambios en la distribución axial del GRIN. De hecho, una configuración concéntrica de la IIS (G=1) mantiene el índice de refracción equivalente casi constante con la edad, lo que da lugar a un aumento de la potencia de la lente con el envejecimiento.

10.3 LÍNEAS DE INVESTIGACIÓN FUTURAS

A continuación, se presentan algunas líneas de investigación interesantes a seguir:

- Implementación de modelos adicionales para el trazado finito de rayos, como el modelo AVOCADO [70], que incorpora de forma implícita gradientes de curvatura variables. Una posible aproximación simplificada al modelo GRINCU podría ser el modelo de lente de cuatro superficies, cuya validación podría resultar de utilidad para futuras implementaciones.
- El desarrollo de modelos oculares cada vez más realistas y precisos es fundamental para diversas aplicaciones básicas y clínicas. Se pueden destacar varias áreas de potencial interés:
  - Modelos oculares genéricos (promedio de la población) de gran ángulo que incorporen cambios con la edad, como el modelo Perpetual [134], y la acomodación.
  - Modelos poblacionales que continúen el trabajo que se ha desarrollado en esta tesis con modelos sintéticos del ojo en el capítulo 6 (*Rendimiento óptico de SyntEyes con lentes GRIN*).
  - La combinación de modelos biomecánicos y ópticos es de especial interés, ya que no solo representa una posible aplicación de esta tesis, sino que también constituye una extensión directa del proyecto OBERON, dentro del programa Marie Skłodowska-Curie Actions (MSCA), del cual esta tesis ha formado parte.
  - Existen numerosas aplicaciones potenciales de modelos oculares más realistas y precisos en el ámbito clínico, como la evaluación de la calidad visual, el desarrollo de implantes ópticos (IOLs), la planificación de tratamientos y la personalización de cirugías (de cataratas y otros problemas refractivos).

APPENDICES

A STATISTICAL RESULTS

A.1 EYE ABERRATIONS

Table A.1: Average Zernike aberration terms for each model and G value used. Standard deviations are provided in parentheses.

Model	G	Z3	Z4	Z5	Z7	Z8	Z12
Equivalent	-	0.012	0.593	0.076	-0.019	-0.162	0.121
		(0.053)	(2.238)	(0.039)	(0.041)	(0.049)	(0.018)
GRIN	-	0.059	0.656	0.115	-0.006	-0.145	0.137
		(0.081)	(2.236)	(0.061)	(0.037)	(0.043)	(0.016)
GRINCU	+1	0.059	0.677	0.116	-0.006	-0.144	0.136
		(0.081)	(2.235)	(0.062)	(0.037)	(0.042)	(0.016)
GRINCU	0	0.057	0.696	0.113	-0.008	-0.139	0.125
		(0.079)	(2.234)	(0.060)	(0.035)	(0.042)	(0.018)
GRINCU	-1	0.054	0.689	0.111	-0.012	-0.132	0.103
		(0.075)	(2.238)	(0.058)	(0.035)	(0.041)	(0.024)
GRINCU	-1.5	0.052	0.619	0.110	-0.017	-0.126	0.078
		(0.073)	(2.268)	(0.057)	(0.042)	(0.042)	(0.039)
GRINCU	-2	0.049	0.237	0.109	-0.026	-0.118	0.030
		(0.068)	(2.457)	(0.056)	(0.061)	(0.045)	(0.063)

Z3: 45^0 primary astigmatism
Z4: defocus
Z5: 0^0 primary astigmatism
Z7: primary x-coma
Z8: primary y-coma
Z12: primary spherical aberration

A.1.1 Equivalent vs. All T-test Results

Table A.2: T-test results comparing the ocular aberrations of all GRIN and GRINCU lens models with the equivalent lens model. After applying the Bonferroni correction, we used a modified alpha value of $\alpha' = \alpha/6 = 0.008333$. The correlation value r is provided in parentheses. Shaded cells are used to highlight the models and configurations that showed statistically significant differences with the equivalent lens model.

Model	G	Z3	Z4	Z5	Z7	Z8	Z12
Equivalent	-	-	-	-	-	-	-
GRIN	-	$< \alpha'$	0.777	$< \alpha'$	$< \alpha'$	$< \alpha'$	$< \alpha'$
		(0.905)	(1.000)	(0.979)	(0.973)	(0.998)	(0.964)
GRINCU	+1	$< \alpha'$	0.704	$< \alpha'$	$< \alpha'$	$< \alpha'$	$< \alpha'$
		(0.903)	(1.000)	(0.979)	(0.975)	(0.998)	(0.973)
GRINCU	0	$< \alpha'$	0.643	$< \alpha'$	$< \alpha'$	$< \alpha'$	0.029
		(0.902)	(1.000)	(0.981)	(0.995)	(0.997)	(0.998)
GRINCU	-1	$< \alpha'$	0.667	$< \alpha'$	0.064	$< \alpha'$	$< \alpha'$
		(0.901)	(1.000)	(0.982)	(0.955)	(0.992)	(0.969)
GRINCU	-1.5	$< \alpha'$	0.907	$< \alpha'$	0.596	$< \alpha'$	$< \alpha'$
		(0.901)	(0.999)	(0.982)	(0.791)	(0.983)	(0.892)
GRINCU	-2	$< \alpha'$	0.132	$< \alpha'$	0.225	$< \alpha'$	$< \alpha'$
		(0.898)	(0.977)	(0.975)	(0.523)	(0.954)	(0.830)

Z3: 45^0 primary astigmatism
Z4: defocus
Z5: 0^0 primary astigmatism
Z7: primary x-coma
Z8: primary y-coma
Z12: primary spherical aberration

A.1.2 GRIN vs. All T-test Results

Table A.3: T-test results comparing the ocular aberrations of all GRIN and GRINCU lens models with the GRIN lens model. After applying the Bonferroni correction, we used a modified alpha value of $\alpha' = \alpha/6 = 0.008333$. The correlation value r is provided in parentheses. Shaded cells are used to highlight the models and configurations that showed statistically significant differences with the equivalent lens model.

Model	G	Z3	Z4	Z5	Z7	Z8	Z12
Equivalent	-	$< \alpha'$	0.777	$< \alpha'$	$< \alpha'$	$< \alpha'$	$< \alpha'$
		(0.905)	(1.000)	(0.979)	(0.973)	(0.998)	(0.964)
GRIN	-	-	-	-	-	-	-
GRINCU	+1	0.980	0.924	0.979	0.972	0.809	0.507
		(1.000)	(1.000)	(1.000)	(1.000)	(1.000)	(0.999)
GRINCU	0	0.820	0.858	0.751	0.573	0.153	$< \alpha'$
		(1.000)	(1.000)	(1.000)	(0.987)	(0.999)	(0.979)
GRINCU	-1	0.573	0.884	0.496	0.089	$< \alpha'$	$< \alpha'$
		(0.999)	(1.000)	(0.998)	(0.871)	(0.994)	(0.874)
GRINCU	-1.5	0.412	0.869	0.399	$< \alpha'$	$< \alpha'$	$< \alpha'$
		(0.998)	(0.999)	(0.994)	(0.644)	(0.984)	(0.749)
GRINCU	-2	0.205	0.076	0.269	$< \alpha'$	$< \alpha'$	$< \alpha'$
		(0.992)	(0.977)	(0.976)	(0.329)	(0.953)	(0.659)

Z3: 45^0 primary astigmatism
Z4: defocus
Z5: 0^0 primary astigmatism
Z7: primary x-coma
Z8: primary y-coma
Z12: primary spherical aberration

A.2 PARAXIAL ANALYSIS

Table A.4: Average results of the paraxial analysis for the lens and eye optical systems. Standard deviations are shown in parentheses.

Model	G	n	VH_{lens} (mm)	$V'H'_{lens}$ (mm)	P_{eye} (D)	VN_{eye} (mm)	$V'N'_{eye}$ (mm)	VH_{eye} (mm)	$V'H'_{eye}$ (mm)	FFL_{eye} (mm)	BFL_{eye} (mm)
Equivalent	-	1.4316	2.319	-1.529	60.67	7.099	-0.037	1.531	-5.605	-14.971	16.465
		(0.0092)	(0.235)	(0.163)	(2.04)	(0.174)	(0.307)	(0.095)	(0.324)	(0.601)	(0.692)
GRIN	-	1.4344	2.393	-1.482	60.61	7.125	-0.036	1.553	-5.608	-14.963	16.481
		(0.0092)	(0.243)	(0.147)	(2.03)	(0.171)	(0.305)	(0.097)	(0.323)	(0.603)	(0.686)
GRINCU	+1	1.4341	2.372	-1.503	60.63	7.118	-0.041	1.547	-5.612	-14.966	16.471
		(0.0093)	(0.238)	(0.152)	(2.03)	(0.172)	(0.305)	(0.096)	(0.323)	(0.602)	(0.688)
GRINCU	0	1.4316	2.338	-1.542	60.65	7.105	-0.057	1.536	-5.626	-14.969	16.448
		(0.0092)	(0.230)	(0.161)	(2.04)	(0.174)	(0.306)	(0.095)	(0.322)	(0.602)	(0.691)
GRINCU	-1	1.4284	2.294	-1.592	60.69	7.090	-0.078	1.524	-5.644	-14.974	16.419
		(0.0093)	(0.218)	(0.175)	(2.05)	(0.176)	(0.308)	(0.094)	(0.322)	(0.601)	(0.696)
GRINCU	-1.5	1.4260	2.266	-1.625	60.71	7.080	-0.092	1.515	-5.656	-14.976	16.400
		(0.0097)	(0.209)	(0.186)	(2.05)	(0.177)	(0.309)	(0.093)	(0.322)	(0.600)	(0.700)
GRINCU	-2	1.4220	2.241	-1.671	60.72	7.071	-0.111	1.508	-5.674	-14.979	16.376
		(0.0112)	(0.208)	(0.209)	(2.05)	(0.178)	(0.313)	(0.093)	(0.323)	(0.600)	(0.706)

VH: Object principal plane
V′H′: Image principal plane
P: Power
VN: Object nodal plane
V′N′: Image nodal plane
FFL: Front focal length
BFL: Back focal length

B TAUBIN'S METHOD FOR CURVE FITTING

Non-linear conic surface fitting algorithms may yield significantly biased estimates of the conic constant, especially when the available arc subtends only a small fraction of the whole conic surface. To ensure convergence, robustness, and accuracy, we implemented Taubin's linear least squares ellipse fitting method [24], which minimizes the mean square distance between the data points and the conic. This method was used to fit both the lens nucleus and external surfaces. Beyond the inherent advantages of linear least squares methods as compared with non-linear algorithms, Taubin's method incorporates prior data normalization, which is extremely powerful in delivering stable and reliable estimates of all parameters, including the conic constant.

We assumed that the four surfaces of the lens were rotationally symmetric quadrics and that conic sections could approximate our two-dimensional contours. Any quadratic curve involving two variables can be expressed as a polynomial in terms of powers of z and ω:

$$F_0 + F_1 z^2 + F_2 z\omega + F_3 \omega^2 + F_4 z + F_5 \omega = 0 \tag{B.1}$$

Our goal was to determine the Fn coefficients necessary to compute the conic parameters, mainly the type of conic, the semiaxes, and the principal axis orientation. Taubin's ellipse fitting method requires data normalization to achieve optimal results. Therefore, we first normalized the datasets using the mean values $\bar{z}$, $\overline{\omega}$ and standard deviations $\overline{\sigma_z}$, $\overline{\sigma_\omega}$. The normalized variables Z and Ω are defined as:

$$Z = \frac{(z - \bar{z})\sqrt{2}}{\overline{\sigma_z}} \tag{B.2a}$$

$$\Omega = \frac{(\omega - \overline{\omega})\sqrt{2}}{\overline{\sigma_\omega}}, \tag{B.2b}$$

forming a new bivariate polynomial with coefficients $a_n(F_n, \bar{z}, \overline{\omega}, \overline{\sigma_z}, \overline{\sigma_\omega})$:

$$a_0 + a_1 Z^2 + a_2 Z\Omega + a_3 \Omega^2 + a_4 Z + a_5 \Omega = 0 \tag{B.3}$$

The use of a general formulation that accommodates any possible position or orientation of the conic, along with the coordinate normalization, ensures that the conic shape parameters (R and Q) remain invariant and entirely independent of the selected coordinate origin.

The least-square fitting of the matrix with columns $[Z^2, Z\Omega, \Omega^2, Z, \Omega]$ yielded the values of coefficients a_0 to a_5. Subsequently, we rearranged eq. (B.3) to denormalize the variables and determine F_0 through F_5. With the F_n coefficients of the now adjusted surfaces, we reconstructed the ellipses and calculated the fit error. To determine the cortex and lens thicknesses, we measured the distance between the points where the curves intersect the principal axis. The final step for obtaining the required curve parameters was to convert the conic implicit equation to its canonical form (Appendix C).

C IMPLICIT TO CANONICAL CONIC EQUATION TRANSFORMATION

The axial radius of curvature and the conic constant of a central conic (ellipse or hyperbola) can be determined using the semiaxes: $R = b^2/a$ and $Q = \varepsilon b^2/a^2 - 1$, where $\varepsilon = -1$ for hyperbolas and $\varepsilon = +1$ for ellipses. For parabolas, $\varepsilon = 0$, $Q = -1$, and the radius of curvature is given by $R = 2p$, where p is the distance between the vertex and the focus. To convert the implicit equation to its canonical form, we applied the matrix representation of conic sections [25]. The determinant of the equation matrix, $\mathcal{A}$, the determinant of element $\mathcal{A}_{33}$, denoted as $D = |\mathcal{A}_{33}|$, and its trace, $I = \mathrm{tr}(\mathcal{A}_{33})$ remain invariant to rotation and translation. These invariants define the quadric properties that are independent of the conic section's position.

$$\mathcal{A} = \begin{bmatrix} F_1 & F_2/2 & F_4/2 \\ F_2/2 & F_3 & F_4/2 \\ F_4/2 & F_5/2 & F_0 \end{bmatrix} \tag{C.1}$$

$$D = |\mathcal{A}_{33}| = F_1 F_3 - \frac{F_2^2}{4} = \begin{cases} D > 0 & \text{for ellipses} \\ D = 0 & \text{for parabolas} \\ D < 0 & \text{for hyperbolas} \end{cases} \tag{C.2}$$

$$I = F_1 + F_3 \tag{C.3}$$

Invariants $\mathcal{A}$, D, I, and the roots of the characteristic equation $\lambda^2 - I\lambda + D = 0$ allow us to calculate the squared semiaxes of the conic, a^2 and b^2, or the semilatus rectum (p) for parabolas.

$$\text{Ellipses:} \quad \begin{cases} a^2 = \dfrac{-\mathcal{A}}{\lambda_2 D} \\ b^2 = \dfrac{-\mathcal{A}}{\lambda_1 D} \end{cases} \tag{C.4}$$

$$\text{Hyperbolas:} \quad \begin{cases} a^2 = \dfrac{-\mathcal{A}}{\lambda_1 D} \\ b^2 = \dfrac{\mathcal{A}}{\lambda_2 D} \end{cases} \tag{C.5}$$

$$\text{Parabolas:} \quad p = \frac{1}{2}\sqrt{\frac{-\mathcal{A}}{I^3}} \tag{C.6}$$

Where $\lambda_1 > \lambda_2$. If there are no cross terms in the implicit equation, then $F_2 = 0$, and there are two possible orientations for the principal axis of the conic. If $F_1 < F_3$, the conic central axis is along z, but if $F_1 > F_3$, it is rotated $\pi/2$ rad from the positive z-axis. Therefore, to calculate R and Q correctly, semiaxes a and b must be swapped in the equations $R = a^2/b$ and $Q = \varepsilon a^2/b^2$–1.

BIBLIOGRAPHY

1. Navarro, R., Lockett-Ruiz, V. & López, J. L. Analytical ray transfer matrix for the crystalline lens. *Biomedical Optics Express* **13,** 5836–5848 (2022).
2. Rozema, J. J., Rodriguez, P., Navarro, R. & Tassignon, M.-J. SyntEyes: a higher-order statistical eye model for healthy eyes. *Investigative ophthalmology & visual science* **57,** 683–691 (2016).
3. Navarro, R., Baquedano, S. & Sánchez-Cano, A. I. GRINCU lens with conicoid iso-indicial surfaces: application for modeling the crystalline lens. *Optics Express* **29,** 30998–31009 (2021).
4. Lockett-Ruiz, V., Navarro, R. & López-Gil, N. Intracapsular accommodation mechanism in terms of lens curvature gradient. *Ophthalmic and Physiological Optics* **44,** 334–346 (2024).
5. Lockett-Ruiz, V., Navarro, R. & Rozema, J. Effect of gradient-index lenses on the optical performance of SyntEyes. en. *J. Optom.* **18,** 100568 (July 2025).
6. Lockett-Ruiz, V. & Navarro, R. Modeling the aging crystalline lens: a quantitative explanation of the lens paradox. en. *J. Opt. Soc. Am. A Opt. Image Sci. Vis.* **42,** 1048 (Aug. 2025).
7. Lockett-Ruiz, V., Evans, T., Navarro, R., Mashige, K. P. & Rozema, J. J. Zulu ocular biometry differs fundamentally from that of Europeans–A modelling analysis. *Ophthalmic and Physiological Optics* (2025).
8. Meeney, A & Mudhar, H. Histopathological reporting of corneal pathology by a biomedical scientist: the Sheffield Experience. *Eye* **27,** 272–276 (2013).
9. Quinlan, R. A. & Clark, J. I. Insights into the biochemical and biophysical mechanisms mediating the longevity of the transparent optics of the eye lens. *Journal of Biological Chemistry* **298** (2022).
10. Smith, G., Cox, M. J., Calver, R. & Garner, L. F. The spherical aberration of the crystalline lens of the human eye. *Vision Research* **41,** 235–243 (2001).
11. Nakao, S. Model of refractive indices in the human crystalline lens. *Jpn. J. Clin. Ophthalmol.* **23,** 903–906 (1969).
12. Sivak, J. & Mandelman, T. Chromatic dispersion of the ocular media. *Vision research* **22,** 997–1003 (1982).
13. Fagerholm, P. P., Philipson, B. T. & Lindström, B. Normal human lens—the distribution of protein. *Experimental eye research* **33,** 615–620 (1981).
14. Pierscionek, B. K. Refractive index of the human lens surface measured with an optic fibre sensor. *Ophthalmic research* **26,** 32–35 (1994).
15. Chan, D. Y., Ennis, J. P., Pierscionek, B. K. & Smith, G. Determination and modeling of the 3-D gradient refractive indices in crystalline lenses. *Applied Optics* **27,** 926–931 (1988).

16. Beliakov, G. & Chan, D. Analysis of inhomogeneous optical systems by the use of ray tracing. II. Three-dimensional systems with symmetry. *Applied optics* **37,** 5106–5111 (1998).

17. Qiu, C., Maceo Heilman, B., Kaipio, J., Donaldson, P. & Vaghefi, E. Fully automated laser ray tracing system to measure changes in the crystalline lens GRIN profile. *Biomedical optics express* **8,** 4947–4964 (2017).

18. Moffat, B., Atchison, D. & Pope, J. Age-related changes in refractive index distribution and power of the human lens as measured by magnetic resonance micro-imaging in vitro. *Vision research* **42,** 1683–1693 (2002).

19. Jones, C. E., Atchison, D. A., Meder, R. & Pope, J. M. Refractive index distribution and optical properties of the isolated human lens measured using magnetic resonance imaging (MRI). *Vision research* **45,** 2352–2366 (2005).

20. Bahrami, M., Hoshino, M., Pierscionek, B., Yagi, N., Regini, J. & Uesugi, K. Refractive index degeneration in older lenses: A potential functional correlate to structural changes that underlie cataract formation. *Experimental eye research* **140,** 19–27 (2015).

21. Pierscionek, B., Bahrami, M., Hoshino, M., Uesugi, K., Regini, J. & Yagi, N. The eye lens: age-related trends and individual variations in refractive index and shape parameters. *Oncotarget* **6,** 30532 (2015).

22. Borja, D., Siedlecki, D., de Castro, A., Uhlhorn, S., Ortiz, S., Arrieta, E., Parel, J.-M., Marcos, S. & Manns, F. Distortions of the posterior surface in optical coherence tomography images of the isolated crystalline lens: effect of the lens index gradient. *Biomedical optics express* **1,** 1331–1340 (2010).

23. De Castro, A., Barbero, S., Ortiz, S. & Marcos, S. Accuracy of the reconstruction of the crystalline lens gradient index with optimization methods from Ray Tracing and Optical Coherence Tomography data. *Optics express* **19,** 19265–19279 (2011).

24. De Castro, A., Siedlecki, D., Borja, D., Uhlhorn, S., Parel, J.-M., Manns, F. & Marcos, S. Age-dependent variation of the gradient index profile in human crystalline lenses. *Journal of modern optics* **58,** 1781–1787 (2011).

25. Siedlecki, D., de Castro, A., Gambra, E., Ortiz, S., Borja, D., Uhlhorn, S., Manns, F., Marcos, S. & Parel, J.-M. Distortion correction of OCT images of the crystalline lens: gradient index approach. *Optometry and Vision Science* **89,** E709–E718 (2012).

26. Jones, C. E., Atchison, D. A. & Pope, J. M. Changes in lens dimensions and refractive index with age and accommodation. *Optometry and Vision Science* **84,** 990–995 (2007).

27. Kasthurirangan, S., Markwell, E. L., Atchison, D. A. & Pope, J. M. In vivo study of changes in refractive index distribution in the human crystalline lens with age and accommodation. *Investigative ophthalmology & visual science* **49,** 2531–2540 (2008).

28. Adnan, A., Pope, J. M., Sepehrband, F., Suheimat, M., Verkicharla, P. K., Kasthurirangan, S. & Atchison, D. A. Lens shape and refractive index distribution in type 1 diabetes. *Investigative ophthalmology & visual science* **56,** 4759–4766 (2015).

29. Pan, X., Lie, A. L., White, T. W., Donaldson, P. J. & Vaghefi, E. Development of an in vivo magnetic resonance imaging and computer modelling platform to investigate the physiological optics of the crystalline lens. *Biomedical Optics Express* **10,** 4462–4478 (2019).

30. Lie, A. L., Pan, X., White, T. W., Donaldson, P. J. & Vaghefi, E. Using the lens paradox to optimize an in vivo MRI-based optical model of the aging human crystalline lens. *Translational Vision Science & Technology* **9,** 39–39 (2020).

31. Jakobiec, F. A. *Ocular anatomy, embryology, and teratology* (Harpercollins, 1982).

32. *2020–2021 BCSC Basic and Clinical Science Course*™ `https://www.aao.org/education/bcscsnippetdetail.aspx?id=43fd133d-1389-44d7-8be2-e2db1dda79cf` (2024).

33. Atchison, D. *Optics of the human eye* (CRC Press, 2023).

34. López-Gil, N. *Gullstrand Intracapsular Accommodation Mechanism Revised* in *Photonics* **9** (2022), 152.

35. LeGrand, Y. & ElHage, S. G. *Physiological optics* (Springer, 2013).

36. Navarro, R., Santamaria, J. & Bescós, J. Accommodation-dependent model of the human eye with aspherics. *JOSA A* **2,** 1273–1280 (1985).

37. Zapata-Díaz, J. F., Radhakrishnan, H., Charman, W. N. & López-Gil, N. Accommodation and age-dependent eye model based on in vivo measurements. *Journal of optometry* **12,** 3–13 (2019).

38. Navarro, R. Adaptive model of the aging emmetropic eye and its changes with accommodation. *Journal of Vision* **14,** 21–21 (2014).

39. Navarro, R. & López-Gil, N. Impact of internal curvature gradient on the power and accommodation of the crystalline lens. *Optica* **4,** 334–340 (2017).

40. Maceo, B. M., Manns, F., Borja, D., Nankivil, D., Uhlhorn, S., Arrieta, E., Ho, A., Augusteyn, R. C. & Parel, J.-M. Contribution of the crystalline lens gradient refractive index to the accommodation amplitude in non-human primates: in vitro studies. *Journal of vision* **11,** 23–23 (2011).

41. Hermans, E. A., Dubbelman, M., Van der Heijde, R. & Heethaar, R. M. Equivalent refractive index of the human lens upon accommodative response. *Optometry and Vision Science* **85,** 1179–1184 (2008).

42. Garner, L. F. & Smith, G. Changes in equivalent and gradient refractive index of the crystalline lens with accommodation. *Optometry and Vision Science* **74,** 114–119 (1997).

43. Dubbelman, M., Van der Heijde, G., Weeber, H. A. & Vrensen, G. Changes in the internal structure of the human crystalline lens with age and accommodation. *Vision research* **43,** 2363–2375 (2003).

44. Gullstrand, A. How I found the mechanism of intracapsular accommodation. *Nobel lecture,* 383–415 (1911).

45. Levin, L. A., Nilsson, S. F., Ver Hoeve, J., Wu, S., Kaufman, P. L. & Alm, A. *Adler's Physiology of the Eye: Expert Consult-Online and Print* (Elsevier Health Sciences, 2011).

46. Listing, B. in *R. Wagner's Handwörterbuch der Physiologie mit Rücksicht auf physiologische Pathologie* Google-Books-ID: 6sUEAAAAYAAJ, 451–504 (F. Vieweg und Sohn, 1853).

47. Bennett, A. & Rabbetts, R. Proposals for new reduced and schematic eyes. *Ophthalmic & Physiological Optics: the Journal of the British College of Ophthalmic Opticians (Optometrists)* **9,** 228–230 (1989).

48. Emsley, H. *Visual Optics Visual Optics* **v. 1.** ISBN: 978-0-407-93403-0 (Hatton Press, 1952).

49. Von Helmholtz, H. *Handbuch der physiologischen Optik* (Voss, 1867).

50. Gullstrand, A. *Handbuch der Physiologischen Optik. Appendices II and IV* (Leopold Voss, Leipzig, Germany, 1909).

51. Tscherning, M. H. E. *Physiologic Optics* (Keystone Publishing Company, 1920).

52. Thibos, L. N., Ye, M., Zhang, X. & Bradley, A. *The chromatic eye: A new model of ocular chromatic aberration* in *Ophthalmic and Visual Optics* (1991), ThB1.

53. Tucker, J. The chromatic aberration of the eye between wavelengths 200 nm and 2000 nm: some theoretical considerations. *The British Journal of Physiological Optics* **29,** 118–125 (1974).

54. Drasdo, N & Fowler, C. Non-linear projection of the retinal image in a wide-angle schematic eye. *The British journal of ophthalmology* **58,** 709 (1974).

55. Kooijman, A. C. Light distribution on the retina of a wide-angle theoretical eye. *JOSA* **73,** 1544–1550 (1983).

56. Lotmar, W. Theoretical eye model with aspherics. *JOSA* **61,** 1522–1529 (1971).

57. Blaker, J. W. Toward an adaptive model of the human eye. *JOSA* **70,** 220–223 (1980).

58. Pomerantzeff, O., Pankratov, M., Wang, G.-J. & Dufault, P. Wide-angle optical model of the eye. *Optometry and Vision Science* **61,** 166–176 (1984).

59. Smith, G., Pierscionek, B. K. & Atchison, D. A. The optical modelling of the human lens. *Ophthalmic and Physiological Optics* **11,** 359–369 (1991).

60. Atchison, D. A. & Smith, G. Chromatic dispersions of the ocular media of human eyes. *JOSA A* **22,** 29–37 (2005).

61. Lombardo, M. & Lombardo, G. New methods and techniques for sensing the wave aberrations of human eyes. *Clinical and Experimental Optometry* **92,** 176–186 (2009).

62. Montés-Micó, R. Evaluation of 6 biometers based on different optical technologies. *Journal of Cataract & Refractive Surgery* **48,** 16–25 (2022).

63. Díaz, J. A., Pizarro, C. & Arasa, J. Single dispersive gradient-index profile for the aging human lens. *Journal of the Optical Society of America A* **25,** 250–261 (2007).

64. Goncharov, A. V. & Dainty, C. Wide-field schematic eye models with gradient-index lens. *JOSA A* **24,** 2157–2174 (2007).

65. Li, Q. & Fang, F. Physiology-like crystalline lens modelling for children. *Optics Express* **28,** 27155–27180 (2020).

66. Navarro, R., Palos, F. & González, L. Adaptive model of the gradient index of the human lens. I. Formulation and model of aging ex vivo lenses. *JOSA A* **24,** 2175–2185 (2007).

67. Kasprzak, H. T. New approximation for the whole profile of the human crystalline lens. *Ophthalmic and Physiological Optics* **20,** 31–43 (2000).

68. Popiolek-Masajada, A. & Kasprzak, H. Model of the optical system of the human eye during accommodation. *Ophthalmic and Physiological Optics* **22,** 201–208 (2002).

69. Bahrami, M. & Goncharov, A. V. Geometry-invariant gradient refractive index lens: analytical ray tracing. *Journal of Biomedical Optics* **17,** 055001 (2012).

70. Sheil, C. J. & Goncharov, A. V. Accommodating volume-constant age-dependent optical (AVOCADO) model of the crystalline GRIN lens. *Biomedical optics express* **7,** 1985–1999 (2016).

71. Smith, G., Bedggood, P., Ashman, R., Daaboul, M. & Metha, A. Exploring ocular aberrations with a schematic human eye model. *Optometry and Vision Science* **85,** 330–340 (2008).

72. Díaz, J. A., Fernández-Dorado, J. & Sorroche, F. Role of the human lens gradient-index profile in the compensation of third-order ocular aberrations. *Journal of biomedical optics* **17,** 075003–075003 (2012).

73. Birkenfeld, J., de Castro, A. & Marcos, S. Contribution of shape and gradient refractive index to the spherical aberration of isolated human lenses. *Investigative Ophthalmology & Visual Science* **55,** 2599–2607 (2014).

74. Li, Q. & Fang, F. Impacts of the gradient-index crystalline lens structure on its peripheral optical power profile. *Advanced Optical Technologies* **11,** 23–32 (2022).

75. Navarro, R. The optical design of the human eye: a critical review. *Journal of Optometry* **2,** 3–18 (2009).

76. Rozema, J. J., Tassignon, M.-J., *et al.* The bigaussian nature of ocular biometry. *Optometry and Vision Science* **91,** 713–722 (2014).

77. Navarro, R., González, L. & Hernández-Matamoros, J. L. On the prediction of optical aberrations by personalized eye models. *Optometry and Vision Science* **83,** 371–381 (2006).

78. Bahrami, M. & Goncharov, A. V. Geometry-invariant gradient refractive index lens: analytical ray tracing. *Journal of Biomedical Optics* **17,** 055001–055001 (2012).

79. De Castro, A., Ortiz, S., Gambra, E., Siedlecki, D. & Marcos, S. Three-dimensional reconstruction of the crystalline lens gradient index distribution from OCT imaging. *Optics express* **18,** 21905–21917 (2010).

80. Pierscionek, B. K. Refractive index contours in the human lens. *Experimental Eye Research* **64,** 887–893 (1997).

81. Bahrami, M. & Goncharov, A. V. Geometry-invariant GRIN lens: isodispersive contours. *Biomedical optics express* **3,** 1684–1700 (2012).

82. Bahrami, M. & Goncharov, A. V. Geometry-invariant GRIN lens: finite ray tracing. *Optics express* **22,** 27797–27810 (2014).

83. Khan, A., Pope, J. M., Verkicharla, P. K., Suheimat, M. & Atchison, D. A. Change in human lens dimensions, lens refractive index distribution and ciliary body ring diameter with accommodation. *Biomedical Optics Express* **9,** 1272–1282 (2018).

84. Marchand, E. W. in *Gradient Index Optics* (ed Marchand, E. W.) 1–6 (Academic Press, 1978). ISBN: 978-0-12-470750-4. https://www.sciencedirect.com/science/article/pii/B9780124707504500050.

85. Smith, G. & Atchison, D. A. Equivalent power of the crystalline lens of the human eye: comparison of methods of calculation. *J. Opt. Soc. Am. A* **14,** 2537–2546. http://opg.optica.org/josaa/abstract.cfm?URI=josaa-14-10-2537 (1997).

86. Pérez, M, Bao, C., Flores-Arias, M., Rama, M & Gómez-Reino, C. Gradient parameter and axial and field rays in the gradient-index crystalline lens model. *Journal of Optics A: Pure and Applied Optics* **5,** S293 (Aug. 2003).

87. Díaz, J. A. ABCD matrix of the human lens gradient-index profile: applicability of the calculation methods. *Applied optics* **47,** 195–205 (2008).

88. Rosenblum, W., Blaker, J. & Block, M. Matrix methods for the evaluation of lens systems with radial gradient-index elements. *American journal of optometry and physiological optics* **65,** 661—665. ISSN: 0093-7002. https://doi.org/10.1097/00006324-198808000-00011 (1988).

89. Giovanzana, S., Evans, T. & Pierscionek, B. Lens internal curvature effects on age-related eye model and lens paradox. *Biomedical Optics Express* **8,** 4827–4837 (2017).

90. Gerrard, A. & Burch, J. M. *Introduction to matrix methods in optics* (Courier Corporation, 1994).

91. Olver, F. W., Lozier, D. W., Boisvert, R. F. & Clark, C. W. *NIST digital library of mathematical functions* chap. 15 (Cambridge university press, 2010).

92. Derocher, Z. *Custom dlls in OpticStudio: An overview of user-defined surfaces, objects, and other DLL types* https://support.zemax.com/hc/en-us/articles/1500005578162-Custom-DLLs-in-OpticStudio-An-overview-of-user-defined-surfaces-objects-and-other-DLL-types. [Accessed 02-2025]. 2021.

93. Culler, A., Humphreys, M. & Auriol, S. *How to compile a User-Defined DLL* https://support.zemax.com/hc/en-us/articles/1500005577602-How-to-compile-a-User-Defined-DLL. [Accessed 02-2025]. 2021.

94. Palos, F. *RT Lib, a ray tracing library for Matlab* Spain, 2014.

95. Roorda, A. & Glasser, A. Wave aberrations of the isolated crystalline lens. *Journal of Vision* **4,** 1. ISSN: 1534-7362. https://doi.org/10.1167/4.4.1 (2024) (Apr. 2004).

96. Atchison, D. A., Suheimat, M., Mathur, A., Lister, L. J. & Rozema, J. Anterior corneal, posterior corneal, and lenticular contributions to ocular aberrations. *Investigative Ophthalmology & Visual Science* **57,** 5263–5270 (2016).

97. Kiely, P., Smith, G. & Carney, L. The Mean Shape of the Human Cornea. en. *Optica Acta: International Journal of Optics* **29,** 1027–1040. ISSN: 0030-3909. https://www.tandfonline.com/doi/full/10.1080/713820960 (2023) (Aug. 1982).

98. Manns, F. & Ho, A. Paraxial equivalent of the gradient-index lens of the human eye. *Biomedical optics express* **13,** 5131–5150 (2022).

99. Artal, P., Guirao, A., Berrio, E. & Williams, D. R. Compensation of corneal aberrations by the internal optics in the human eye. *Journal of vision* **1,** 1–1 (2001).

100. Kelly, J. E., Mihashi, T. & Howland, H. C. Compensation of corneal horizontal/vertical astigmatism, lateral coma, and spherical aberration by internal optics of the eye. *Journal of Vision* **4,** 2–2 (2004).

101. Rozema, J. J., Hershko, S., Tassignon, M.-J., EVICR. net, P. G. S. G., Lorenz, K., von Trentini, M., Sala Pomares, E., Corral, M. J. G., Bataille, L., Alió, J. L., *et al.* The components of adult astigmatism and their age-related changes. *Ophthalmic and Physiological Optics* **39,** 183–193 (2019).

102. Hecht, E. *Optics Global Edition. England* 2016.

103. Thibos, L. N., Hong, X., Bradley, A. & Applegate, R. A. Accuracy and precision of objective refraction from wavefront aberrations. *Journal of vision* **4,** 9–9 (2004).

104. López-Gil, N., Fernández-Sánchez, V., Thibos, L. N. & Montés-Micó, R. Objective amplitude of accommodation computed from optical quality metrics applied to wavefront outcomes. *Journal of Optometry* **2,** 223–234 (2009).

105. Hermans, E., Dubbelman, M., van der Heijde, R. & Heethaar, R. The shape of the human lens nucleus with accommodation. *Journal of vision* **7,** 16–16 (2007).

106. Koretz, J. F., Kaufman, P. L., Neider, M. W. & Goeckner, P. A. Accommodation and presbyopia in the human eye—aging of the anterior segment. *Vision research* **29,** 1685–1692 (1989).

107. Koretz, J. F., Cook, C. A. & Kaufman, P. L. Accommodation and presbyopia in the human eye. Changes in the anterior segment and crystalline lens with focus. *Investigative ophthalmology & visual science* **38,** 569–578 (1997).

108. Koretz, J. F., Cook, C. A. & Kaufman, P. L. Aging of the human lens: changes in lens shape at zero-diopter accommodation. *JOSA A* **18,** 265–272 (2001).

109. Koretz, J. F., Cook, C. A. & Kaufman, P. L. Aging of the human lens: changes in lens shape upon accommodation and with accommodative loss. *JOSA A* **19,** 144–151 (2002).

110. Van Rossum, G. & Drake, F. L. *Python/C Api manual-python 3* (CreateSpace, 2009).

111. Bradski, G. & Kaehler, A. *Learning OpenCV: Computer vision with the OpenCV library* (" O'Reilly Media, Inc.", 2008).

112. Canny, J. A computational approach to edge detection. *IEEE Transactions on pattern analysis and machine intelligence,* 679–698 (1986).

113. Taubin, G. Estimation of planar curves, surfaces, and nonplanar space curves defined by implicit equations with applications to edge and range image segmentation. *IEEE Transactions on Pattern Analysis & Machine Intelligence* **13,** 1115–1138 (1991).

114. Korn, G. A. & Korn, T. M. *Mathematical handbook for scientists and engineers: definitions, theorems, and formulas for reference and review* (Courier Corporation, 2000).

115. Brown, N. The change in lens curvature with age. *Experimental Eye Research* **19,** 175–183 (1974).

116. Iribarren, R. Crystalline lens and refractive development. *Progress in retinal and eye research* **47,** 86–106 (2015).

117. Grosvenor, T. Reduction in axial length with age: An emmetropizing mechanism for the adult eye. *American Journal of Optometry and Physiological Optics* **64,** 657–663 (1987).

118. Brown, N. P., Koretz, J. F. & Bron, A. J. The development and maintenance of emmetropia. *Eye* **13,** 83–92 (1999).

119. Huggert, A. Are the discontinuity zones of the crystalline lens iso-indicial surfaces? *Acta Ophthalmologica* **24,** 417–421 (1946).

120. Siebinga, I., Vrensen, G. F., De Mul, F. F. & Greve, J. Age-related changes in local water and protein content of human eye lenses measured by Raman microspectroscopy. *Experimental eye research* **53,** 233–239 (1991).

121. Koretz, J. F. & Handelman, G. H. How the human eye focuses. *Scientific American* **259,** 92–99 (1988).

122. Dubbelman, M. & Van der Heijde, G. The shape of the aging human lens: Curvature, equivalent refractive index and the lens paradox. *Vision Research* **41,** 1867–1877 (2001).

123. Pierscionek, B. Presbyopia–effect of refractive index. *Clinical and Experimental Optometry* **73,** 23–30 (1990).

124. Smith, G & Pierscionek, B. The optical structure of the lens and its contribution to the refractive status of the eye. *Ophthalmic & physiological optics* **18** (1998).

125. Jongenelen, S., Rozema, J. J., Tassignon, M.-J., *et al.* Distribution of the crystalline lens power in vivo as a function of age. *Investigative ophthalmology & visual science* **56,** 7029–7035 (2015).

126. Dubbelman, M. & Van der Heijde, G. L. The shape of the aging human lens: Curvature, equivalent refractive index and the lens paradox. *Vision Research* **41,** 1867–1877 (2001).

127. Dubbelman, M., Van der Heijde, G. L. & Weeber, H. A. Change in shape of the aging human crystalline lens with accommodation. *Vision Research* **45,** 117–132 (2005).

128. Norrby, S. The Dubbelman eye model analysed by ray tracing through aspheric surfaces. *Ophthalmic and Physiological Optics* **25,** 153–161 (2005).

129. Manns, F, Ho, A & Parel, J.-M. in *Handbook of Visual Optics: Fundamentals and Eye Optics* 211–233 (CRC Press, 2017).

130. Moffat, B. A., Atchison, D. A. & Pope, J. M. Explanation of the lens paradox. *Optometry and vision science* **79,** 148–150 (2002).

131. Díaz, J. A., Pizarro, C. & Arasa, J. Single dispersive gradient-index profile for the aging human lens. *JOSA A* **25,** 250–261 (2008).

132. Birkenfeld, J., De Castro, A., Ortiz, S., Pascual, D. & Marcos, S. Contribution of the gradient refractive index and shape to the crystalline lens spherical aberration and astigmatism. *Vision research* **86,** 27–34 (2013).

133. Navarro, R., Palos, F. & González, L. M. Adaptive model of the gradient index of the human lens. II. Optics of the accommodating aging lens. *JOSA A* **24,** 2911–2920 (2007).

134. Rozema, J. J. Perpetual eye model with accommodation. *Investigative Ophthalmology & Visual Science* **64,** 3813–3813 (2023).

135. Smith, G., Atchison, D. A. & Pierscionek, B. K. Modeling the power of the aging human eye. *JOSA A* **9,** 2111–2117 (1992).

136. Hemenger, R. P., Garner, L. F. & Ooi, C. S. Change with age of the refractive index gradient of the human ocular lens. *Investigative Ophthalmology & Visual Science* **36,** 703–707 (1995).